# NAVAL POSTGRADUATE SCHOOL
Monterey, California

DISSERTATION

ANOMALOUS DIURNAL CURRENTS IN THE VICINITY OF
THE YERMAK PLATEAU

by

Christophe Prazuck

June, 1991

Dissertation Supervisor: Roland W. Garwood, Jr.

Approved for public release; distribution is unlimited

REPORT DOCUMENTATION PAGE

1a. REPORT SECURITY CLASSIFICATION UNCLASSIFIED	1b. RESTRICTIVE MARKINGS

2a. SECURITY CLASSIFICATION AUTHORITY	3. DISTRIBUTION/AVAILABILITY OF REPORT
2b. DECLASSIFICATION/DOWNGRADING SCHEDULE	Approved for public release; distribution is unlimited.

4. PERFORMING ORGANIZATION REPORT NUMBER(S)	5. MONITORING ORGANIZATION REPORT NUMBER(S)

6a. NAME OF PERFORMING ORGANIZATION Naval Postgraduate School	6b. OFFICE SYMBOL (If applicable) 55	7a. NAME OF MONITORING ORGANIZATION Naval Postgraduate School

6c. ADDRESS (City, State, and ZIP Code) Monterey, CA 93943-5000	7b. ADDRESS (City, State, and ZIP Code) Monterey, CA 93943-5000

8a. NAME OF FUNDING/SPONSORING ORGANIZATION	8b. OFFICE SYMBOL (If applicable)	9. PROCUREMENT INSTRUMENT IDENTIFICATION NUMBER

8c. ADDRESS (City, State, and ZIP Code)	10. SOURCE OF FUNDING NUMBERS			
	Program Element No	Project No	Task No	Work Unit Accession Number

11. TITLE (Include Security Classification)

ANOMALOUS DIURNAL CURRENTS IN THE VICINITY OF THE YERMAK PLATEAU

12. PERSONAL AUTHOR(S) Christophe Prazuck

13a. TYPE OF REPORT Dissertation	13b. TIME COVERED From To	14. DATE OF REPORT (year, month, day) 1991, June	15. PAGE COUNT 133

16. SUPPLEMENTARY NOTATION

The views expressed in this thesis are those of the author and do not reflect the official policy or position of the Department of Defense or the U.S. Government.

17. COSATI CODES			18. SUBJECT TERMS (continue on reverse if necessary and identify by block number)
FIELD	GROUP	SUBGROUP	Arctic Ocean. Ocean Wave Dynamics. Tides

19. ABSTRACT (continue on reverse if necessary and identify by block number)

Unexpectedly strong diurnal tidal currents, in a region dominated by semi-diurnal tidal surface displacements, were observed in the ARCTEMIZ 86 and 87 and CEAREX 89 records of buoy drift over the Yermak Plateau, a submarine feature north of Svalbard. Similar diurnal currents were observed during the FRAM III, FRAM IV experiments.

Data Analysis of the positions of the thirty satellite-tracked drifting buoys provides a description of the diurnal current field with good spatial coverage. This statistical description shows that tidal diurnal currents are enhanced over the entire plateau region. However, specific smaller regions above the plateau (order of 90 km) exhibit locally an even stronger and highly polarized response to the tide that has not been explained until now.

Firtly, a simple analytic model is used to show that the variation in the steepness of the slopes of the plateau could be responsible for significant spatial variations in the diurnal current field. Secondly, a numerical model shows that the variation in the curvature of the plateau is also important. Furthermore, the numerical model shows that the curvature of the topography causes the Yermak Plateau to act like a filter, responding resonantly to forcing with periods ranging from approximately 20 to 35 hours.

20. DISTRIBUTION/AVAILABILITY OF ABSTRACT [X] UNCLASSIFIED/UNLIMITED [X] SAME AS REPORT [ ] DTIC USERS	21. ABSTRACT SECURITY CLASSIFICATION Unclassified	
22a. NAME OF RESPONSIBLE INDIVIDUAL Dr. Roland W. Garwood, Jr.	22b. TELEPHONE (Include Area code) 408 646 3260	22c. OFFICE SYMBOL OC/Gd

DD FORM 1473, 84 MAR   83 APR edition may be used until exhausted   SECURITY CLASSIFICATION OF THIS PAGE
All other editions are obsolete   UNCLASSIFIED

Anomalous diurnal currents in the vicinity of the Yermak Plateau

by

Christophe Prazuck
Lieutenant Commander, French Navy
Ingénieur de l'Ecole Navale, 1981

Submitted in partial fulfillment of the
requirements for the degree of

DOCTOR OF PHILOSOPHY IN PHYSICAL OCEANOGRAPHY

from the

NAVAL POSTGRADUATE SCHOOL

June 1991

A B S T R A C T

Unexpectedly strong diurnal tidal currents, in a region dominated by semi-diurnal tidal surface displacements, were observed in the ARCTEMIZ 86 and 87 and CEAREX 89 records of buoy drift over the Yermak Plateau, a submarine feature north of Svalbard. Similar diurnal currents were observed during the FRAM 111, FRAM 1V experiments.

Data Analysis of the positions of the thirty satellite-tracked drifting buoys provides a description of the diurnal current field with good spatial coverage. This statistical description shows that tidal diurnal currents are enhanced over the entire plateau region. However, specific smaller regions above the plateau (order of 90 km) exhibit locally an even stronger and highly polarized response to the tide that has not been explained until now.

Firstly, a simple analytic model is used to show that the variation in the steepness of the slopes of the plateau could be responsible for significant spatial variations in the diurnal current field. Secondly, a numerical model shows that the variation in the curvature of the plateau is also important. Furthermore, the numerical model shows that the curvature of the topography causes the Yermak Plateau to act like a filter, responding resonantly to forcing with periods ranging from approximately 20 to 35 hours.

TABLE OF CONTENTS

I. INTRODUCTION

A.   THE YERMAK PLATEAU

The Yermak Plateau (Figure 1.1) is an extension of the Barents Sea continental slope, covering roughly 20,000 km^2 northwest of the coast of Svalbard. The plateau lies on a 350 km-long arc with a 100 km width. Minimum water depths along the crest of the arc are of the order of 500 m near Svalbard and deepen to 700 m further north. On the north and the west sides of the plateau, the bottom slopes rapidly to depths of approximately 3500 m. In contrast, the eastern slopes are more gentle and reach a maximum depth of 2200 m as they encompass a semi-enclosed basin.

B.   GLOBAL AND REGIONAL TIDAL MODELS IN THE NORDIC SEA AND THE ARCTIC OCEAN

Following Hoffman (1990), the tides in this region are dominated by the semi-diurnal frequency. Schwiderski's (1986) method of tidal prediction combines the Newtonian tide-generating potential and hydrodynamical features of the ocean with the Navier-Stokes equations of motion to produce a global tidal prediction system with accuracy of better than 10 cm. Through the use of tidal decomposition he has produced corange and cotidal maps for eleven tidal constituents covering the entire globe. The leading semi-diurnal (M_2, principal lunar) and diurnal (K_1, declination luni-solar) tidal components respectfully, show the dominance of semidiurnal surface displacements in the Nordic Seas (Figure 1.2 and Figure 1.3). In the vicinity of the Yermak Plateau, Schwiderski's (1986) data show semidiurnal amplitudes of the order of 20 cm and diurnal amplitudes of only 2 to 3 cm.
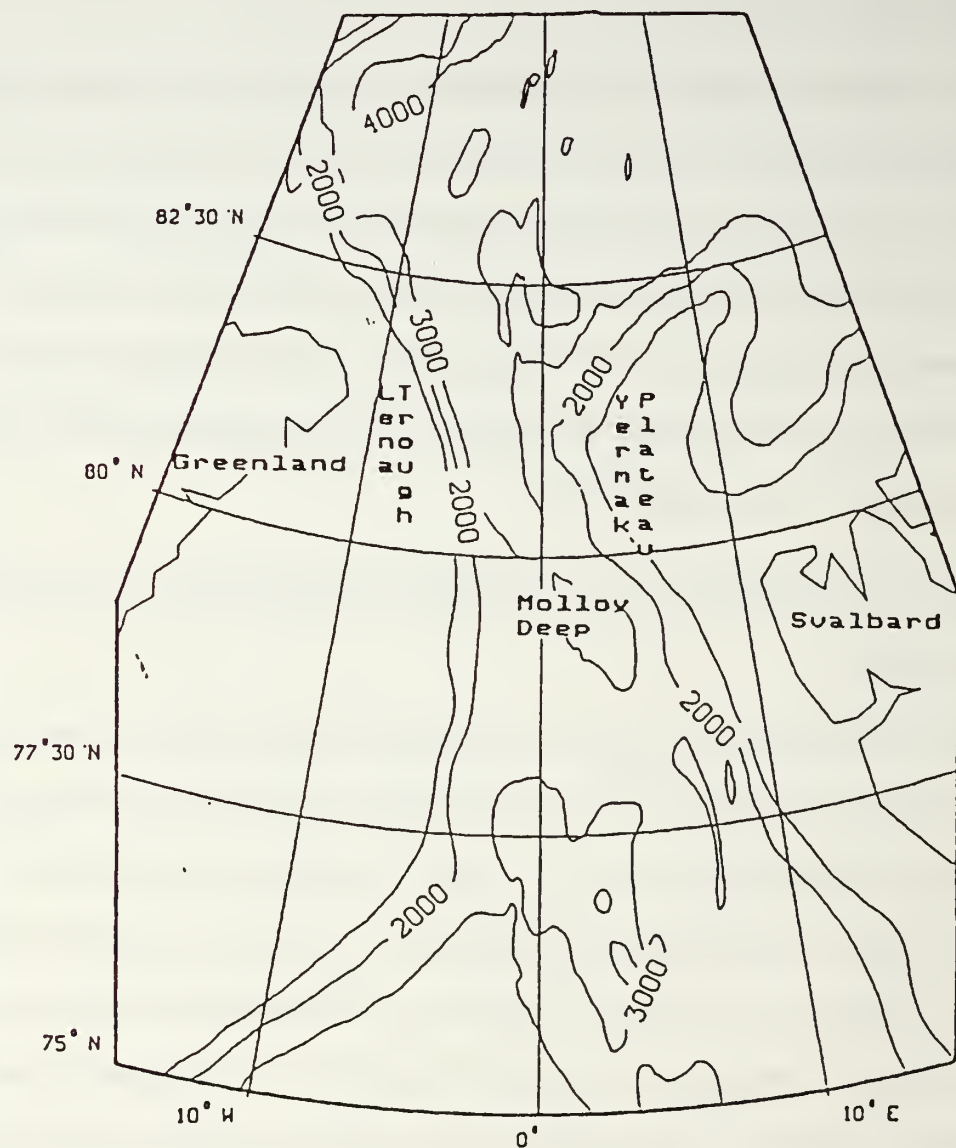
Figure 1.1 The Yermak Plateau and surrounding bathymetry (from Hoffman, 1990).
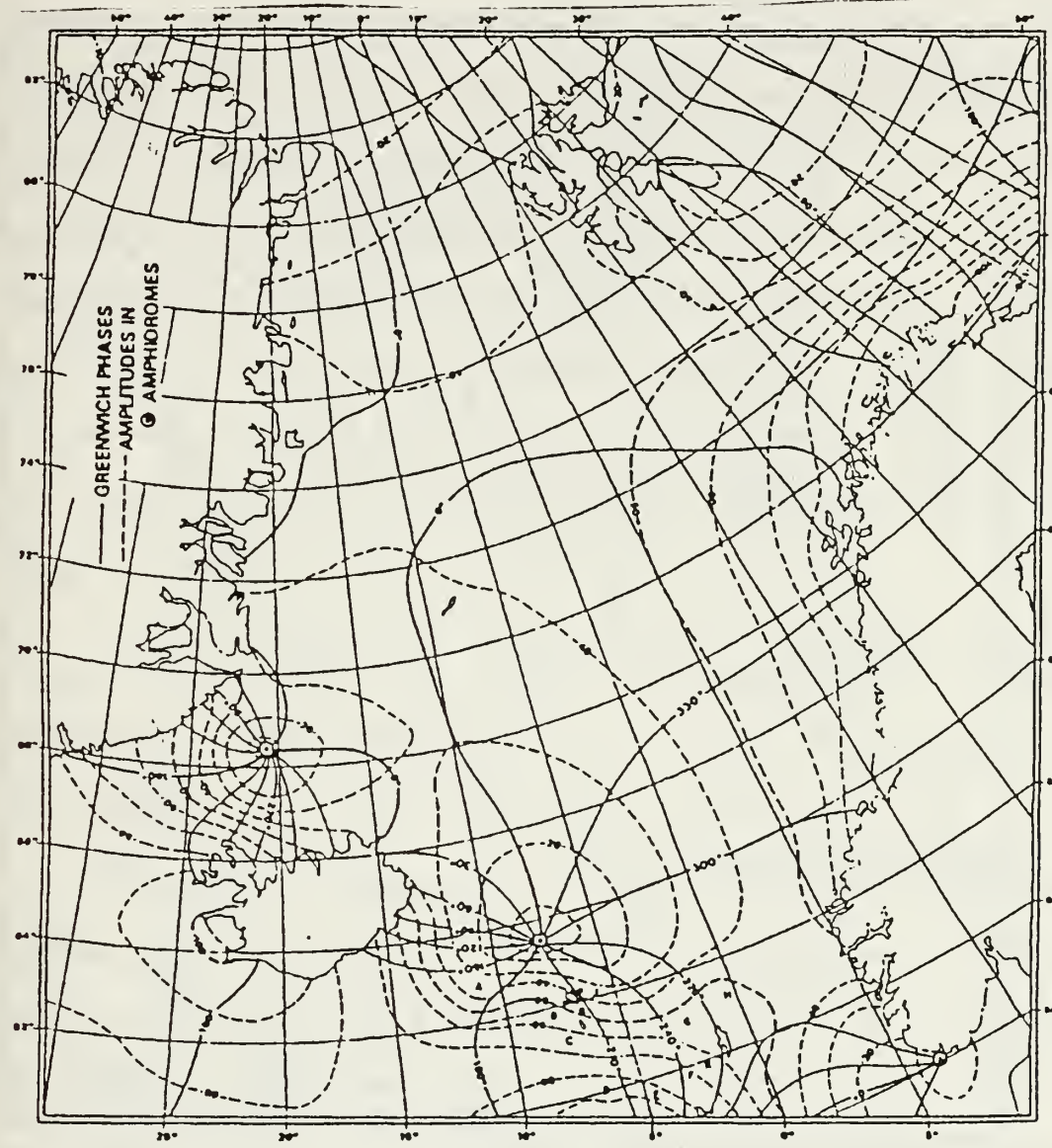
Figure 1.2 Leading semi-diurnal (M₂) ocean tide. The Greenwich equi-phase lines are spaced every 30° (1 hour); the equi-amplitude lines every 10 cm (from Schwiderski, 1986).

3
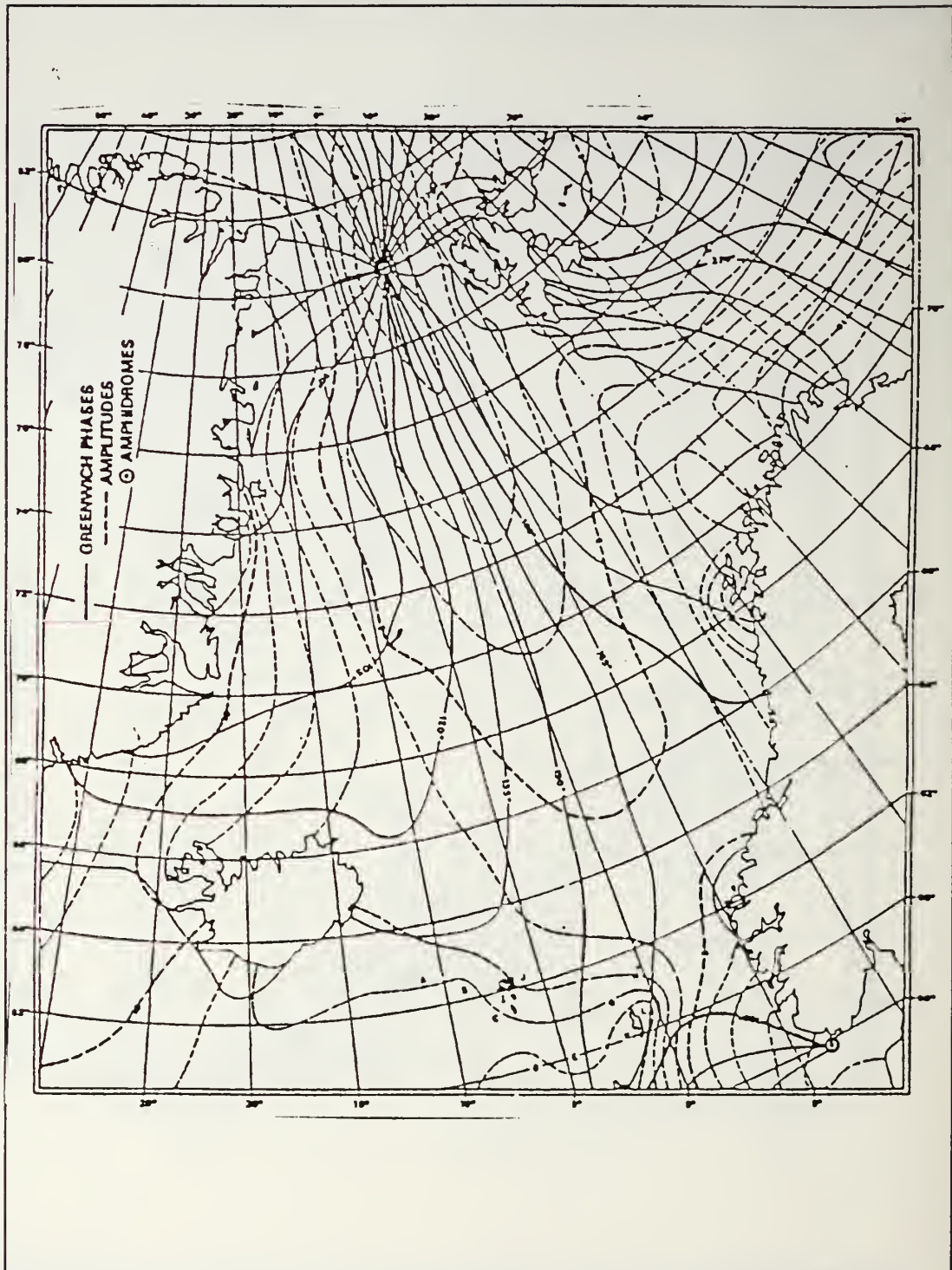
Figure 1.3 Leading diurnal (K_1) ocean tide. The Greenwich equi-phase lines are spaced every 15° (1 hour); the equi-amplitude lines every 1 cm (from Schwiderski, 1986).

4

A regional tidal model has been developed by Gjevik and Straume (1989) covering the Nordic Seas and the Arctic Ocean on a stereographic map projection with a grid size 50 x 50 km at 60° N. The amplitudes of the M_2 and K_1 tides are similar to the ones found in Schwiderski's global model and show the same amphidrome in Fram Strait for the K_1 tide. In addition, the model shows a band-shaped region with mainly clockwise current rotation along the shelf west of Norway and over to Svalbard. According to the authors this indicates that the K_1 tide has a coastal trapped wave (CTW) modal structure in this region. Muench et al. (1990) describes the results of this model in the region of the Yermak Plateau as enhanced K_1 currents with the fastest currents occurring over the core of the plateau, in accordance with the view that the amplification is due to cross-slope continuity of the barotropic tidal flux.

C. TIDAL CURRENTS IN THE VICINITY OF THE YERMAK PLATEAU: OBSERVATIONS AND EXPLANATIONS

1. MIZEX 84

The currents were measured by current meters deployed beneath the ice from freely-drifting floes occupied by the R/V Polar Queen during June and July 1984 in a region centered on 80.7° N and 3° E. Morison et al. (1987) and McPhee (1987) present results showing strong semi-diurnal and diurnal motions during this period. During the period of drift between the 1,000 and 3,000 m depth contours over the southwest slope of the Yermak Plateau a strong diurnal component of motion is responsible for open-loops in the drift track of the R/V Polar Queen. The across and along-slope velocities at the diurnal period are of the order of 20 and 10 cm/s respectively, rotating in a clockwise sense. Elsewhere the drift data show little energy at the diurnal period. Morison et al.

(1987) reason that the observed diurnal motion which occurs over the plateau may be a combination of forced internal tidal motion and barotropic motion.

2. FRAM III AND FRAM IV

a. Observations

Hunkins (1986) examines data from the FRAM III (1981) and FRAM IV (1982) drifting ice stations. Each station was occupied for two months during spring. The stations were set at latitude 84° and drifted over water depths of 4,000 m before reaching the shallower northern flank of the Yermak Plateau (Figure 1.4).
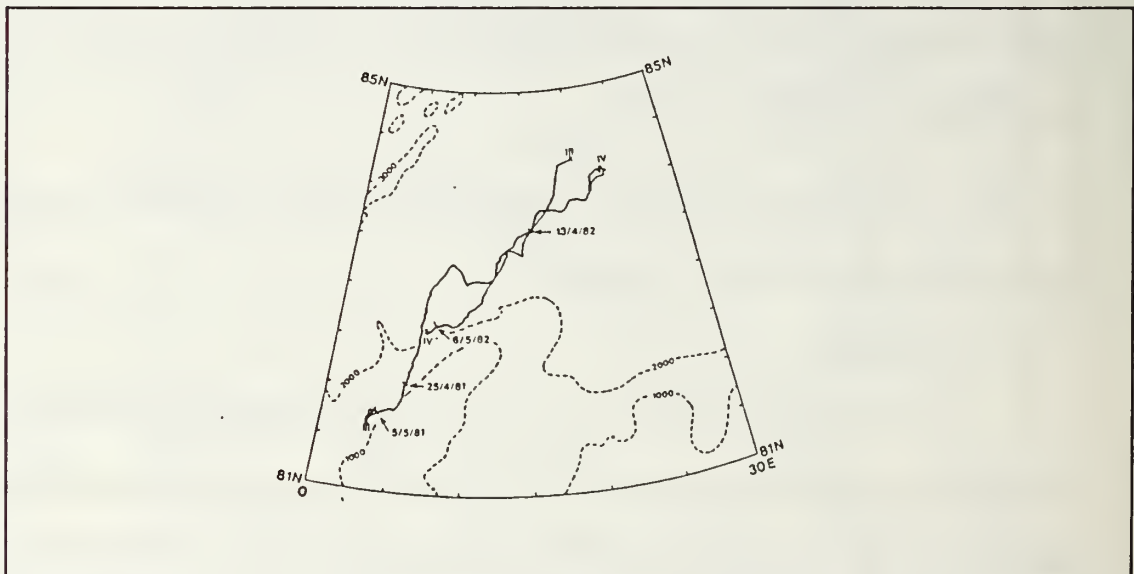
Figure 1.4 Drift tracks of ice camps FRAM III and FRAM IV (solid lines) superimposed on depth contours (dashed lines) (from Hunkins, 1986).

Current data were obtained at 25 and 104 m for FRAM III, and 29, 55, 104, 153, 303 m for FRAM IV. The ice drift track is derived from Transit fixes. Absolute currents are decomposed into orthogonal components across- and along-slope. The two ice camps followed similar tracks. In both cases strong diurnal currents are observed over the steep

6

northern slopes of the plateau in the depth ranges of 800 to 2,000 m (upper slope) in 1981 and 1800 to 3,500 m (lower and middle slope) in 1982 (Figures 1.5 and 1.6).

The diurnal current vector has two principal characteristics:

- a nearly circular clockwise rotation over the upper slope

- an almost rectilinear segment aligned in the across-slope direction over the middle and lower slope.

It must be kept in mind that this description suffers from a spatial ambiguity: the tracks of the ice camps (Figure 1.4) show that the lower and middle slope are situated closer to the northern tip of the plateau than is the upper slope over which the camp drifted in the middle of the almost rectilinear northwestern side of the plateau.
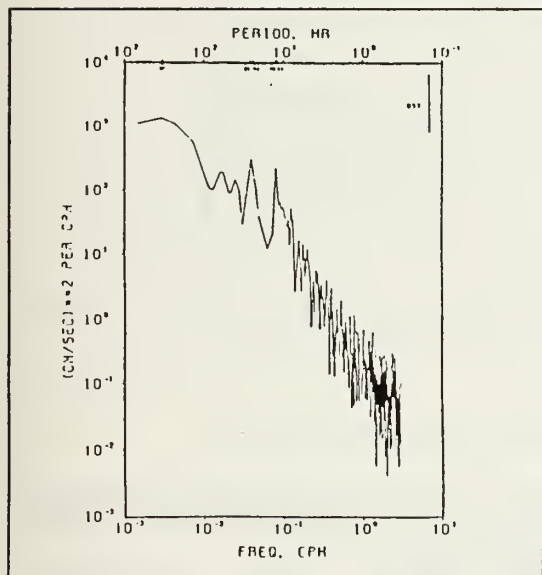
Figure 1.5 Kinetic energy spectrum for along-slope velocity, FRAM IV 303 m (from Hunkins, 1986).
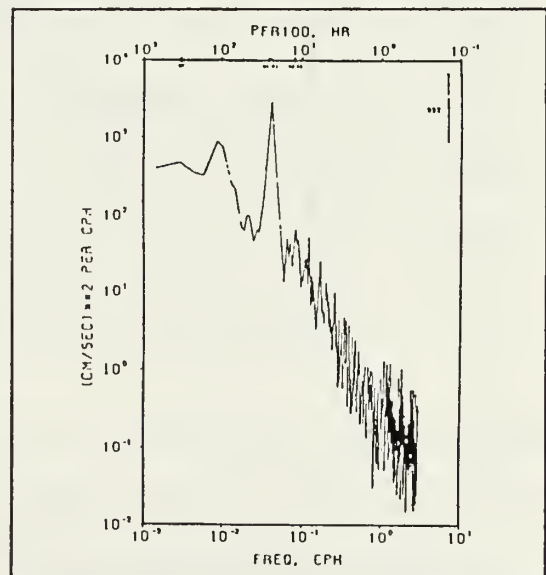
Figure 1.6 Kinetic energy spectrum for across-slope velocity, FRAM IV 303 m (from Hunkins, 1986).

On the other hand, all semi-diurnal tidal component ellipses are aligned along-slope. These factors apply to observation at all depths, although the upper 100 m of the water column is strongly stratified. Hunkins also points out that the surface current speeds, as measured by ice drift, are less than the subsurface current speeds. Hunkins explains that these observations are suggestive of Kelvin waves for the semi-diurnal period (Kowalik, 1979) and consistent with topographic vorticity waves at the diurnal period.

b.   *Interpretation*

Adapting Longuet-Higgins's (1970) theory of vorticity waves around an island, Hunkins develops a solution for free vorticity waves around a circular submarine plateau (Figure 1.7).
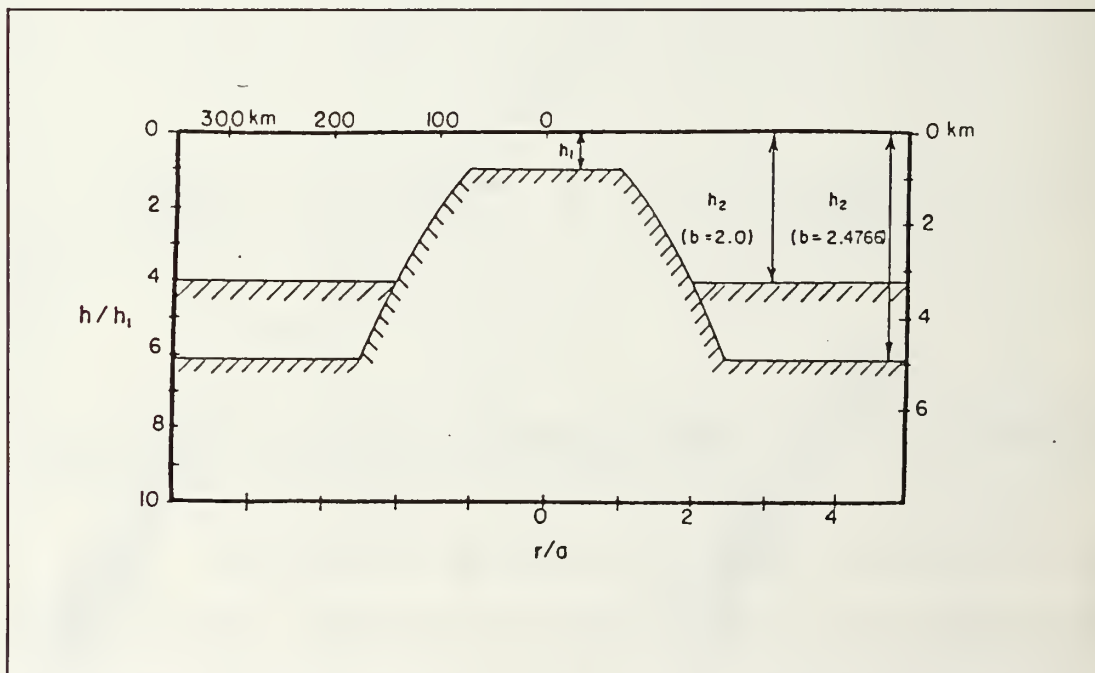
Figure 1.7 Cross section of the circular submarine plateau used by Hunkins (1986) in his development of a model for coastal trapped waves.
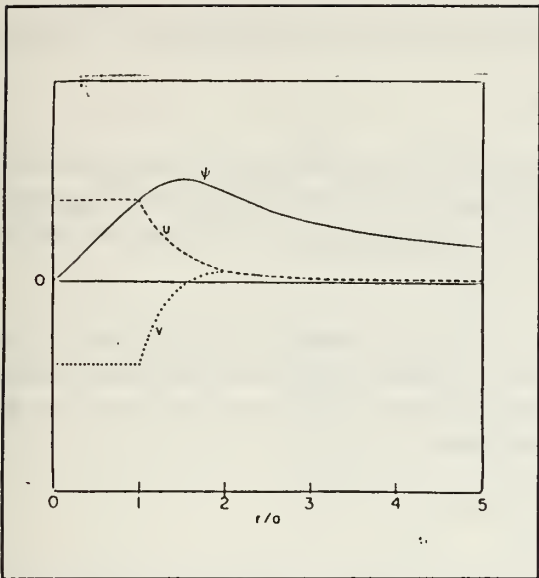
Figure 1.8 Stream function and velocity components for mode (1,1) with $b = 2.0$ and $\omega/f = 0.5$ (from Hunkins, 1986).
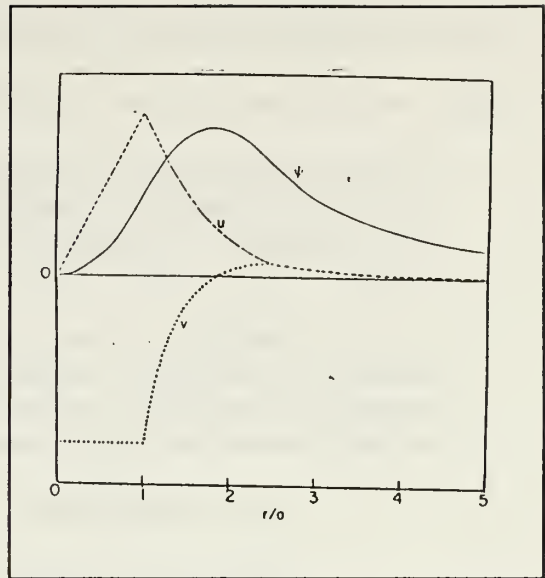
Figure 1.9 Stream function and velocity components for mode (1,2) with $b = 2.47$ and $\omega/f = 0.5$ (from Hunkins, 1986).

Reasonable agreement between an idealized shelf profile (defined by the two shelf scaling parameters a and b) and the actual north, west and northwest shelves can be made by setting $a = 70$ km and setting b between 2.0 and 2.47. The free wave solutions have both modal structure in the radial (2m cells) and the azimuthal (2n cells) direction. At the diurnal period over the Yermak Plateau only the modes $(m,n) = (1,1)$ or $(1,2)$ can exist with the slope extending from $r/a = 1$ to $b = 2$ for mode (1,1) and r/a extending from 1 to $b = 2.47$ for mode (1,2), where r is radial coordinate equal to 0 at the center of the plateau. Therefore a diurnal forcing would generate resonant natural conditions of oscillation.

Figure 1.8 (Figure 1.9) shows the stream function and velocity component amplitudes for the mode (1,1) (mode (1,2)) at the diurnal frequency. Wherever u (radial velocity) and v (azimuthal velocity) are of the same (opposite) sign the current rotates

9

counter-clockwise (clockwise). The result is consistent with the observations over the upper slope. However, the model has two difficulties:

- It fails to explain the quasi-rectilinear across-slope motion found on the lower slope close to the northern tip of the plateau. Hunkins argues that along-shelf variations of the topography may broaden the mid-slope nodal region and produce this current feature.

- It shows a trapping occurring over the flat top of the plateau. This trapping is more important for the gravest mode (1,1). Due to forcing scale considerations Hunkins considers that mode (1,1) is the most likely to happen. We will see later that this trapping feature does not fit other observations.

c.   *Further developments*

Hoffman (1990) applied the Hunkins model to the eastern slope of the plateau to show that diurnal vorticity waves cannot be supported by the gentle topography in this region. Chapman (1989) refines the Hunkins model by including a forcing mechanism. An oscillating rectilinear barotropic current flows over an isolated radially-symmetric topographic feature. Bottom friction induces forced topographically-trapped waves. The forced wave has a structure very similar to the free wave structure. For a given shelf width Figure 1.10 shows the maximum velocity amplifications occurring on the flat top (u_K and v_K being the forcing velocities of the incident tidal Kelvin wave); it can reach a normalized value of 60 for a period close to the diurnal period (ω is 0.47 for O_1, 0.51 for K_1) . The robustness of this result is tested by varying the shelf width parameter b. Figure 1.11 shows that the amplification is greater than 5 for $1.6 < b < 2.4$ for the K_1 tide (the values of b chosen by Hunkins for the Yermak Plateau are 2.0 and 2.47). The results are identical for the O_1 tide.

10
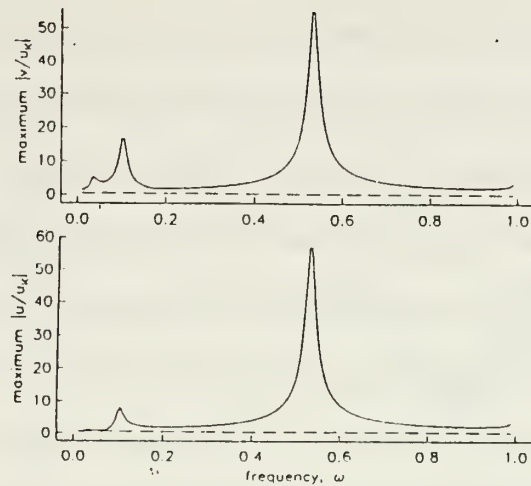
Figure 1.10 Velocity amplification as a function of non-dimensionalized frequency (ω/f) for Rockall Bank. The results are very similar for the Yermak Plateau (from Chapman, 1989).
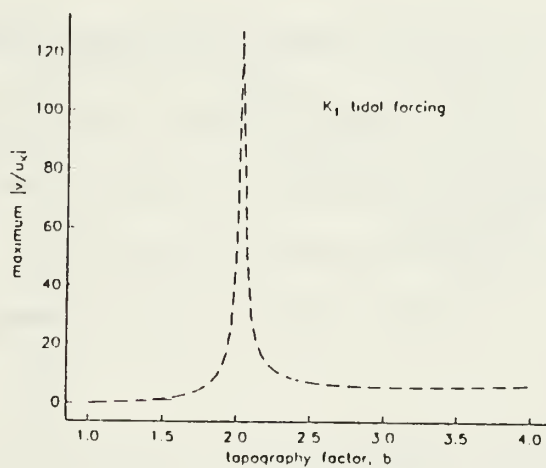
Figure 1.11 Maximum azimuthal velocity amplification for the K_1 tide vs shelf width parameter b at Yermak Plateau (dashed line) (from Chapman, 1989).

11

3.   ARCTEMIZ 86

Fifteen ARGOS satellite tracked buoys were deployed north of 83°N. Several of them passed over the Yermak Plateau between late June and early September.

Using both standard FFT analysis (Figures 1.12 and 1.13) and a complex demodulation technique developed by McPhee (1986), Hoffman (1990) detected anomalous strong diurnal currents along the northern slope of the plateau. The across- slope current is strong enough relative to the mean current to produce diurnal loops between the 1,000 m and 3,000 m depth contours. The order of magnitude of the across- (along-) slope current was 20 (10) cm/s, determined from ice motion. A beat is quite apparent in the demodulated clockwise diurnal velocity (Figure 1.14) and is interpreted as a fortnightly beat. Most of the energy at the diurnal period is found in the clockwise components.

D.   SOME OTHER EXAMPLES OF ANOMALOUS DIURNAL CURRENTS

Apart from the Yermak Plateau, unexpectedly strong diurnal currents that do not conform to other local observations or models have been observed in five other regions:

- around the island of St. Kilda near Scotland (Cartwright, 1969)

- at Rockall Bank, a submarine plateau west of the British Isles (Huthnance, 1974)

- off Vancouver Island, Canada (Crawford and Thomson, 1982)

- on the Campbell Plateau near New Zealand (Heath, 1983)

- in the vicinity of the Farallones Islands near San Francisco (Noble, personal communication).
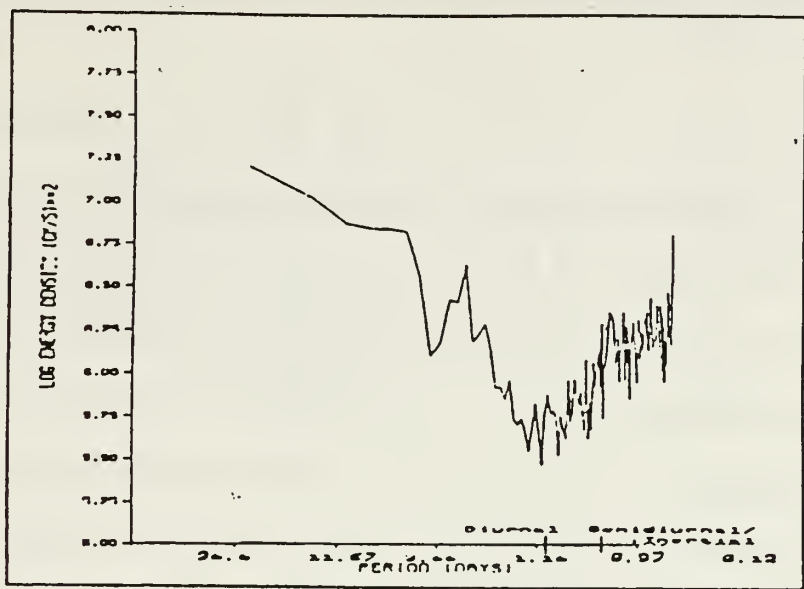
Figure 1.12 Kinetic energy spectrum for u while ARCTEMIZ 86 buoys flow over depths greater than 3,000 m (from Hoffman, 1990).
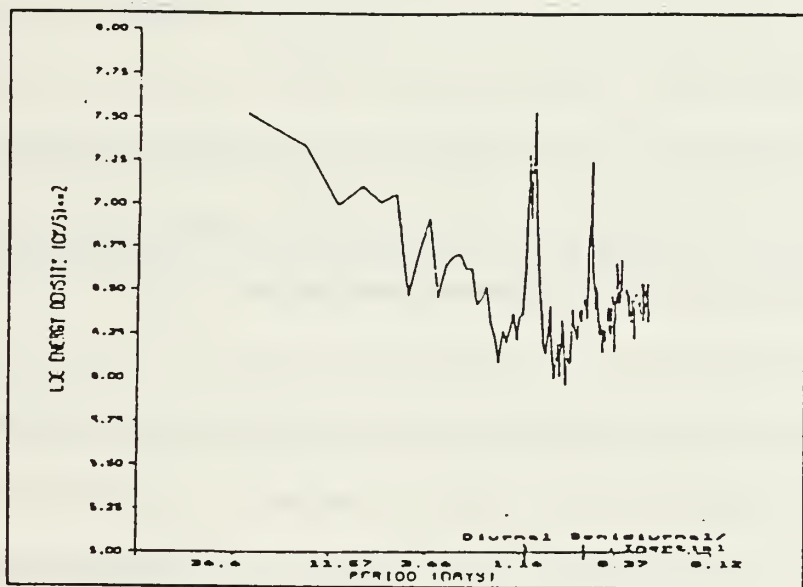
Figure 1.13 Kinetic energy spectrum for u while ARCTEMIZ 86 buoys flow over depths shallower than 3,000 m (from Hoffman, 1990).
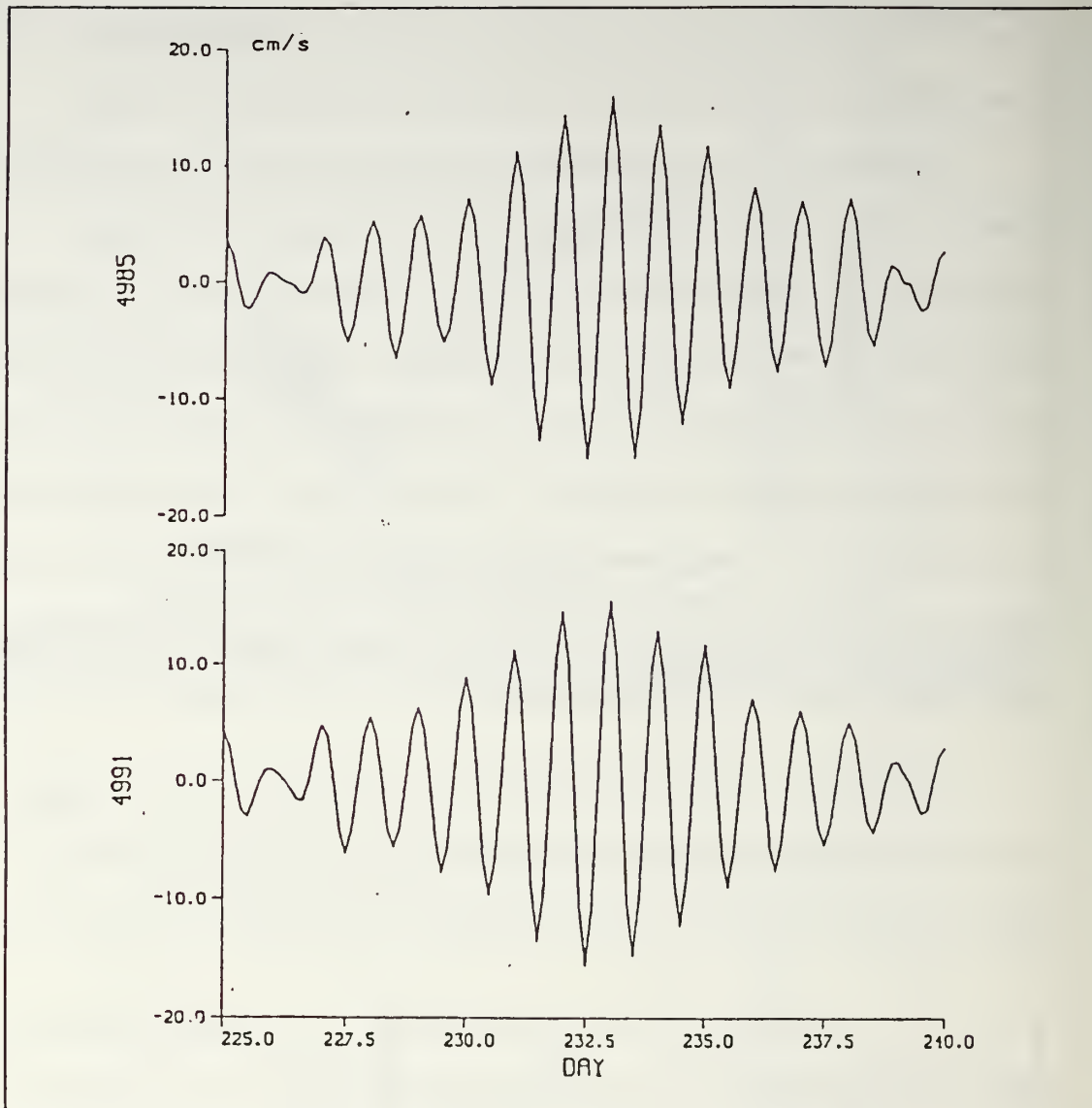
Figure 1.14 Diurnal clockwise velocity peak from two ARCTEMIZ 86 buoys on the northern slope of the Yermak Plateau (from Hoffman, 1990).

1. St. Kilda

Cartwright (1969) and Cartwright et al. (1980) investigate tidal current records from the St. Kilda shelf. They interpret the anomalous strong diurnal components of motion as the superposition of a Kelvin wave and a short topographic wave. They point

14

out that the strong coherence of their records is an indication of the barotropic character of the waves.

2. Rockall Bank

Huthnance (1974) analyzes tidal records from Rockall Bank. Rockall Bank is an elongated bank of length scale of order 100 km. Off the southern end of the bank, observations show anomalous strong diurnal currents that do not seem to be present at other locations around the bank. An analytic circular model is developed showing that the lowest order mode of a topographically trapped wave is close to resonance with the diurnal tide. In order to account for the much stronger diurnal current observed at the tip of the bank, the author describes the circulation around an abrupt elliptic bank, showing a tip-enhancement comparable to the one observed in the real data.

3. Vancouver Island

Currents and sea level data from the Coastal Oceanic Dynamics Experiment off Vancouver Island are analyzed by Crawford and Thomson (1982, 1984). Strong across-slope diurnal currents are interpreted in terms of coastally trapped waves (CTW).

In the first of these two papers the authors show that bottom friction acting on an incident Kelvin wave can generate a barotropic CTW. Their approach is similar to that of Gill and Schumann (1974) who express the forcing in terms of across-slope modes corresponding to the free CTW modes. In the second paper Crawford and Thomson take the stratification into account and explain the enhanced diurnal currents as a first baroclinic mode CTW.

4. Campbell Plateau

Heath (1983) reports anomalous strong currents at the diurnal period, attributable to two possible mechanisms:

- proximity of an amphidrome

- or, more likely, to existence of a coastal trapped wave.

E. COASTAL TRAPPED WAVES

1. Propagation

It is well known that topography can trap energy in the form of vorticity waves where the conservation of potential vorticity is the principal restoring mechanism. A review of the more recent papers on this subject is given by Brink (1987).

The role of stratification in the propagation of CTW is discussed by Huthnance (1978) and Chapman (1983). Brink (1989) focuses on the effect of stratification on waves trapped around a seamount. The importance of stratification can be measured by the stratification parameter:

$$S = \frac{N^2 H^2}{f^2 L^2}$$

where N is the buoyancy frequency, f is the Coriolis parameter and inertial frequency, H a typical water depth, and L a typical horizontal scale of the topography. When this parameter is small the effect of stratification can be neglected and the barotropic assumption is valid.

In the case of the Yermak Plateau a typical value of $N = 3$ cph (Padman et al., 1991) leads to a stratification parameter of the order of 0.03. Hence the barotropic assumption is valid as a first approximation.

The propagation characteristics of CTW in a barotropic medium are qualitatively different from those in a stratified medium. In a barotropic medium it can be

16

shown that each mode has a high frequency cut-off that is always less than the inertial frequency f. The group speed is zero at this cut-off frequency. On the other hand, when S is large the entire frequency range, up to f is possible for the modes. The waves are no longer frequency limited but become wavenumber limited, and the group speed is always in the same direction as the phase speed.

The forcing of CTW by the atmosphere is investigated in Gill and Schumann (1974) and in other recent papers. The role played by CTW in the propagation of tidal energy is considered by comparatively fewer authors. Three of these include Cartwright (1969), Munk et al. (1970), and Daifuku and Beardsley (1983).

2. Scattering of CTW with bottom friction

The propagation of CTW has been mostly studied under the assumption of uniform alongshore profile of topography. However, some workers have investigated the effects of small variations in bottom topography (Chao et al., 1979; Brink, 1980; Brink, 1986), slow along-shelf variations (Grimshaw, 1977), and abrupt change in bottom topography (Wang, 1980; Wilkin and Chapman, 1987; Webster, 1987; Wilkin and Chapman, 1990). The later case will be of interest in this work. In these papers, the shelf is idealized by two semi-infinitely uniform shelf profiles linked by an abrupt transition zone (Figure 1.15 gives an example of such a shelf geometry).

The modal structure for CTW up-shelf may be quite different from the modal structure allowed by the topography down-shelf. In the later case, when an incident wave reaches the transition zone its energy is redistributed among available down-shelf modes (transmission or forward scattering) and/or backscattered (reflected) in the direction opposite to the incidence of the wave. This last case can happen only when the CTW is frequency limited and not wavenumber limited. Then there are two wavenumbers for each
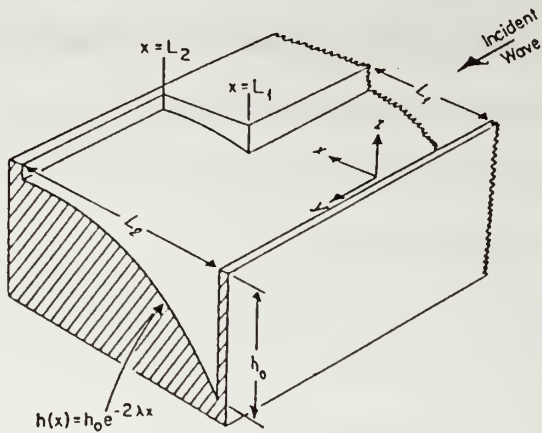
Figure 1.15 Shelf geometry (from Wilkin and Chapman, 1987).

frequency below the cut-off frequency of a given mode: a long-wave wavenumber corresponding to a wave propagating with relatively high positive phase speed and large positive group speed, and a short-wave wavenumber corresponding to a wave propagating with smaller positive phase speed and smaller negative group speed. Backscattering for a given mode and frequency occurs in forms of CTW having negative group speed. The difference in magnitude between the group speeds suggests that the latter is more vulnerable to dissipation (Wang, 1980). Schwing (1989) shows that friction can dissipate a CTW with negative group speed in the space of a shelf width approximately.

As the frequency of the incident wave approaches the cut-off frequency down-shelf, reflection increases. Of particular interest for this research is the case where the frequency of the incident wave is above the critical frequency (cut-off frequency of the first mode down-shelf). Then energy cannot be transmitted forward except in evanescent form (modes decaying exponentially in the along-shelf direction), and most of it is reflected. This case has been studied by Wang (1980) for idealized shelf profiles. Figure 1.16 shows an

example where 30% of the energy is transmitted down-shelf, the rest of it being reflected by a canyon in a frictionless ocean. The results are displayed in terms of along-shelf distribution of along and across-shelf transport computed at two locations along the shelf. In Figure 1.17 friction is added to the model. It has a large effect on the reflected wave, limiting the amplitude of the interference patterns and confining them in the vicinity of the transition zone. In this example across-shelf transport is dominated by the reflected wave, and friction has a strong effect on the transport.
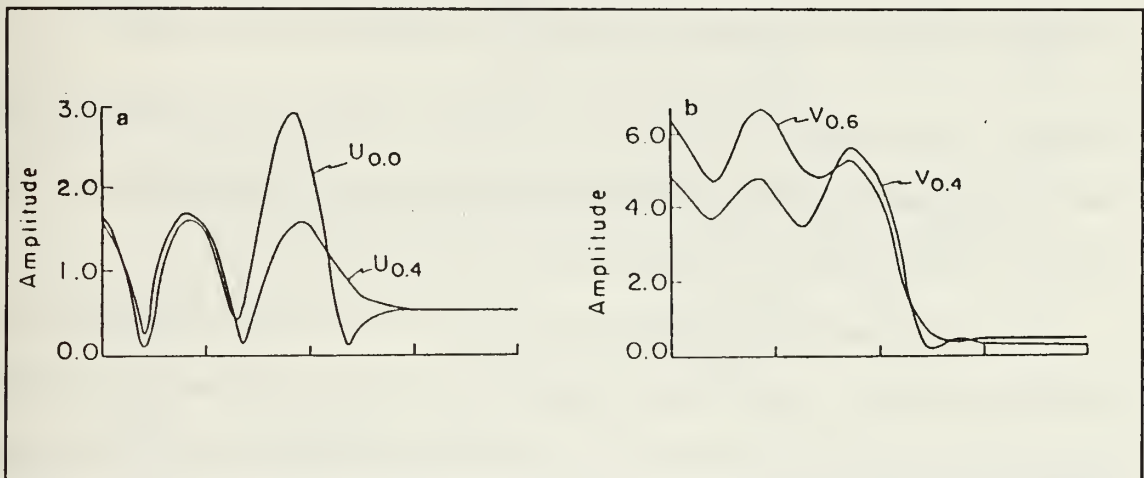
Figure 1.16 Along-shelf distribution of (a) along- and (b) across-shelf transport (b); index 0.0 indicates the shelf break (modified from Wang, 1980)

F.   ICE MOTION

The goal of this part of the present work is to describe the diurnal tidal currents on the Yermak Plateau based on ice floe tracks. However, the relation between ice motion and the underlying currents is not simple. Apart from wind stress, the ice motion is forced by the ocean currents via interfacial stress. Hunkins (1986) notices that the tidal motion of the ice is significantly less than the motion recorded for the underlying current. Another

19
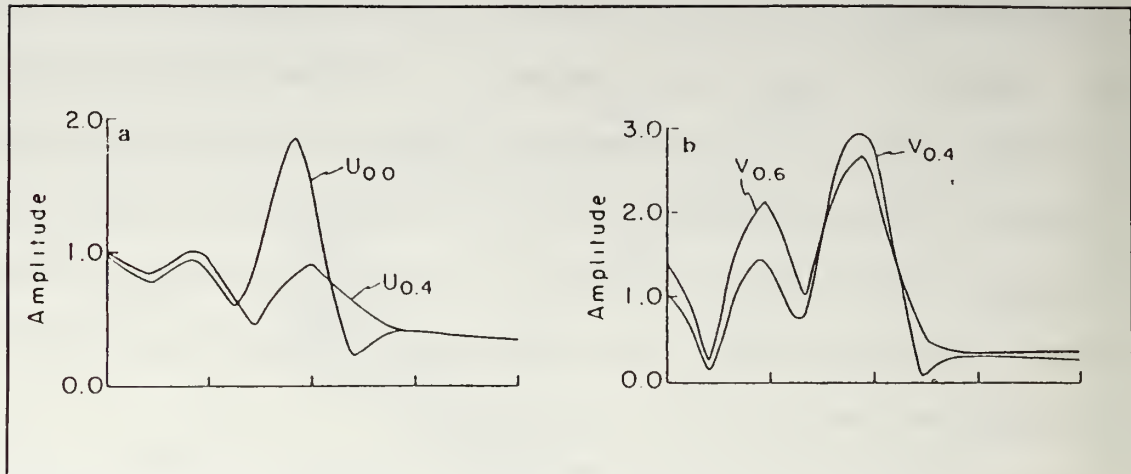
Figure 1.17 Same as figure 18 with friction (modified from Wang, 1980)

ambiguity is the compactness of the ice; in a free ice condition it is reasonable to assume that the ice motion represents well the underlying currents. Hoffman (1990) assumes that the ARCTEMIZ 86 observations are made in free ice condition.

Ice compactness varies both in time and space. It is questionable to assume that ice motion represents even qualitatively the underlying currents whenever and wherever the free ice assumption is not valid. This is especially important in our case where oscillating currents are trapped in a narrow region; the scale of the horizontal constraints on ice floes due to compactness may be larger than the across-shelf modal structure of the trapping.

Figure 1.18 shows the discrepancies between ice motion and underlying current in the diurnal band recorded during CEAREX 89 on the Yermak Plateau (L. Padman, personal communication). The ratio of the ice velocity to the current is not constant. Also, there are significant phase shifts.

In this work the following assumptions will be made:

- ice floes drift in free ice condition
- there is direct proportionality between ice motion and water motion.

20

These approximations become less realistic as ice concentration increases during late fall and winter.
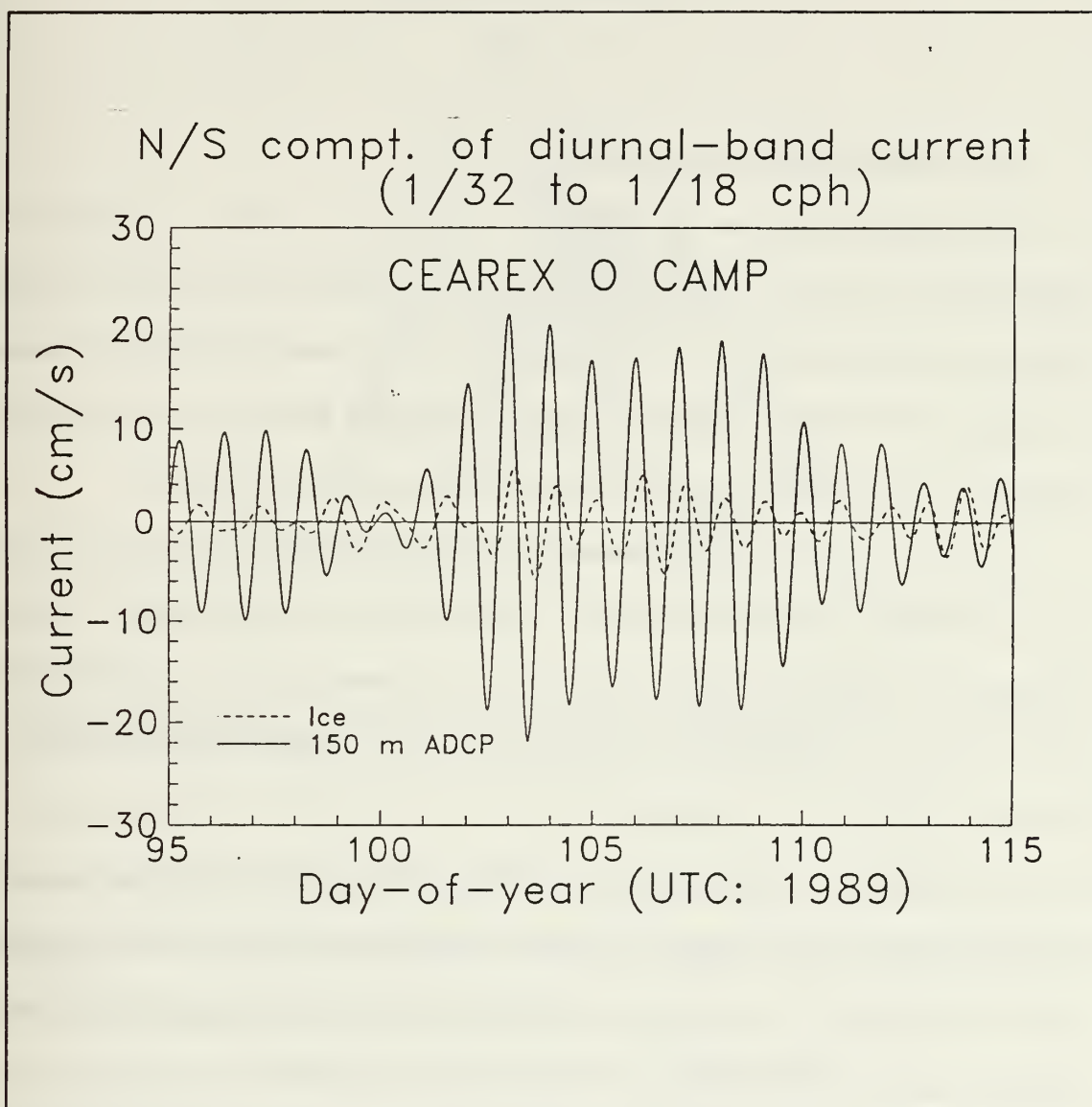
**Figure 1.18** Comparison between ice motion and underlying current in the diurnal band recorded during CEAREX 89 (Padman, personal communication).

II. DATA ANALYSIS

A. ARCTEMIZ 87 DATA ANALYSIS

ARCTEMIZ 87 is the University of Paris' second attempt at deploying an observational network in the European Sector of the Arctic Ocean between Svalbard, Greenland and the North Pole. The first attempt of this kind was ARCTEMIZ 86, discussed by Hoffman (1990). Nine buoys were deployed on the ice during the period of 15 July through 14 August 1987. Their deployment positions are given in Table 2.1.

It must be noted that the buoys were deployed 4 months later in the year than those for ARCTEMIZ 86. Consequently the 87 buoys drifted over the Yermak Plateau in November and December, experiencing a higher ice concentration than the ARCTEMIZ 86 buoy covering for the same region during June, July and August of the previous year.

1. Raw data

The buoys were tracked by the ARGOS satellite system with position accuracies of approximately 0.5 km. Figure 2.1 shows the trajectory of the buoys. The irregularly spaced position data are interpolated to produce latitude and longitude at three hour intervals. Total velocity (V), east-west (u) and north-south (v) velocities are computed from these interpolated positions. From here on these velocities will be referred to as currents, even if strictly speaking they are ice velocities and are only indirectly related to water velocities. "Underlying current" will be used to refer to the actual water velocity.

All of the buoys trajectories are illustrated in Appendix A. Of the nine buoys deployed, six drifted over the Yermak Plateau. Enhanced views of their tracks in the
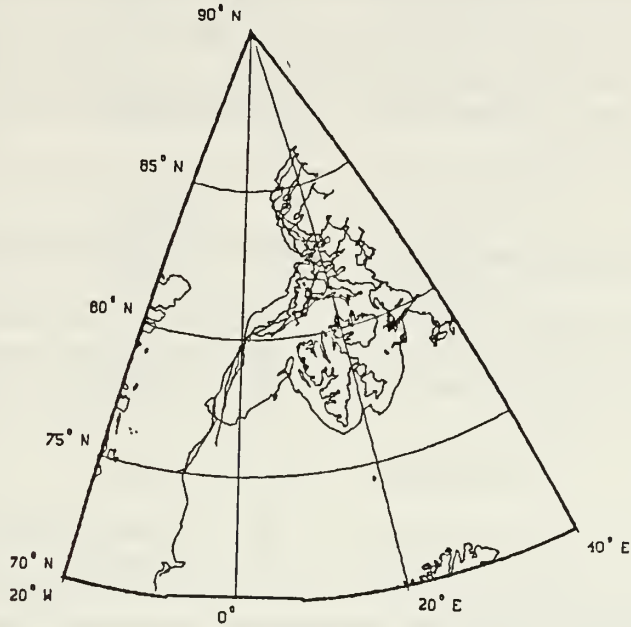
Figure 2.1 Trajectories of the 9 buoys deployed in ARCTEMIZ 87.

vicinity of the plateau are shown in Appendix B. Compared with the '86 buoy tracks it is evident that all of the '87 trajectories pass south of the northeastern tip of the plateau. The other three buoys (4992, 5079 and 5095) will not be discussed in the present work because their positions never approached the plateau.

TABLE 2.1 ARCTEMIZ 87 ARGOS BUOYS.

Buoy number	Deployment Latitude	Deployment Longitude	Deployment Date (Julian)
5095	82 428 N	31 327 E	15 July (196)

5079	82 990 N	31 927 E	16 July (197)
5094	83 408 N	30 127 E	20 July (201)
4996	84 455 N	30 020 E	24 July (205)
5077	85 042 N	28 565 E	27 July (208)
4992	85 518 N	25 283 E	28 July (209)
3491	85 907 N	22 670 E	31 July (212)
4994	85 368 N	21 472 E	11 Aug (223)
1479	83 375 N	19 838 E	14 Aug (226)

2.   Time series analysis

Time series analysis is performed using a fast Fourier analysis of east-west and north-south velocity data to produce kinetic energy spectra for each component. The data are separated into two sets corresponding to periods when the drifters were above the plateau (delimited by the 3,000 m isobath) or away from the plateau (Figures 2.2 to 2.5).

Comparing kinetic energy spectra magnitude (Figures 1.12 and 1.13) from ARCTEMIZ 86 (Hoffman, 1990) shows that the signal magnitude is one order of magnitude lower in 1987 than in 1986 both in deep and shallow waters. This is likely due to the higher ice concentration experienced by the ARCTEMIZ 87 drifters (Lewis et al. 1989).

When the buoys are in deep water no peak is discernable at the diurnal period. On the other hand two distinct peaks near the diurnal period appear when the buoys are over the Yermak Plateau. One peak between 25.56 and 27.39 hours (centered on 26.48 hours) contains the energy associated with the O_1 tide (period of 25.8192 h), and the other

and stronger one between 23.24 and 24.75 hours (centered on 24.00 hours) contains the energy associated with the K_1 tide (period of 23.9345 h), exceeding significantly the semi-diurnal peak. Compared with the '86 data, the '87 peaks are at least one order of magnitude weaker but the signal to noise ratio is of the same order (1 to 1.25 on a log scale).

Attention must be drawn to the fact the data were assumed to be ergodic in order to perform this analysis. This hypothesis is certainly not valid. Nevertheless if the diurnal signal is strong enough to be evident after an averaging process, its significance is even greater.

3.   Complex demodulation

The spectral analysis above clearly reveals the difference in the ice motion between deep water and shallow water conditions. However, as an averaging process, it is not sufficient to determine any smaller scale spatial variability of the diurnal enhancement on the plateau. Following the work done by Hoffman (1990), the complex demodulation technique of McPhee (1986) is applied to the data.

Use of this method presumes drifter trajectory to be a superposition of mean motion, diurnal and semidiurnal motions. Clockwise and counterclockwise sense of rotation are considered for both semidiurnal and diurnal period. The total velocity V is decomposed into:

$$V = V_m + S_{cw} e^{-ft} + S_{ccw} e^{ft} + D_{cw} e^{-\omega t} + D_{ccw} e^{\omega t}$$

where f is the semi-diurnal frequency and ω is the diurnal frequency. The complex coefficients in the above equation are determined every 3 hours by a least mean square fit, based on a 48 hour data window. As a result, the energy of the signal is divided into 4
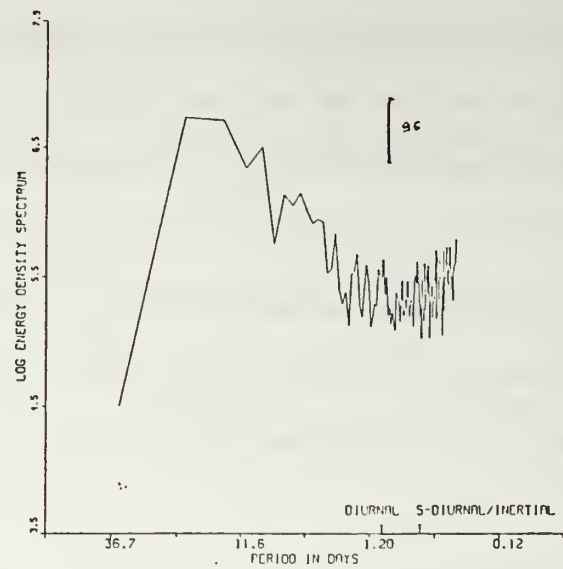
Figure 2.2 Kinetic energy spectrum for u component of velocity while buoys were in waters deeper than 3,000 m.
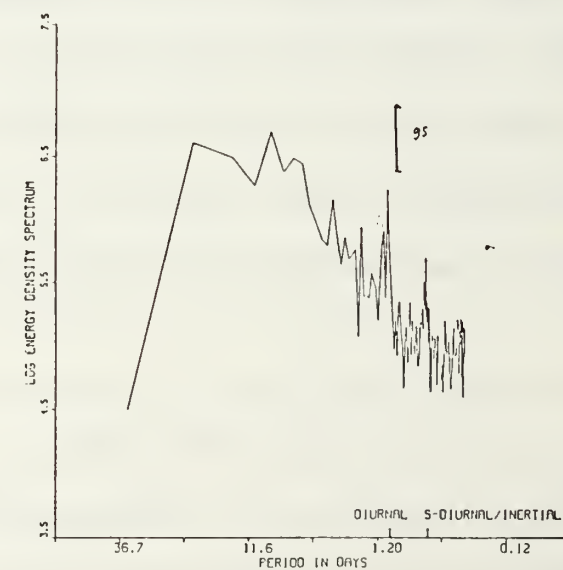
Figure 2.3 Kinetic energy spectrum for u component of velocity while buoys were in waters shallower than 3,000 m.
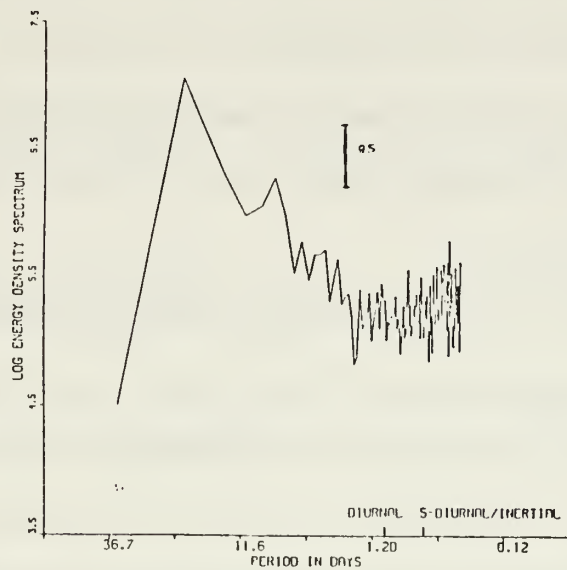
Figure 2.4 Kinetic energy spectrum for v component of velocity while buoys were in waters deeper than 3,000 m.
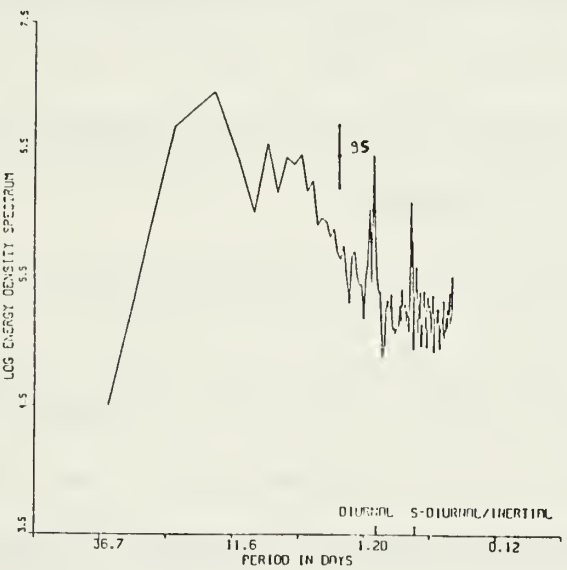

Figure 2.5 Kinetic energy spectrum for v component of velocity while buoys were in waters shallower than 3,000 m.

different bands in a manner similar to what would be obtained using a rotary spectrum decomposition computed with a shifting 48 hour data window.

At the latitudes of interest, the leading semi-diurnal period (12.2 hours) is almost identical to the inertial period (about 12.1 hours), and we will not try to discriminate between the two.

Appendix C is a collection of the results of the complex demodulation for all the buoys. The most noticeable features appearing in some of these plots are the strong pulses observed in the clockwise part of the diurnal signal. Figure 2.6 and Figure 2.7 show these pulses for buoys 1479 and 3491. The envelopes of the pulses have a period of 10 days for the first buoy and 15 days for the second. However, the effects of spatial and temporal variation on drifter data and the uncertainty of ice-current coupling (see Introduction) limit the utility of the amplitudes calculated for the modulation periods above. These pulses in amplitude are similar to those found by Hoffman (1990).

These strong diurnal components appear only when the buoys are above the yermak plateau. This confirms the result of the FFT analysis. However, even while the buoys are bove the plateau the diurnal component amplitudes vary significantly.

4.   Data Analysis conclusion

The following intermediate conclusions are drawn from the data analysis performed above:

* Abnormally strong diurnal currents exist in the vicinity of the Yermak Plateau. This has been discovered in data collected by current-meters (FRAM III and IV) and by drifters (ARCTEMIZ 86 and 87) in 1981, 1982, 1986 and 1987.
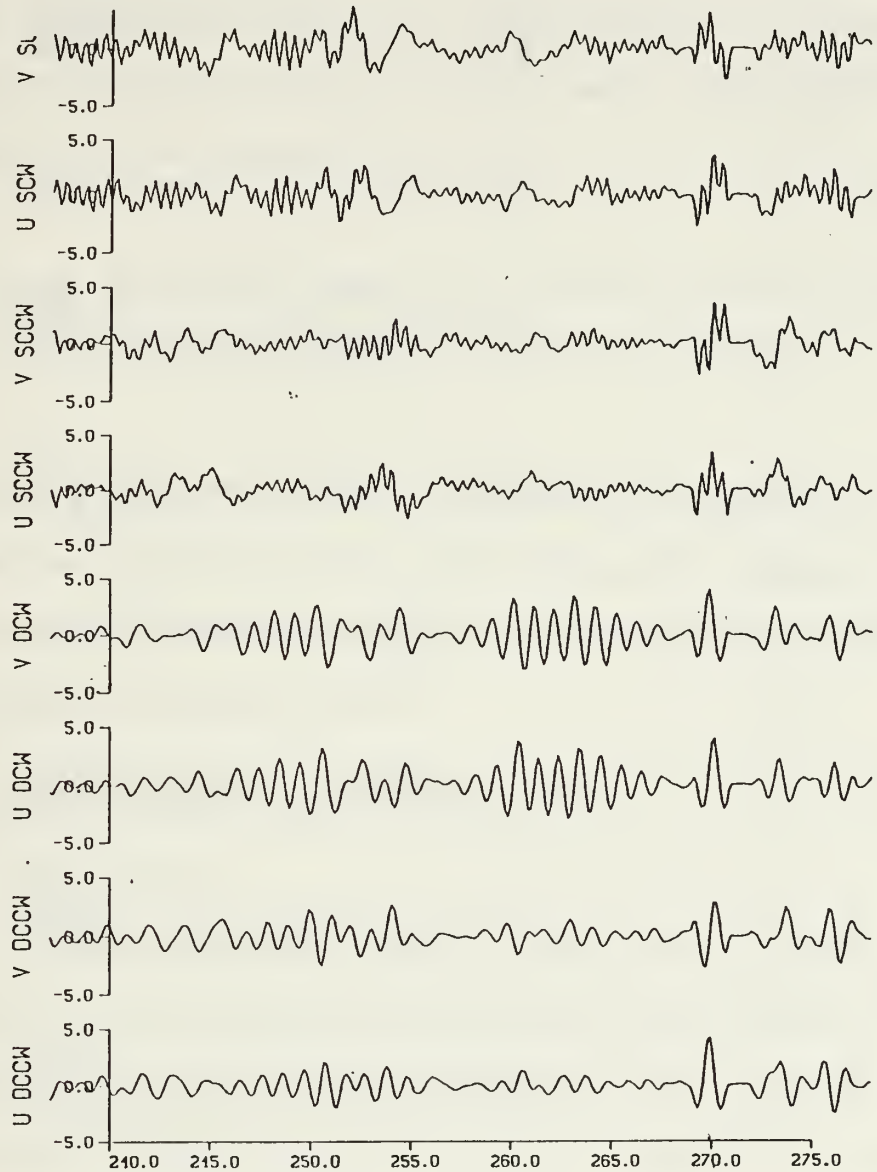
Figure 2.6 Time series reconstructed from complex demodulation for buoy 1479. The u and v components are separated into semidiurnal/diurnal clockwise (SCW/DCW) and counter-clockwise (SCCW/DCCW) signals.

29
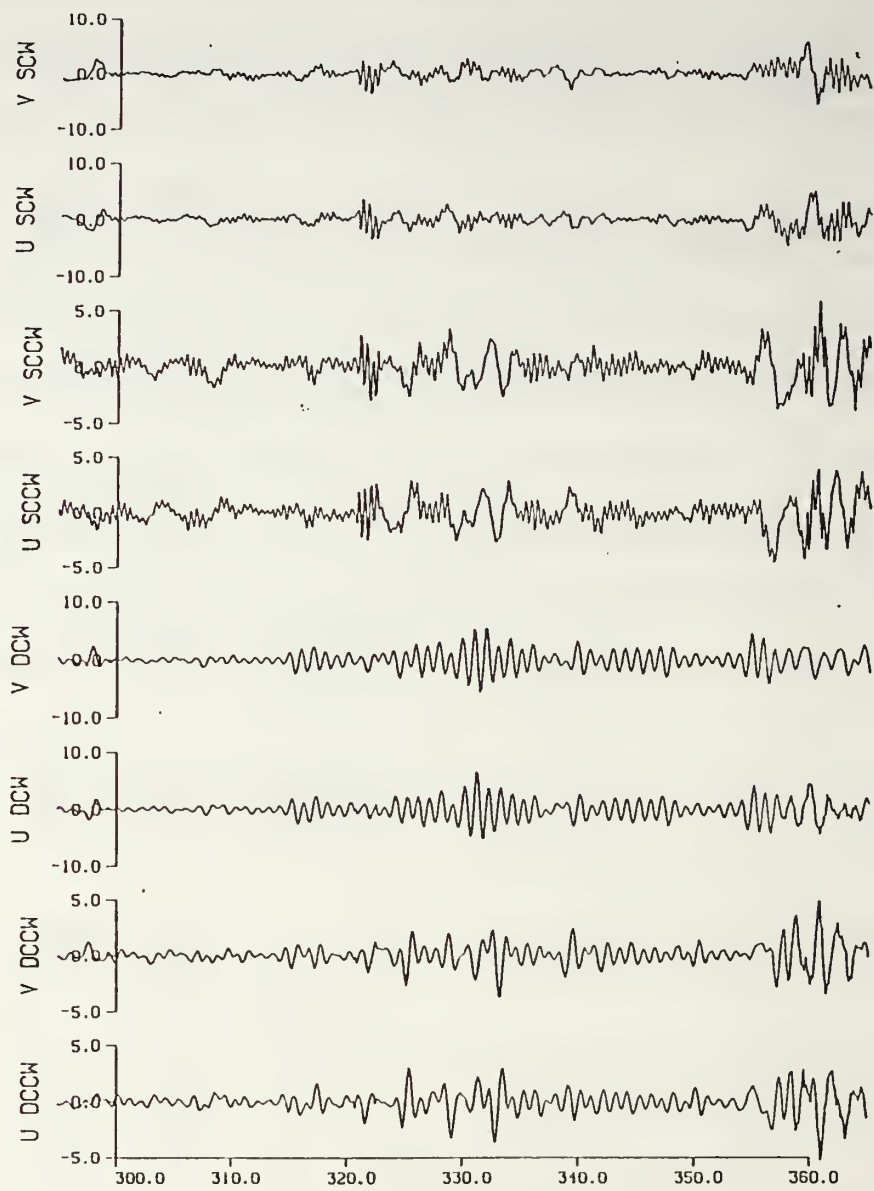
Figure 2.7 Time series reconstructed from complex demodulation for buoy 3491. The u and v components are separated into semidiurnal/diurnal clockwise (SCW/DCW) and counter-clockwise (SCCW/DCCW) signals.

30

* Neglecting any possible interannual variability, FFT analysis shows a marked seasonal variability between the summer ARCTEMIZ 86 data and the fall-winter ARCTEMIZ 87 data. The latter have a weaker variance over the whole spectrum. However, the nature of the FFT treatment may mask a spatial variability due to the difference of tracks followed in '86 and '87.

* Complex demodulation suggests that the diurnal current enhancement present some spatial variability on the plateau.

* Both the stability of the diurnal enhancement on a long time scale (same phenomenon recorded from 1981 to 1989), and the stability and the narrowness of the frequency band of the observed signal are indicative of a process that is decoupled from atmospheric forcing.

B.   SYNOPTIC PRESENTATION OF THE DATA

1.   Data processing

A synoptic presentation of the data is made in order to best determine the spatial variability of the enhancement of the diurnal tidal velocities. Figure 2.8 shows the tracks of the 15 buoys that drifted over the Yermak Plateau during ARCTEMIZ 86 and 87, revealing the relatively good coverage of the east part of the plateau and the relatively poorer sampling of the northwest slope. Figure 2.9 displays the tracks of 6 buoys that drifted in the vicinity of the northwest slope of the plateau during CEAREX 89. These buoys provide supplementary information in this area. The data are processed separately

using the same method of interpolation and complex demodulation, as discussed in the section "Data Analysis."

Figure 2.10 displays the portion of the tracks where strong diurnal demodulated components appear. Visual inspection shows that the northeast tip of the plateau is the region were most of the strong components are observed. This localization excludes the northwest slope and the eastern part of the plateau. Conclusions drawn for the northwest slope are somewhat uncertain due to a poor sampling, but we will see later that these conclusions can be confirmed by CEAREX 89 observations. Such doubts do not arise for the eastern part of the plateau where the sampling is good.

The following analysis is meant to provide an overall picture of the diurnal currents over the Yermak Plateau. The plateau is divided into 14 geographical and bathymetric domains, as listed in table 2.2.

TABLE 2.2 DEFINITION OF 14 SUB-AREAS ABOVE THE YERMAK PLATEAU.

Area #	Limits in latitude	Limits in longitude	Limits in depth
1	80. / 81. N	1. / 5. E	> 800m
2	81. / 82.5 N	2. / 7. E	500 < D < 1500m
3	82. / 82.5 N	8. / 12. E	1500 < D < 2500m
1	82. / 83. N	8. / 12. E	1500 < D < 2500m
5	82.5 / 83. N	8. / 12. E	2500 < D < 3500m

6	82. / 82.6 N	12. / 15. E	600 < D < 2000m
7	82.5 / 83. N	12. / 18. E	2000 < D < 3200m
8	83. / 84. N	16. / 24. E	3200 < D < 4000m
9	80. / 81.5 N	4. / 8. E	200 < D < 1000m
10	81.5 / 82.5 N	16. / 22. E	2000 < D < 3000m
11	81. / 82. N	8. / 13. E	700 < D < 1300m
12	81. / 82. N	11. / 15. E	1000 < D < 2200m
13	80.5 / 81. N	10. / 16. E	1000 < D < 2000m
14	81. / 82. N	12. / 16. E	2000 < D < 3000m

For each period and sense of rotation, the following method is applied: each time the position of a buoy falls into one of the geographical sub-areas of table 2.2, the current vector at the required period is computed from complex demodulation output. This vector is the sum of the vectors corresponding to the two senses of rotation. In each sub-area a collection of current vectors is obtained, forming a cluster of points in the (u,v) plane.

For each cluster the covariance matrix is formed:

$$\begin{vmatrix} S_{uu} & S_{uv} \\ S_{uv} & S_{vv} \end{vmatrix}$$

with :

$$\bar{U} = \frac{1}{N}\sum_{i=1}^{N} U_i \qquad\qquad \bar{V} = \frac{1}{N}\sum_{i=1}^{N} V_i$$

$$S_{uu} = \frac{1}{(N-1)}\sum_{i=1}^{N} (U_i - \bar{U})^2 \qquad\qquad S_{vv} = \frac{1}{N-1}\sum_{i=1}^{N} (V_i - \bar{V})^2$$

$$S_{uv} = \frac{1}{(N-1)}\sum_{i=1}^{N} (U_i - \bar{U})(V_i - \bar{V})$$

and a principle component analysis is performed in order to produce σ_1 and σ_2, the two positive eigenvalues of the symmetric covariance matrix in increasing order. The corresponding eigenvectors, **E1** and **E2**, are orthogonal. The eigenvector **E1** indicates the direction of the major axis of the envelope of the cluster of points, and the eigenvector **E2** indicates the minor axis. In the frame of reference defined by (**E1,E2**) the eigenvalues are the estimators of the variance along the x and y axes. Assuming that the current vector has a two dimensional normal distribution, P percent of the data are contained within an ellipse defined by:

$$\left(\frac{x}{\sigma_1}\right)^2 + \left(\frac{y}{\sigma_2}\right)^2 = \chi_P^2$$

so $\sigma_1\chi_P$ and $\sigma_2\chi_P$ are the values of the major and minor axes of the ellipse, respectively. We use P = 95%. The strength of the polarization can be computed (Mauchly, 1940):

$$P_e = L_e^{N-2} \qquad\qquad L_e = \frac{2\sigma_1\sigma_2}{\sigma_1^2 + \sigma_2^2}$$

34

where N is the number of points to analyze in the cluster. It is assumed that there is no polarization when P_e is close to 1 (i.e. the envelope is a circle). When P_e is small such an assumption cannot hold.

The sense of rotation of each ellipse is determined by applying the same treatment as above separately to the clusters formed by the clockwise and counter-clockwise current vectors. Hence two envelopes are associated with each sub-area, one corresponding to a clockwise sense of rotation and the other to a counter-clockwise sense of rotation. According to rotary spectrum theory the envelopes of these clusters should be circles, and the circle with the largest radius imposes the sense of rotation. Due to the method of sampling the data and to the fact that the data are collected over areas and not at a single point, the principal component analysis gives ellipses even for a single sense of rotation.
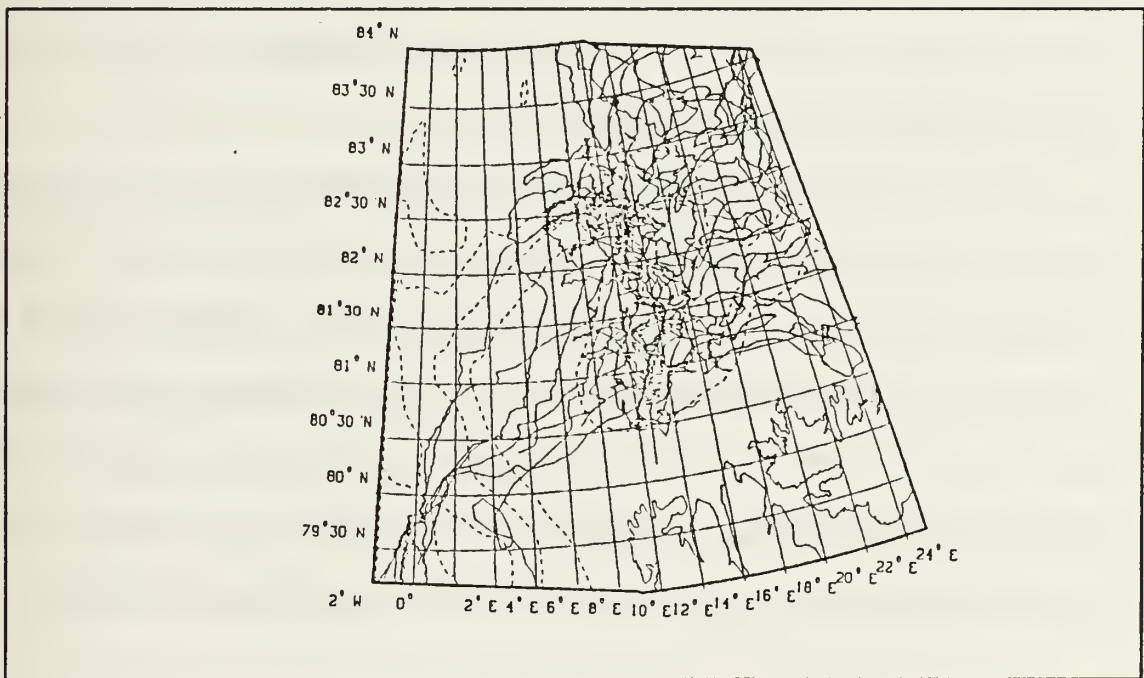

Figure 2.8 Tracks of the 15 buoys that drifted over the Yermak Plateau as part of ARCTEMIZ 86 and 87.
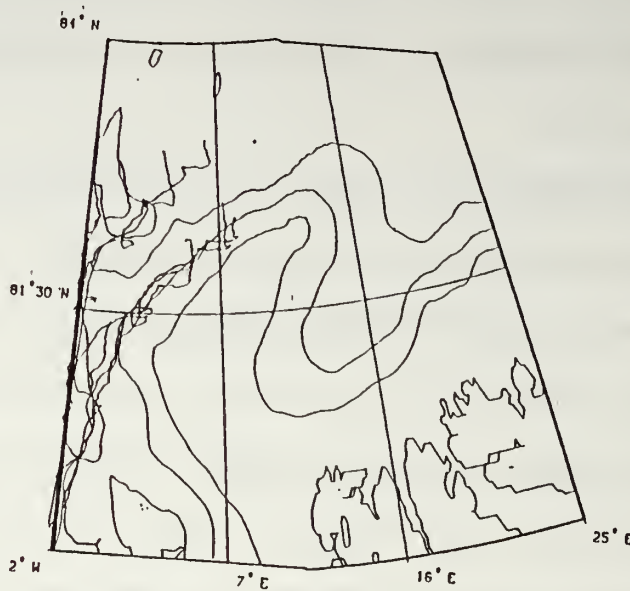
Figure 2.9 Tracks of 6 buoys that drifted in the vicinity of the Yermak Plateau during CEAREX 89.

The Mauchly criterion P_e allows a test of polarization of the envelopes. If P_e is of order of 1 it will be assumed that the envelopes are circles and the cluster analysis is consistent, i.e. data are homogeneous in the sub-areas and are correctly sampled. If P_e is small (order of 10^{-3} or less) then the method is not valid.

Among all the sub-areas only position 8 yields a strong polarization of the clockwise and counter-clockwise envelopes ($P_e = 10^{-3}$-10^{-4}) for both the '86 and '87 data. This site is the most off-shore position, and the diurnal signal there is probably too weak to be detected from the complex demodulation. Positions 13 and 14 show the same anomaly for the '87 data only. In all other sub-areas and for the two data sets P_e is between 0.2 and 0.95. The number of samples per sub-area varies from 80 to 1600. All ellipses rotate in a clockwise sense except at position 8 where the results are statistically insignificant.

36
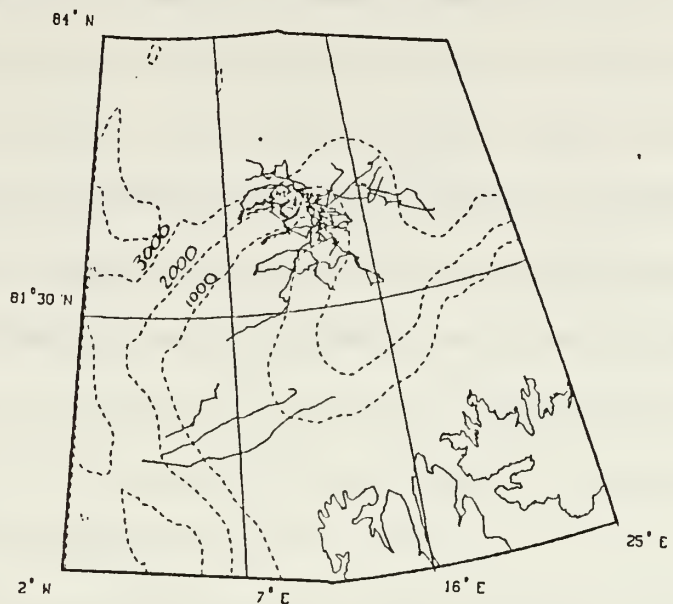
Figure 2.10 Parts of ARCTEMIZ 86/87 buoy tracks where a strong diurnal demodulated component have been found.

When applied to the ARCTEMIZ 86 and 87 data at the diurnal and semi-diurnal periods, this method shows clearly that the diurnal signal dominates the semi-diurnal signal over the plateau, both in 1986 and in 1987.

Focusing now on the diurnal part of the signal, Figure 2.11 (Figure 2.12) show the results for ARCTEMIZ 86 (87). Figure 2.13 focuses on the results for higher resolution sub-areas (Z1 to Z6) near the tip of the plateau (ARCTEMIZ 86 only). Figure 2.14 focuses on the results obtained for the CEAREX 89 buoys on the north slope of the plateau. The results are also presented in table 2.3.

The main features in these figures are:

* In terms of signal amplitude, the diurnal signal is weaker (less than 2.5 cm/s) away from the Plateau (position 8). On the nearly flat top of the Plateau (position 9) the current envelope shows an enhancement (order of 6 cm/s) in accordance with

Muench et al.'s (1990) explanation of the Gjevik and Straum model. Also the weakest polarization of the diurnal signal is found at this position in agreement with the current structure depicted by mode (1,1) in Hunkins radially symmetric model (Figure 1.8). The strongest signal for trapped motion (order of 17 cm/s) is on the slope of the plateau, especially in the vicinity of the northeast tip (Figures 2.12 and 2.13). This contradicts the Hunkins (1986) and Chapman (1989) models (positions 3, to 5 and Z1 to Z6).

* In terms of modal structure, the large amplitudes near the tip of the plateau (Figure 2.13) are for modes having a very strong across-slope polarization (positions Z2 to Z5). The largest across-slope transport occurs between the 1000 m and the 2000 m isobaths. The signal is still strong but aligned along-slope on the lower slope and the shelf break at positions Z1 and Z6.

* This across-slope polarization is correlated with the topography around the tip of the plateau as it abruptly turns south (position 6). After this southerly turn, the across-slope polarization still seems to persist on the upper slope (position 11) and tends to disappear on the lower slope (position 12). Further south on the east side of the plateau, the envelopes are not polarized, and the amplitudes decrease rapidly toward the south (position 13).

* West of the tip where the sampling is poor, the envelope (position 2) has smaller amplitudes than near the tip. CEAREX 89 data (Figure 2.14) confirm this result and

38

show an along-slope polarized current ellipse of small amplitude on the lower slope (position C3).

* Comparison between the 1986 and 1987 diurnal signals for overlapped positions does not confirm the seasonal variability found in the FFT analysis. Ellipse amplitudes are comparable in size and orientation. The difference observed in the FFT analysis between the amplitude of the diurnal energy peak in 1986 versus 1987 can be accounted for because only the '86 buoys drifted near the highly energetic region near the tip of the plateau.

TABLE 2.3 CHARACTERISTICS OF CURRENT ENVELOPES.

Area #	Number of points (86/87)	Major axis (86/87) in cm/s	Minor axis (86/87) in cm/s	P_e (86/87)	Angle of major axis (86/87)
1	72/72	6.4/8.5	7.2/3.4	10^{-6} / 0.34	129/161
2	184/0	4.0/-	2.9/-	10^{-4} /	123/-
3	205/0	12.7/-	10.8/-	10^{-2}/	129/-
4	279/0	15.7/-	12.1/-	10^{-5}/	95/-
5	423/0	10.4/-	6.0/-	$<10^{-10}$/	70/-

6	1154/183	8.2/6.3	6.2/4.6	$<10^{-10}/$ 10^{-4}	125/133
7	442/354	5.6/4.1	3.5/2.5	$<10^{-10}/$ $<10^{-10}$	93/122
8	783/367	2.1/2.9	1.8/2.2	$10^{-4}/$ 10^{-7}	177/174
9	190/186	6.2/5.6	5.3/4.8	$10^{-2}/$ 0.1	7/114
10	481/497	2.6/3.5	1.9/2.8	$<10^{-10}/$ 10^{-6}	160/167
11	509/172	4.8/4.4	3.7/2.8	$10^{-8}/$ 10^{-8}	139/129
12	1630/408	3.6/3.9	2.8/3.8	$<10^{-10}/$ 0.8	164/55
13	237/271	3.9/4.1	3.0/3.0	$10^{-4}/$ 10^{-6}	109/136
14	1277/380	3.4/4.3	2.6/3.6	$<10^{-10}$ 10^{-3}	182/155
Z1	107/0	8.9/-	7.0/-	10^{-2}	116/-
Z2	98/0	15.9/-	13.7/-	0.3	138/-

Z3	106/0	17.0/-	11.5/-	10^{-4}	111/-
Z4	173/0	15.0/-	11.7/-	10^{-3}	79/-
Z5	244/0	11.0/-	7.0/-	10^{-9}	72/-
Z6	355/0	8.0/-	4.0/-	10^{-10}	67/-
C1	40 ('89)	5.1	3.8	0.1	162
C2	691 ('89)	3.5	2.5	$<10^{-10}$	117
C3	290 ('89)	3.4	1.9	$<10^{-10}$	83

2.   Conclusions of the synoptic presentation

Two conclusions can be drawn from the synoptic presentation of the data :

* Enhanced diurnal currents are found on the Yermak Plateau and to that regard the present work confirms observations made previously (Hunkins, 1986; Hoffman, 1990).

* The new point added here is that this enhancement is not homogeneous over the plateau. The tip of the plateau and to a lesser extent the west part of it present strong currents, whereas currents are weaker on the east side. This contradicts Hunkins model (1986) that predicts uniform enhancement of diurnal currents over the plateau.

The synoptic picture presented above is somewhat puzzling. How can there be such discrepancies in the current amplitudes? How is it possible that near the tip of the plateau currents are suddenly so strong? What is the source of the kinetic energy? In order to obtain at least partial answers to these questions two models will be used: a simple analytic model and a more complex numerical model having more realistic topography.
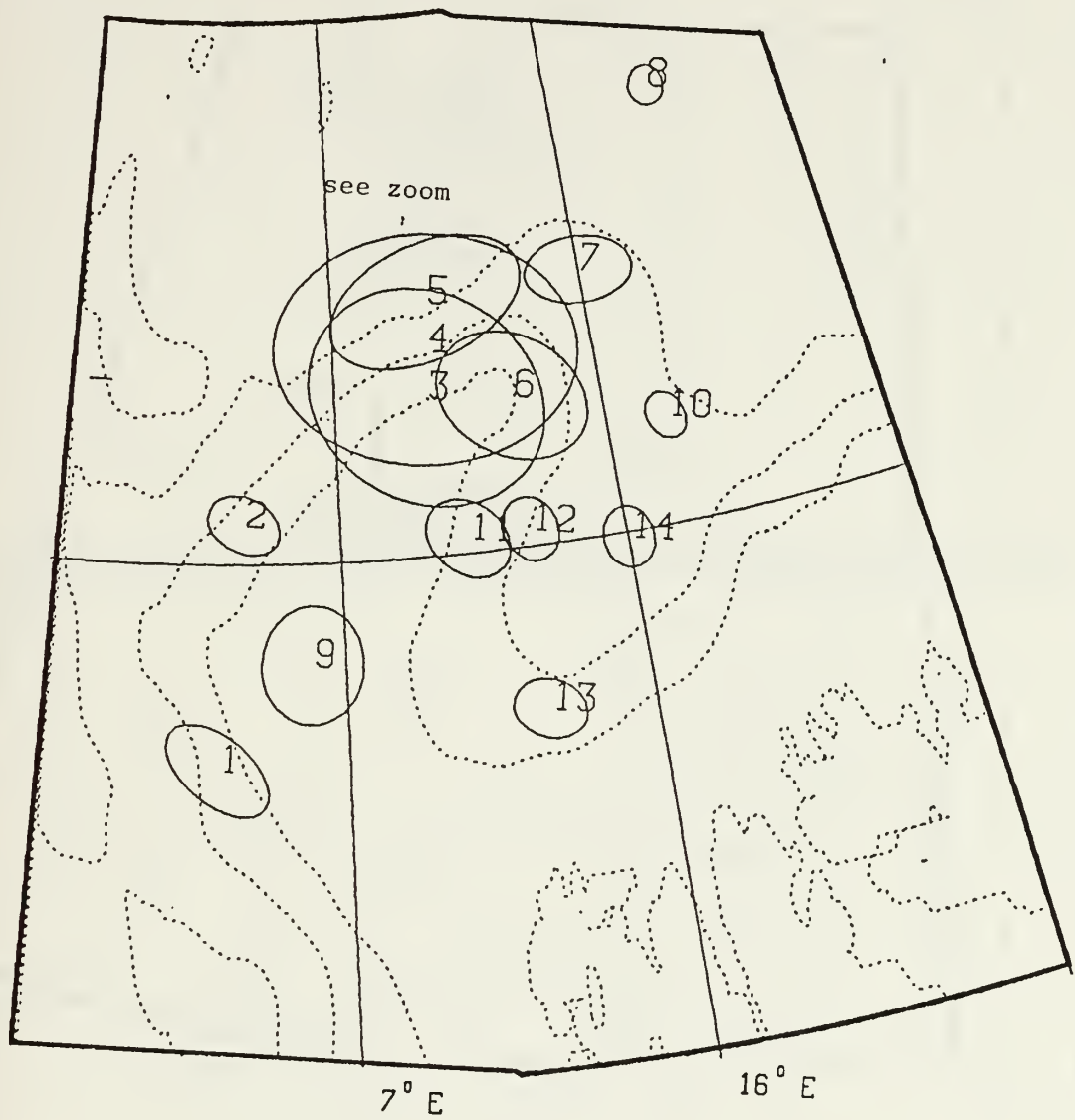
Figure 2.11 Diurnal current envelopes for ARCTEMIZ 86 buoys.
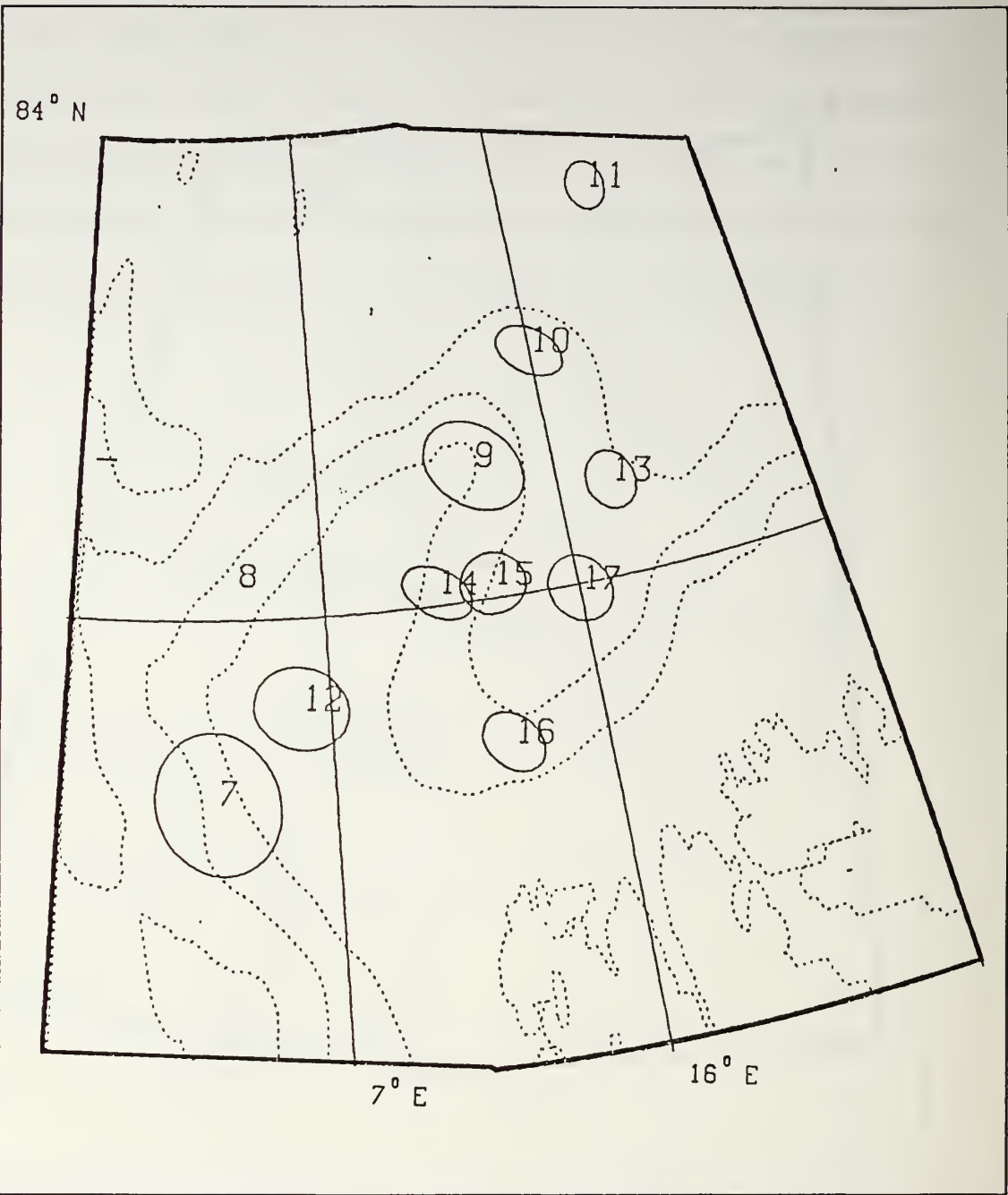
**Figure 2.12** Diurnal current envelopes for ARCTEMIZ 87 buoys.
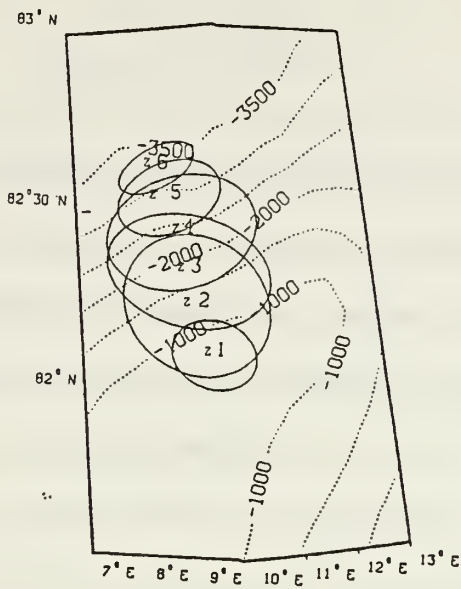
**Figure 2.13** Diurnal current envelopes near the tip of the plateau for ARCTEMIZ 86 buoys.
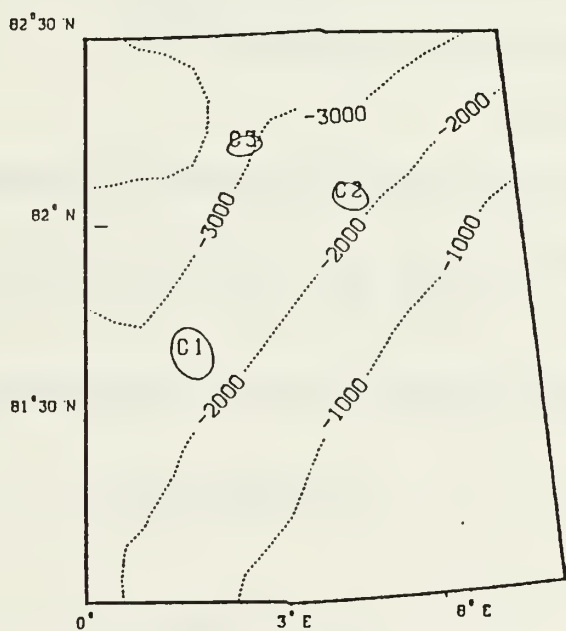
Figure 2.14 Diurnal current envelopes for CEAREX 89 buoys.

45

III ANALYTIC MODEL.

A.   THE SAINT-GUILY MODEL FOR SHELF WAVES

The analytic model to be used here was developed by Saint-Guily (1976). This model has been applied to the Southern Weddell Sea by Middleton et al. (1982 and 1987). The model yields an analytic solution for waves trapped by topographic features having cross sections similar to the bathymetric profiles across the Yermak Plateau. The original development by Saint-Guily (1976) provided only minimal details on the derivation of the analytic model. Middleton et al. (1982) added significantly to the details, but there were some typographical errors. Hence, presented below is a corrected complete model derivation.

The model assumptions are:

- small Rossby number: neglect the non-linear term

- small Ekman number: neglect stress terms

- barotropic ocean

- topography profile constant in the along-shelf x direction

- shelf extended to infinity in the across-shelf y direction

The linearized equations for a shallow water barotropic fluid on an f-plane are:

$$\frac{\partial u}{\partial t} - fv = -g\frac{\partial \eta}{\partial x} + \frac{1}{\rho h}(\tau_x^S - \tau_x^B) \tag{3.1}$$

$$\frac{\partial v}{\partial t} + fu = -g\frac{\partial \eta}{\partial y} + \frac{1}{\rho h}(\tau_y^S - \tau_y^B) \tag{3.2}$$

46

$$\frac{\partial \eta}{\partial t} + \frac{\partial hu}{\partial x} + \frac{\partial hv}{\partial y} = 0 \qquad (3.3)$$

where u and v are velocities in the x (directed eastward) and y (directed northward) directions, f is the local inertial frequency, g is gravity, η is the sea surface displacement, and h is the ocean depth which varies in the y-direction only. The surface and bottom stresses $\tau_{x,y}^{S}$ and $\tau_{x,y}^{B}$ are set to zero (small Ekman number). These equations are non-dimensionalized by the slope scale width a, the time scale $1/f$, and the reference depth H. Then the dimensionless depth profile is $q(y)=h(y)/H$.

In dimensionless form equations (3.1) to (3.3) become:

$$\frac{\partial u}{\partial t} - v = -(\frac{g}{f^2 a})\frac{\partial \eta}{\partial x} \qquad (3.4)$$

$$\frac{\partial v}{\partial t} + u = -(\frac{g}{f^2 a})\frac{\partial \eta}{\partial y} \qquad (3.5)$$

$$\frac{\partial qu}{\partial x} + \frac{\partial qv}{\partial y} = -\frac{a}{H}\frac{\partial \eta}{\partial t} \qquad (3.6)$$

Eliminating velocities from equations (3.4) to (3.6) leads to:

$$[\frac{\partial}{\partial y}(q\frac{\partial}{\partial y}) + q\frac{\partial^2}{\partial x^2}]\frac{\partial \eta}{\partial t} - \kappa(\frac{\partial^2}{\partial t^2} + 1)\frac{\partial \eta}{\partial t} + \frac{\partial q}{\partial y}\frac{\partial \eta}{\partial x} = 0 \qquad (3.7)$$

where $\kappa = f^2 a^2/gH$ is the divergence parameter. Assuming a solution of the form:

$$\eta = e^{i(kx - \omega t)}\psi(z) \qquad (3.8)$$

where:

$$z = \int \frac{1}{q(y)} dy$$

equation (3.7) becomes

$$\frac{d^2\psi}{dz^2} - [\kappa(1-\omega^2)q + \frac{k}{\omega}\frac{dq}{dz} + k^2q^2]\psi(z) = 0 \qquad (3.9)$$

The shelf profile is implicitly mapped by:

$$q = 1 + \lambda tanh z \qquad (3.10)$$

$$y = z + \lambda \ln(cosh z) \qquad (3.11)$$

where λ is the slope parameter.

With the transformation of variables,

$$\xi(z) = \frac{1}{2}(1 - tanh z) \qquad (3.12)$$

$$\psi(z) = \xi^n(1-\xi)^m\phi(\xi) \qquad (3.13)$$

Equation (3.9) becomes:

$$\xi(1-\xi)\frac{d^2\phi}{d\xi^2} + [1 + 2n - 2(n+m+1)\xi]\frac{d\phi}{d\xi} - [(n+m)(n+m+1) - p]\phi = 0 \qquad (3.14)$$

where

48

$$2n = [k^2(1-\lambda)^2 + \kappa(1-\omega^2)(1+\lambda)]^{\frac{1}{2}} \tag{3.15}$$

$$2m = [k^2(1-\lambda)^2 + \kappa(1-\omega^2)(1-\lambda)]^{\frac{1}{2}} \tag{3.16}$$

$$p = k^2\lambda^2 - k\frac{\lambda}{\omega} \tag{3.17}$$

The solution for ψ is

$$\psi(z) = \xi^n(1-\xi)^m F(\alpha,\beta,\gamma,\xi) \tag{3.18}$$

where

$$\phi = F(\alpha,\beta,\gamma,\xi) = 1 + \frac{\alpha\beta}{\gamma}\xi + \frac{\alpha(\alpha+1)\beta(\beta+1)}{2!\gamma(\gamma+1)}\xi^2 + \dots \tag{3.19}$$

is the hypergeometric function with arguments:

$$2\alpha = 2n + 2m + 1 + (1+4p)^{\frac{1}{2}} \tag{3.20}$$

$$2\beta = 2n + 2m + 1 - (1+4p)^{\frac{1}{2}} \tag{3.21}$$

$$\gamma = 2n + 1 \tag{3.22}$$

In order to keep ψ finite as $\xi \to 1$, Φ itself must remain finite which implies that F is reduced to a polynomial of order s, having

$- \beta = s$, s = 0, 1, 2, ...

49

The dispersion relation comes from equation (3.21). Writing

$$\omega = \omega_0 + \kappa \omega_1 + O(\kappa^2) \tag{3.23}$$

gives

$$\omega_0 = -\frac{k\lambda}{k^2(1-\lambda^2) - k(2s+1) + s(s+1)} \tag{3.24}$$

$$\omega_1 = \frac{\omega_0^2(1-\omega_0^2)}{2k\lambda}(2 - \frac{2s+1}{k}) \tag{3.25}$$

where s is the mode number.

the currents are given by equations (3.4) and (3.5). Assuming:

$$(u,v)(x,y,t) = (U,V)(y)e^{i(kx-\omega t)} \tag{3.26}$$

$$V(y) = \frac{g}{f^2 a}\frac{i}{1-\omega^2}[\omega\frac{\partial\psi}{\partial y} - k\psi] \tag{3.27}$$

$$U(y) = \frac{g}{f^2 a}\frac{1}{1-\omega^2}[\frac{\partial\psi}{\partial y} - \omega k\psi] \tag{3.28}$$

and using the change of variables (3.10) to (3.12) we obtain:

$$U(y) = -\frac{g}{f^2 a}\frac{1}{1-\omega^2}[\frac{sech^2 z}{2q}\frac{\partial\psi}{\partial\xi} + \omega k\psi] \tag{3.29}$$

$$V(y) = -\frac{g}{f^2 a}\frac{i}{1-\omega^2}[\omega\frac{sech^2 z}{2q}\frac{\partial\psi}{\partial\xi} + k\psi] \tag{3.30}$$

When the two components of the current have the same sign the current vector rotates clockwise. It rotates counter-clockwise when the current components are of opposite sign.

50

B.   APPLICATION TO THE YERMAK PLATEAU

Applying Saint-Guily's model to the Yermak Plateau may be in violation of the model assumption that the depth profile is constant in x (along shelf). This assumption would certainly be inappropriate for long waves with wavelengths larger than the spatial scale of the plateau (500 km). In that case the use of Hunkins' radially-symmetric model would be more appropriate. For short waves, however, the Saint-Guily model can give better results.

As a consequence of these limitations the results of the analytic study presented below will be considered qualitative and not as accurate predictive values. The Saint-Guily model will be applied to two depth profiles with locations shown on Figure 3.1.

The first profile selected is on the northern slope of the plateau. A best fit to the actual profile is found using a least-mean square method. The shelf parameters are H = 2333 m, a = 30,000 m and λ = 0.73. The second profile is on the eastern side of the plateau. At this location the curvature of the isobaths is important and the model assumption of constant topography profile is probably violated. The shelf parameters are H = 1444 m, a = 30,000 m and λ = 0.56. Figure 3.2 displays the dispersion diagram of mode 1 computed with the two profiles. Higher modes have cut-off frequencies far below the diurnal band at either location. It appears that the cutoff frequency is below the K_1 frequency for the lowest value of λ corresponding to the second profile because the topography is too gentle at this location. For profile 1 the wavelengths for the K_1 period are K_+ = O(6400 km) and K_- = O(200 km).

A sensitivity study of the influence of the slope parameter λ reveals that these wavelengths may vary significantly with λ, while the agreement between the idealized profile defined by λ and the actual profile remains acceptable:
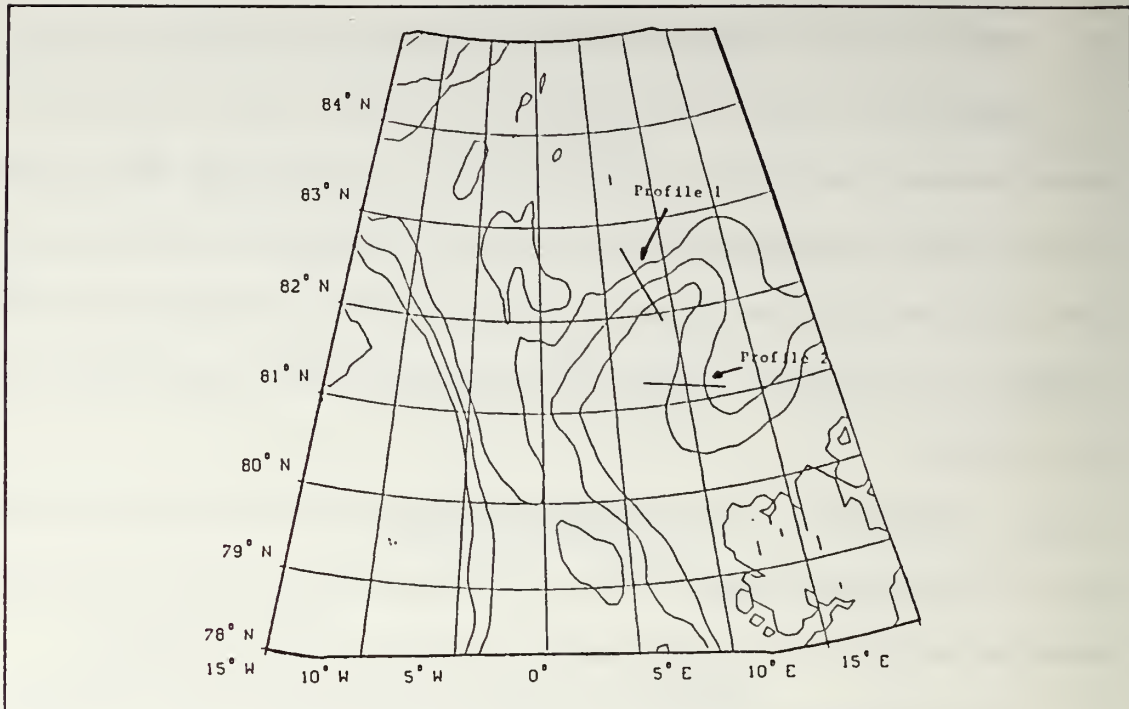
**Figure 3.1** Location of two shelf profiles.
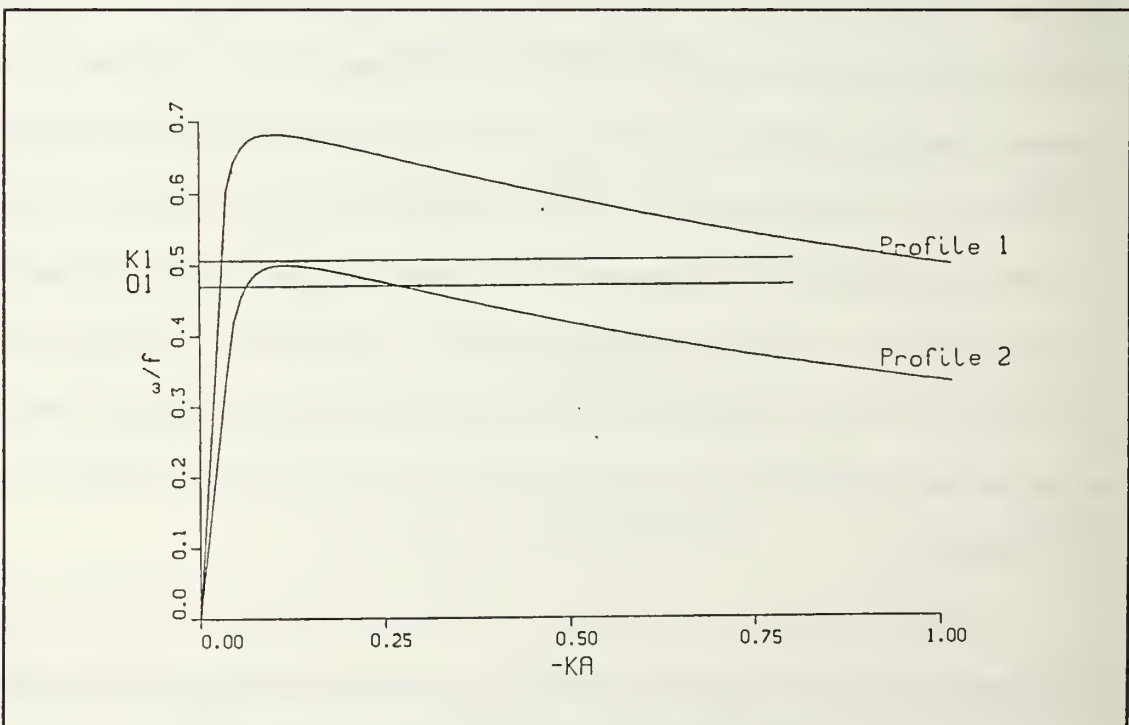
Figure 3.2 Dispersion curves for $\lambda = 0.73$ and 0.56, for the first mode (s=0).

52

* At the K_1 period the short wave wavenumber corresponding to a negative group velocity varies by 50% in magnitude from O(150 km) to O(200 km) for λ varying from 0.65 to 0.70.

* The long wave varies by 5% from O(6000 km) to O(6400 km) under the same conditions.

Figure 3.3 displays the computed currents and surface displacement corresponding to the first mode at the two wavenumbers K_+ and K_- for $\lambda = 0.73$ (profile 1). This figure shows that the short wave is most effectively trapped on the slope (bottom frame), with a large across-slope current component. By contrast, the currents associated with the long wave (middle frame) are stronger on the flat top of the plateau than they are on the slope.

Four conclusions can be drawn:

* The low wavenumber K_1 period CTW has a spatial scale that exceeds the width of the plateau. The curvature of the plateau is then likely to play a role in the propagation of the tidal energy. In that regard, Hunkins' model is probably more appropriate.

* The limitation of Hunkins' model comes from the assumption of radially symmetric topography. Hunkins' model predicts uniform enhancement of the diurnal currents over the plateau, in contradiction with the synoptic description obtained in the section "Data Analysis." The above study shows that if the plateau were straight, a diurnal period CTW

53

could not propagate on the eastern part of the plateau because the slope of the topography is too weak. Therefore a CTW at the K_1 period can propagate around the plateau starting from Fram Strait along the west and north side but cannot penetrate further than approximately the tip of the plateau. The tidal energy carried by the incident CTW is scattered when the CTW reaches the region where the slope is too gentle to support the wave. Part of the energy is transmitted in evanescent form further downshelf but most of it is reflected and carried by a negative group speed short CTW at the K_1 period (see section E.2 in the "Introduction": "Scattering of CTW with bottom friction"). The Saint-Guily model shows that the current speeds associated with the incident long wave are larger on the top of the slope, whereas the currents associated with the reflected short wave are stronger and trapped on the slope of the plateau. Up-shelf of the scattering zone the current structure of the reflected wave is superimposed on the current structure of the incident wave. Bottom friction that is not included in the Saint-Guily model now comes into play. Wang (1980) and Schwing (1989) showed that bottom friction is very efficient at dissipating a low group speed short CTW. The decay scale of this short wave is of the order of a shelf width. Hence the influence of the reflected wave is restricted to a limited region up-shelf of the scattering zone.

The above explanation is in accordance with the synoptic description of the diurnal currents. On the west side of the plateau the largest ellipse is on the top of the plateau and near the tip it is on the slope with stronger currents and large across-slope transport.

* One notes that the observed strong across-slope velocity region (Figure 2.11) is in fact located significantly up-shelf from profile 2. It is therefore likely that the scattering is

also due to the sharp turn of the shelf near the tip of the plateau with spatial scale very short compared to the scale of the incident wave.

* Finally, tidal energy cannot propagate on the eastern side of the plateau according to Saint- Guily model. Nonetheless, the narrow width of the Yermak Plateau does allow a coupling between the western and the eastern sides. A continuous forcing on the eastern side can be applied by the velocity structure of the incident wave on the western side.

C.   CONCLUSIONS FROM THE ANALYTIC INVESTIGATION

The analytic model is able to confirm one point and to answer one question:

* it confirms the finding by Hunkins (1986) that the west and north slopes of the Yermak Plateau can support CTW at the K_1 period.

* it partially explains why the enhancement of diurnal currents is not uniform over the plateau because of the change in the topography.

However the analytic model does not take the actual topography into account. The change in the curvature of the topography may induce scattering an incident CTW. Such a scattering effect is to be expected, for example where the rather straight north side of the plateau turns sharply to form the tip of the plateau. The structure of an incident CTW must adjust to the strong curvature of the topography.

In this study the scattering effect is amplified by two factors:

* firstly, the ocean is barotropic and the CTW are frequency limited

* secondly, the K_1 frequency is far above the cut-off frequency of modes higher than mode 1

These two factors limit the possibilities of adjustment by a CTW. In general the incident energy is redistributed among several modes having positive and negative group speeds. In the case of the Yermak Plateau and an incident wave at the K_1 frequency, the incident energy can only be redistributed between the mode 1 of a transmitted wave possibly in evanescent form and a reflected short wave.

Hence a numerical model is needed to take the full effect of the topography into account.
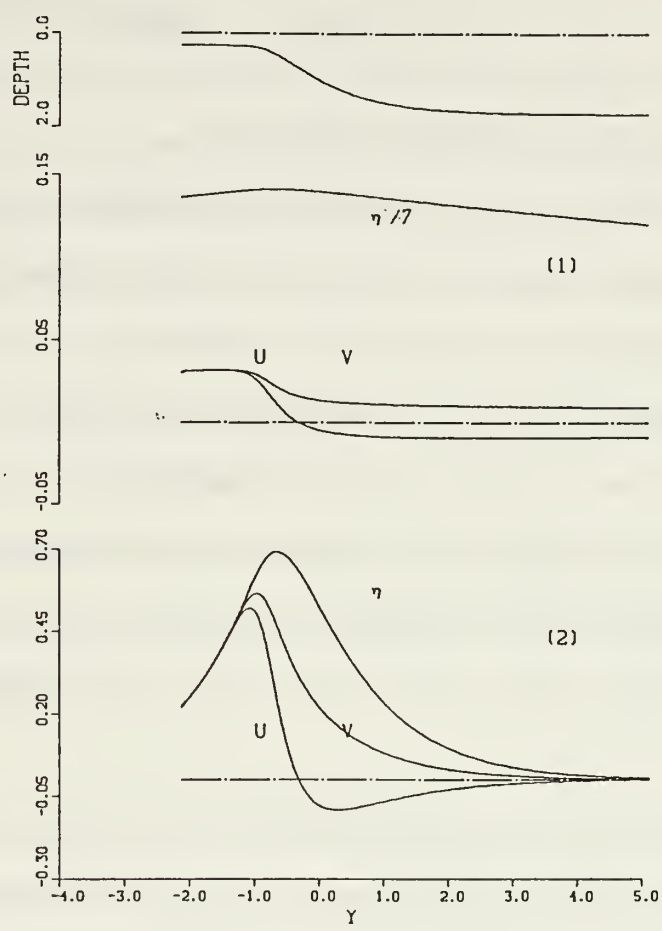
Figure 3.3 Idealized shelf profile (top) for $\lambda = 0.73$, velocities and surface elevation at the diurnal period for long wave (middle) and short wave (bottom).

IV. NUMERICAL MODEL

A.   GENERAL EXPLANATION OF THE MODEL

A linear barotropic model developed by Schwing (1989) was used to investigate the anomalous diurnal currents found in the vicinity of the Yermak Plateau. The bottom topography was smoothed, but the plateau is realistically represented. The coast lines of Svalbard were simplified. An iterative technique was used to compute the surface elevation field. This field is the approximate solution of an elliptic equation obtained from the two-dimensional, linearized, shallow water barotropic equations of motion and continuity. Free surface and free slip boundary conditions were specified at the surface and at the coast respectively. Bottom friction was linearized using a linear depth-dependent friction coefficient.

The model assumes a sinusoidal time dependence for each variable. The frequency of oscillation of the variables is a parameter to be specified. The model is solved at several frequencies to show the spectral dependence of the Yermak Plateau region to a range of frequencies.

The tide potential was neglected since the spatial scales of the Yermak Plateau are small compared to the scale of this potential. The forcing consists of an incident topographic wave trapped on the western side of Svalbard and heading north. This simple representation of the tide is consistent with Schwiderski (1986) and Gjevik and Straum (1989) (see Introduction).

B. DESCRIPTION OF THE MODEL

1. The model topography

The Digital Bathymetry Data Base 5 m (DBDB5) provides a topography field with a spatial resolution of 5 minutes in latitude and longitude. When compared to maps derived from more precise or more recent data, the topography given by DBDB5 shows some small to medium scale discrepancies especially in the vicinity of the northeastern tip of the plateau.

In order to obtain depth values on a rectangular regular mesh for model integration, the following processes were used:

* First, the bathymetry field was mapped using a Polar Azimuthal Equidistant projection (USGS 1395, 1987) centered on the plateau (81.5°N, 007°E), using the polar radius of curvature.

* The orientation of the map axes was rotated by 30° counter-clockwise in order to have an x axis approximately normal to the west coast of Svalbard. This last step simplifies the forcing condition at the northern exit of Fram Strait.

* The International Mathematical Subroutine Library (IMSL) interpolation routine SURF was used to transform the irregular projected field onto a rectangular field having a fixed resolution of 5 km.

* The coast lines of Svalbard are idealized as straight lines. The IMSL routine SURF was used to adjust the shelf topography with the simplified coast lines. With the

model coastline approximately as a wall at the 100 m depth contour, SURF fills the region between the 200 m isobath and the coast with interpolated values.

* Finally, the interpolated topography is smoothed for stability because the numerical model is overly sensitive to abrupt changes of topography. Smoothing is performed with a weighted 3 x 3 spatial filter such that:

$$h_{i,j}^{smoothed}=(h_{i+1,j}+h_{i+1,j+1}+h_{i,j+1}+h_{i-1,j+1}+h_{i-1,j}+h_{i-1,j-1}+h_{i,j-1}+h_{i+1,j-1}+5h_{i,j})/13$$

Small areas where the interpolation routine introduces noise are also smoothed locally with lower order spatial filters.

The final array is a 100 x 92 matrix with resolution 5 km both in x and y. The domain spatial dimension is 495 x 455 km. The projected smoothed bathymetry is displayed in Figure 4.1. The bottom left corner of the domain corresponds to the position 79°N, 00°E.

2.   Derivation of a single governing equation

This section generally follows the work of Schwing (1989).

The two dimensional, linearized, shallow water barotropic equations of motion and continuity are:

60
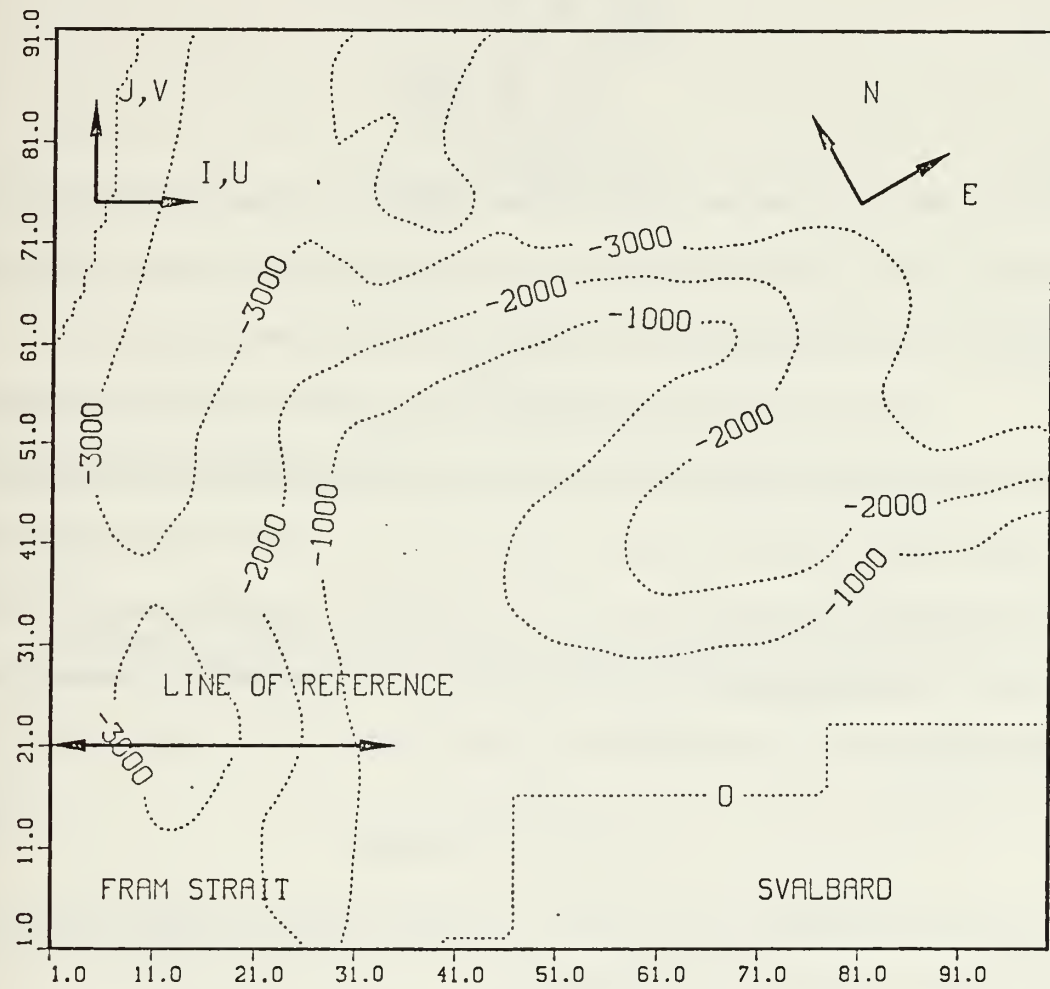
Figure 4.1 Domain and bathymetry in Yermak plateau numerical simulations.

$$\frac{\partial u}{\partial t} - fv = -g\frac{\partial \eta}{\partial x} + \frac{1}{\rho h}(\tau_x^S - \tau_x^B) \qquad (4.1)$$

$$\frac{\partial v}{\partial t} + fu = -g\frac{\partial \eta}{\partial y} + \frac{1}{\rho h}(\tau_y^S - \tau_y^B) \qquad (4.2)$$

$$\frac{\partial \eta}{\partial t} + \frac{\partial uh}{\partial x} + \frac{\partial vh}{\partial y} = 0 \qquad (4.3)$$

where u and v are depth-averaged velocities, η is the sea surface elevation, h the bottom depth, τ_x^S and τ_y^S are the components of the surface stress in the x and y direction, and τ_x^B and τ_y^B are the components of the bottom stress in the x and y direction.

Forcing will come from lateral inflow boundaries. Following the simplification made in the analytic model the influence of atmospheric forcing is not considered in this numerical study. Hence the surface stress is set to zero. However, bottom friction which was neglected in the analytic model, is imposed in the numerical model. To be able to derive a set of linear governing equations, bottom stress is linearized following Clarke and Brink (1985):

$$\tau_{x,y} = \rho r(u,v) = \rho C_D U_{ref}(u,v) \qquad (4.4)$$

where U_{ref} is a reference velocity above the bottom, and C_D is a bottom drag coefficient. Equations (4.1) and (4.2) are then rewritten:

$$\frac{\partial u}{\partial t} - fv = -g\frac{\partial \eta}{\partial x} - \frac{ru}{h} \qquad (4.5)$$

$$\frac{\partial v}{\partial t} + fu = -g\frac{\partial \eta}{\partial y} - \frac{rv}{h} \qquad (4.6)$$

with $r = C_D U_{ref}$.

Harmonic time dependence of the form $e^{i\omega t}$ is assumed for all time derivatives, where ω is the frequency of the lateral boundary forcing. Then equations (4.5) and (4.6) yield current components:

$$u = \frac{1}{1+\epsilon^2}[-\frac{g}{f}(\epsilon\frac{\partial\eta}{\partial x}+\frac{\partial\eta}{\partial y})] \tag{4.7}$$

$$v = \frac{1}{1+\epsilon^2}[\frac{g}{f}(\frac{\partial\eta}{\partial x}-\epsilon\frac{\partial\eta}{\partial y})] \tag{4.8}$$

with:

$$\epsilon = i\frac{\omega}{f}+\frac{r}{fh} \tag{4.9}$$

Substituting equations (4.7) and (4.8) into the continuity equation (4.3) gives the governing equation:

$$\frac{a^2\epsilon}{1+\epsilon^2}\nabla^2\eta+[\frac{\partial}{\partial x}(\frac{a^2\epsilon}{1+\epsilon^2})-\frac{\partial}{\partial y}(\frac{a^2}{1+\epsilon^2})]\frac{\partial\eta}{\partial x}+[\frac{\partial}{\partial x}(\frac{a^2}{1+\epsilon^2})+\frac{\partial}{\partial y}(\frac{a^2\epsilon}{1+\epsilon^2})]\frac{\partial\eta}{\partial y}-i\frac{\omega}{f}\eta=0 \tag{4.10}$$

where $a^2 = gh/f^2$. Equation (4.10) is an elliptic partial differential equation in terms of the variable η.

3.   Boundary conditions

  a.   *Non-forcing boundary conditions*

       Open boundaries are set on the approximately eastern (x = 100), northern (y = 92) and western (x=0) sides of the domain. Following Schwing (1989) the radiative conditions are:

$$\frac{\partial^2 \eta}{\partial x^2} = 0 \qquad\qquad (4.11)$$

$$\frac{\partial^2 \eta}{\partial y^2} = 0 \qquad\qquad (4.12)$$

respectively for the western and eastern side (x = 0 and 100) and the northern side (y = 92). These are empirical radiative conditions that allow absorption of incoming waves at the boundary with little or no reflection of energy. These conditions may affect the solutions inside the domain within a few grid points from the boundary. However, this effect was not noticeable in the present study (Hsueh, 1980; Hopkins et al., 1983).

At the coast the condition is no flow normal to the coast. Equations (4.7) and (4.8) provide:

$$\epsilon \frac{\partial \eta}{\partial x} + \frac{\partial \eta}{\partial y} = 0 \qquad\qquad (4.13)$$

$$\frac{\partial \eta}{\partial x} - \epsilon \frac{\partial \eta}{\partial y} = 0 \qquad\qquad (4.14)$$

for coastlines normal to x $(u = 0)$ and to y $(v = 0)$, respectively.

b.   Forcing boundary condition

In order to represent a forcing similar to the tide propagating from south to north through Fram Strait and incident on the Yermak Plateau, the southern side of the domain (y = 0) is continually forced by a CTW. The mathematical details are given in Appendix D. Since the structure of this forcing wave is not in perfect equilibrium with respect to the actual bathymetry, the model wave requires several grid steps of along-shelf to bring the idealized incoming wave into equilibrium.

This adjustment as impedance-matching does not influence significantly the model solution in the interior of the domain. To minimize the effects of this adjustment process, a position located 150 km down-shelf (y = 31) is be used as a reference of the forcing amplitude.

4. Finite difference form of the model

The governing equation (4.10) cannot be solved analytically for irregular topography. Following Schwing (1989), it can be written in a more general form:

$$p(x,y)\eta + q(x,y)\frac{\partial^2 \eta}{\partial x^2} + r(x,y)\frac{\partial \eta}{\partial x} + s(x,y)\frac{\partial^2 \eta}{\partial y^2} + t(x,y)\frac{\partial \eta}{\partial y} = 0 \qquad (4.15)$$

where:

$$q(x,y) = \frac{a^2 \epsilon}{1 + \epsilon^2}$$

$$r(x,y) = \frac{\partial}{\partial x}(\frac{a^2 \epsilon}{1 + \epsilon^2}) - \frac{\partial}{\partial y}(\frac{a^2}{1 + \epsilon^2})$$

$$s(x,y) = \frac{a^2 \epsilon}{1 + \epsilon^2}$$

$$t(x,y) = \frac{\partial}{\partial x}(\frac{a^2}{1 + \epsilon^2}) + \frac{\partial}{\partial y}(\frac{a^2 \epsilon}{1 + \epsilon^2})$$

$$p(x,y) = -i\frac{\omega}{f}$$

Equation (4.15) can now be discretized using a centered in space second order finite difference scheme, with $x = i\ \Delta x$, $i = 0,1,2,....I$ and $y = j\ \Delta y$, $j = 0,1,2,....J$, Δx and Δy being the grid spacing in the x and y directions respectively :

65

$$p_{i,j}\eta_{i,j}+q_{i,j}(\frac{\eta_{i+1,j}-2\eta_{i,j}+\eta_{i-1,j}}{\Delta x^2})+r_{i,j}(\frac{\eta_{i+1,j}-\eta_{i-1,j}}{2\Delta x})+s_{i,j}(\frac{\eta_{i,j-1}-2\eta_{i,j}+\eta_{i,j+1}}{\Delta y^2})$$

$$+t_{i,j}(\frac{\eta_{i,j+1}-\eta_{i,j-1}}{2\Delta y})+O(\Delta x^2+\Delta y^2)=0 \qquad (4.16)$$

Rearranging (4.16) in terms of $\eta_{i,j}$ leads to:

$$a_{i,j}\eta_{i+1,j}+b_{i,j}\eta_{i-1,j}+c_{i,j}\eta_{i,j-1}+d_{i,j}\eta_{i,j+1}+e_{i,j}\eta_{i,j}=0 \qquad (4.17)$$

where:

$$a_{i,j}=q_{i,j}+\frac{\Delta x}{2}r_{i,j}$$

$$b_{i,j}=q_{i,j}-\frac{\Delta x}{2}r_{i,j}$$

$$c_{i,j}=\delta^2 s_{i,j}-\delta\frac{\Delta x}{2}t_{i,j}$$

$$d_{i,j}=\delta^2 s_{i,j}+\delta\frac{\Delta x}{2}t_{i,j}$$

$$e_{i,j}=\Delta x^2 p_{i,j}-2q_{i,j}-2\delta^2 s_{i,j}$$

$$\delta=\frac{\Delta x}{\Delta y}$$

The finite difference forms of the boundary conditions are:

* for the northern side (y = 92, j = J) equation 4.13 yields

66

$$\frac{\eta_{i,J+1}-2\eta_{i,J}+\eta_{i,J-1}}{\Delta y^2}=0$$

This expression defines a fictitious surface elevation $\eta_{i,J+1}$ at a point lying outside the domain:

$$\eta_{i,J+1}=2\eta_{i,J}-\eta_{i,J-1}$$

Substituting this expression into the governing equation (4.17) leads to an expression for $\eta_{i,J}$ in terms of the surface elevation at the surrounding grid points within the domain:

$$\eta_{i,J}=\frac{-1}{e_{i,J}+2d_{i,J}}(a_{i,J}\eta_{i+1,J}+b_{i,J}\eta_{i-1,J}+(c_{i,J}-d_{i,J})\eta_{i,J-1}) \tag{4.18}$$

Similar expressions can be obtained for grid points lying on the eastern and western sides of the domain. For the northeastern and northwestern corners equations (4.11) and (4.12) are used simultaneously.

* For a coast normal to the x direction from (I0, j-1) to (I0, j+1) with point (I0-1, j) lying inland, equation 4.13 yields:

$$e_{I0,j}\frac{\eta_{I0+1j}-\eta_{I0-1j}}{2\Delta x}+\frac{\eta_{I0j+1}-\eta_{I0j-1}}{2\Delta y}=0 \tag{4.19}$$

which is used to express $\eta_{I0-1,j}$:

$$\eta_{I0-1,j}=\eta_{I0+1,j}+\frac{\delta}{e_{I0,j}}(\eta_{I0j+1}-\eta_{I0j-1}) \tag{4.20}$$

Substituting (4.20) into (4.17) yields:

$$\eta_{10,j} = \frac{1}{e_{10,j}} [\eta_{10,j-1} (b_{10,j} \frac{\delta}{e_{10,j}} - c_{10,j}) - \eta_{10,j+1} (b_{10,j} \frac{\delta}{e_{10,j}} + d_{i,j}) - \eta_{10+1,j} (a_{10,j} + b_{10,j})] \qquad (4.21)$$

Following a similar treatment, finite difference forms of the coastal boundary conditions are found for all possible geometries of the coast: normal to the y direction, corner headland, and corner cove.

5.   The sequential overrelaxation (SOR) solver

    a.   *Description of the SOR method*

SOR is a well-documented iterative technique designed to solve elliptic-type partial differential equations (i.e. Haltiner and Williams, 1980, p. 157; Smith, 1985, p. 262).

For simplicity equation (4.17) is rewritten:

$$\Gamma_{i,j} + e_{i,j} \eta_{i,j} = 0 \qquad (4.22)$$

Using the surface elevation values found at iteration n we obtain:

$$\Gamma_{i,j}^n + \eta_{i,j}^n = R_{i,j} \qquad (4.23)$$

where $R_{i,j}$ is the residual due to errors in the η-field. We now compute the value of $\eta_{i,j}^G$ such that:

$$\Gamma_{i,j} + \eta_{i,j}^G = 0 \qquad (4.24)$$

Combining (4.23) and (4.24) yields:

$$\eta_{i,j}^G = \eta_{i,j}^n - \frac{R_{i,j}}{e_{i,j}} \tag{4.25}$$

In order to make the scheme converge more rapidly, the overrelaxation parameter α is introduced (in general $1 < \alpha < 2$). Then the updated value $\eta^{n+1}_{i,j}$ is:

$$\eta_{i,j}^{n+1} = \eta_{i,j}^n + \alpha \frac{R_{i,j}}{e_{i,j}} = \alpha \eta_{i,j}^G + (1-\alpha)\eta_{i,j}^n \tag{4.26}$$

The solution converges when $\eta_{i,j}^G \approx \eta_{i,j}^n$. In this study convergence is assumed when:

$$\Sigma_{i=0}^I \Sigma_{j=0}^J |\eta_{i,j}^G - \eta_{i,j}^n| \leq 10^{-3} \tag{4.27}$$

b. The choice of the overrelaxation parameter

Schwing (1989) describes a theoretical method to choose the optimum overrelaxation parameter α. It can be shown that if the finite difference problem is posed as linear system:

$$A\eta = F$$

where A is a complex matrix of order $N = (I+1) \times (J+1)$, and F and η are both vectors of length N, then the optimum overrelaxation parameter is given by:

$$\alpha = \frac{2}{1 + (1 - \rho^2)^{1/2}}$$

Here the spectral radius ρ is the absolute value of the largest eigenvalue of A. For realistic problems that are complex this value cannot be determined exactly. However, it is possible to gradually adjust the value of α to find a near-optimum value. Several methods are available to perform this task. In this work, the Chebyshev semi-iterative method was used:

$$\alpha = 1, \qquad\qquad\qquad\qquad\qquad\qquad n = 1$$

$$\alpha = 1 / (1 - \rho /2) \qquad\qquad n = 2$$

$$\alpha = 1 / (1 - \alpha\rho /4) \qquad\qquad n > 2$$

$$\alpha \rightarrow \alpha \text{ optimum} \qquad\qquad n \rightarrow \infty$$

where n is the number of iterations.

This technique implies knowledge of ρ. The value of ρ must be determined empirically for a given problem. For this model of the Yermak Plateau, a value of ρ of the order of 0.9 or less provides for a generally rapid rate of convergence. Depending on the frequency of the forcing and the bottom friction coefficient, 6000 to 30,000 iterations are needed to satisfy the convergence criterion (4.27).

C.   MODEL RESULTS

1.   Objectives of the numerical investigation

The numerical model presented above contains several simplifications and uncertainties (topography, forcing, linearization, approximate solver) that are reasonable at first order but possibly important enough to discourage the use of the model for predictive purposes. Instead of accurate high order prediction, the model will be used here to answer the following question: does the topography/geometry of the Yermak Plateau generate a resonant response to incident wave energy in the diurnal band? In order to answer this question a sensitivity study is performed. The response of the plateau is studied as a function of the characteristics of the model: frequency and/or shape of the forcing, and bottom friction.

2.   Response of the Yermak Plateau to a monochromatic diurnal forcing

For the sake of numerical stability, the bottom friction coefficient r is set at 0.013 ms^{-1}. This represents a strong bottom friction, 10 times larger than the coefficient chosen

by Chapman (1989) in the same area. However, where the friction term is largest, at the shallowest region on the plateau (800 m), the ratio of friction to acceleration ($r/h\omega$) is order of 0.2. Hence friction does not play an important role (Chapman and Brink, 1987). Furthermore, it will be shown later that further increasing the bottom friction two-fold does not modify significantly the current features revealed by the model in the deep water above the plateau.

a.   *Distribution of the kinetic energy on the plateau*

For a monochromatic forcing at the K_1 period, Figure 4.2 is a contour plot of the kinetic energy (KE) averaged over one period and normalized by the kinetic energy of the forcing at the reference line defined in section 3-b, averaged over one period and across the shelf. This plot reveals the following:

* Kinetic energy is trapped in two regions: along the northern coast of Svalbard where it is strongly damped due to the shallow depth of the ocean, and on the plateau.

* On the plateau the contour lines of kinetic energy tend to follow closely the isobaths.

* On the top of the plateau two cells of high kinetic energy are evident. One is in the vicinity of the northwestern corner of the plateau where the average KE is five times greater than the normalizing value. The other one is near the northeastern tip of the plateau where KE is up to eight times larger than the mean KE of the input. These high-energy cells are in the proximity of strong curvatures of the isobaths.
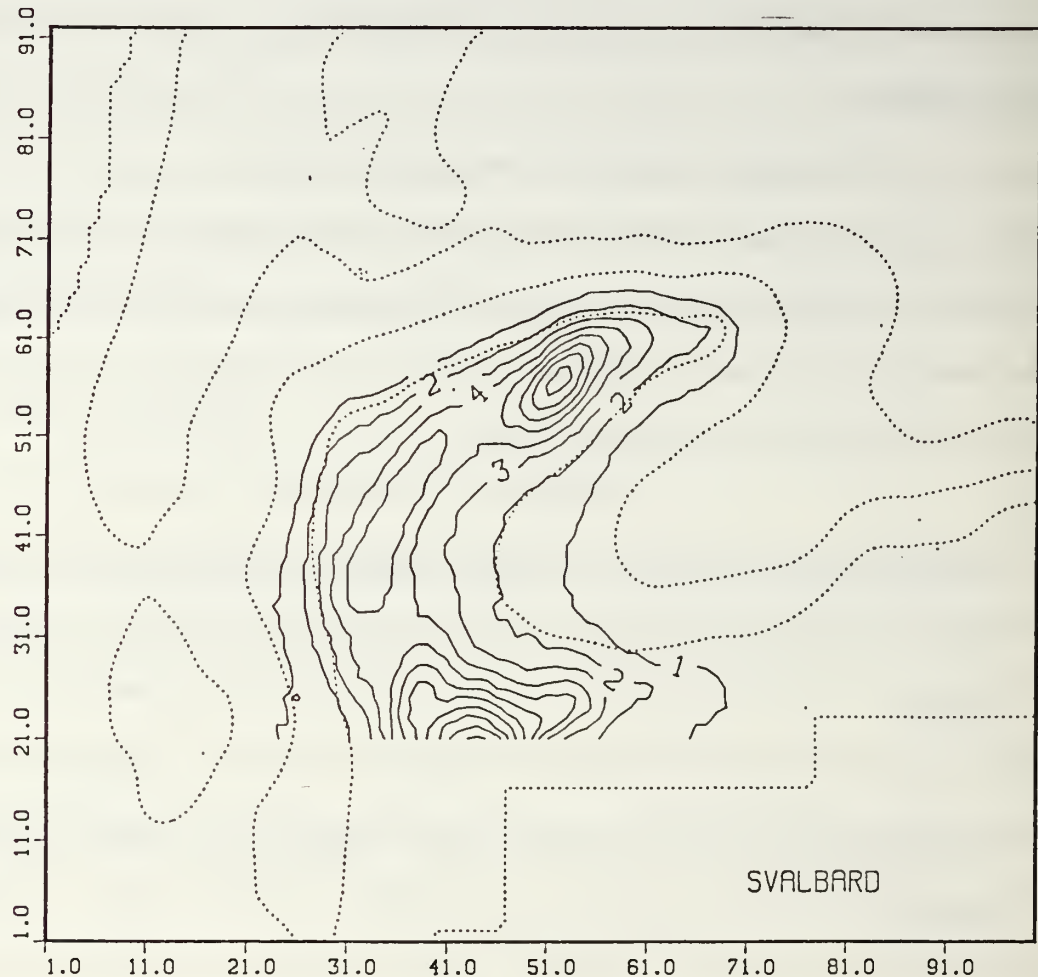
Figure 4.2 Normalized average kinetic energy at the K_1 period.

72

* The most energetic of these two cells has a small-scale oval shape. Figure 4.3 displays the amplitude of the velocities near the tip of the plateau and confirms the radial structure of the velocity field at that location. This distribution is very analogous to the current structure predicted by Hunkins for a wave trapped around a radially symmetric submerged topographic feature (see Introduction).

b. Current vector field

Snapshots of the current vector and surface elevation fields every tenth of a period over half a period are displayed in Appendix E. They reveal the paths followed by the wave energy on the plateau. The current structure is dominated by two waves:

* The first wave is trapped along the northern coast of Svalbard heading east with the coast on its right. Surface elevation iso-lines tend to be oriented parallel to the coast.

* North of Fram Strait the second wave follows the topography of the plateau with its maximum amplitude approximately on the 1,000 m isobath. As indicated by the kinetic energy plots (western corner cell) this wave experiences some scattering while propagating around the western corner. The wave then follows the northern side of the plateau until it reaches the plateau's eastern tip. Because of the very sharp turn of the topography and the flattening of the shelf south of the tip, the wave cannot propagate further down-shelf.
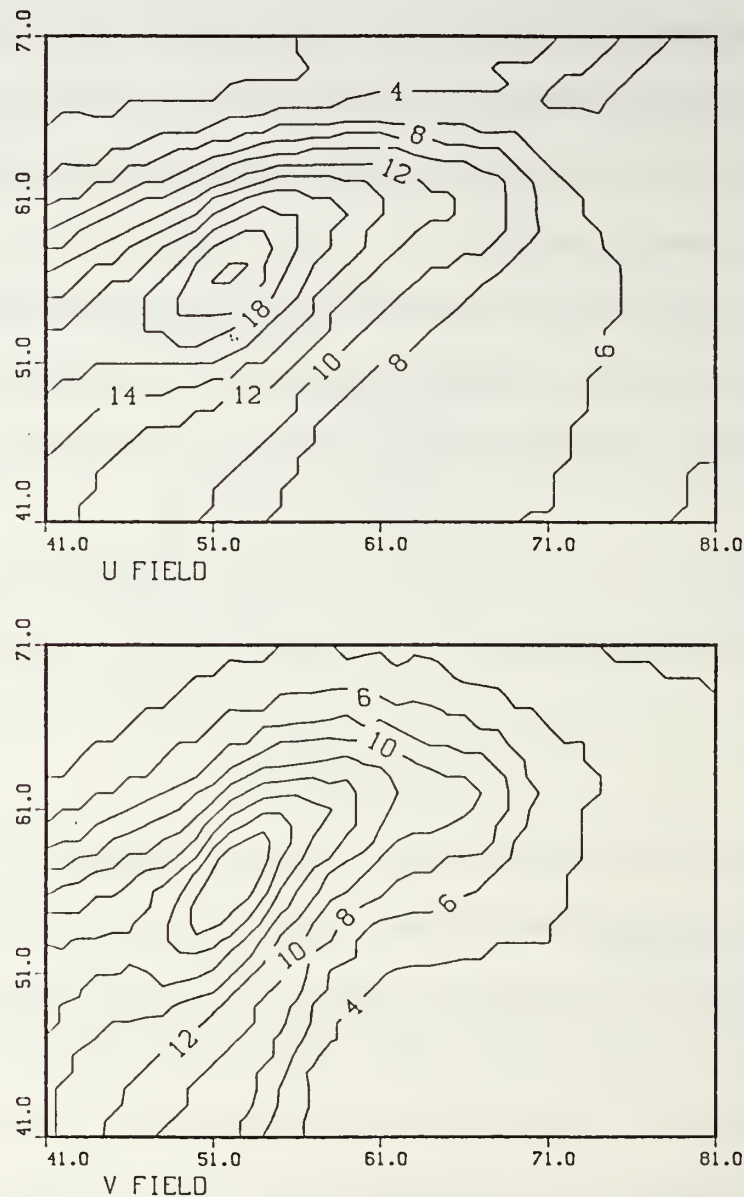
Figure 4.3 Velocity fields near the tip of the plateau. K_1 forcing. Contour lines are drawn every 2 cm/s.

* On the eastern side of the plateau, where the wave described above does not penetrate, currents are dominated by both the wave heading east along Svalbard and the current structure of the wave following the 1,000 m isobath on the western side of the plateau.

c.   *Comparison with the observed data*

The numerical model reproduces reasonably well the features found in the data analysis and the analytic model:

* currents are strong on the plateau and weak in deep waters.

* the amplitude of the diurnal current varies significantly over the plateau. The current enhancement is not uniform.

* the strongest currents are found near the tip of the plateau with amplitudes of the order of 20 cm/s in accordance with the data. Strong currents are also found on the western side of the plateau. By contrast, currents are weak on the eastern side of the plateau.

* current ellipses computed with the model outputs (not shown) rotate in a clockwise sense except far off the plateau.

* the model predicts strong currents on the top of the plateau near the tip whereas the data as well as the analytic model showed these currents trapped on the slope.

3. Sensitivity to model parameters

The model result described in the previous section is not very sensitive to changes of the major model parameters:

* Slight changes in the forcing frequency do not lead to any significant modifications of the current features described above. The frequency dependence of the response of the plateau will be discussed later.

* In order to test the influence of the shape of the forcing on the response of the plateau the modal structure of the forcing wave is changed. Instead of a shelf wave-structured forcing, a uniform surface elevation oscillating in time is imposed across the lower boundary. The response on the plateau is not changed.

* Finally, as mentioned in the previous section, the influence of bottom friction coefficient is evaluated by increasing this coefficient. When bottom friction is increased by a factor of 2, the model gives the same general current structure. The two cells of high kinetic energy previously described (Figure 4.2) are clearly present at the same locations, but their normalized magnitudes are decreased. Their non-dimensional magnitudes decrease from 5 to 4 for the western corner cell, and from 8 to 3 for the tip cell. The stronger decay in the second cell is due to the fact that the tip is further down-shelf so that the incident wave experiences more damping before reaching that position.

This sensibility study demonstrates the robustness of the model. On the plateau the predicted current structure has only minor alterations with changes in the model parameters. Therefore the model is a fairly good representation of the physical processes

affecting circulation on the Yermak Plateau. The strong friction parameter required for numerical stability probably leads to an under estimation of the current magnitudes near the tip relative to the current magnitudes on the western side of the plateau.

4.   Response of the Yermak plateau at other frequencies

Changing the frequency of the monochromatic forcing allows study of the response of the Yermak Plateau to forcing frequency. It appears that current enhancement on the plateau occurs for a limited range of frequency. As shown below, the mechanisms responsible for the narrow width of this frequency window are simple:

* At high frequency, waves cannot be supported by the topography of the Yermak Plateau even on the abrupt western and northern sides.

* At low frequency, waves can propagate all around the plateau, but currents associated with these waves are of small amplitudes.

a.   *Response of the plateau to higher frequency forcing*

The model is solved with a 19.39-hour period forcing. Figure 4.4 displays the normalized average kinetic energy on the plateau. Near the tip, the maximum value of KE is 1.5 versus 8 for the K_1 forcing. This discrepancy is due to the fact that the incident wave cannot propagate further around the plateau than the western corner. This is revealed by a series of snapshots of the surface elevation (see Appendix E) and confirmed by the kinetic energy amplification cell in the middle of the western side (with a maximum value of 3).

When the model is solved for a 13.5 hour period forcing no kinetic energy is apparent on the plateau.

77
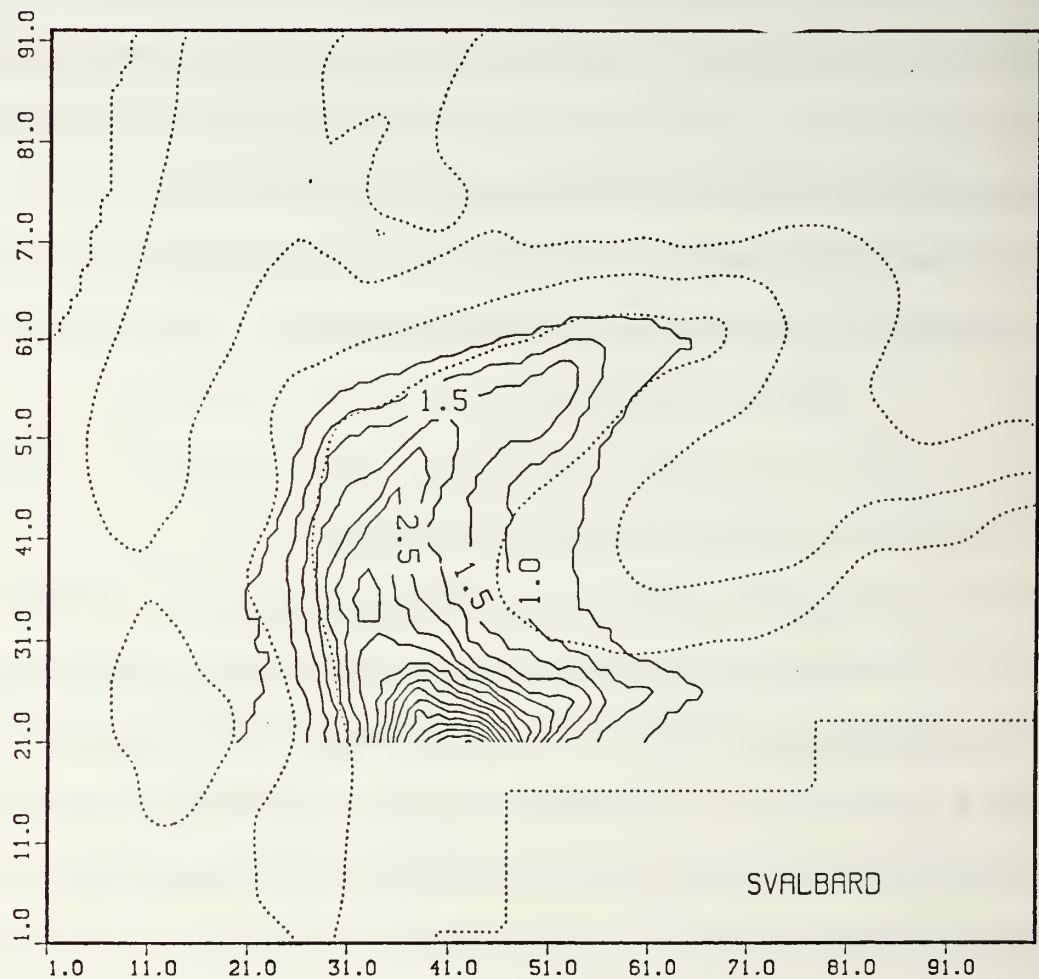
Figure 4.4 Normalized average kinetic energy for a 19.39-hour period forcing.

b. Response of the plateau to lower frequency forcing

The model is first solved with a forcing at the O_1 frequency. The CTW trapped by the plateau propagates further downshelf in the eastern part than does the K_1 wave (see Appendix E). However, the distribution of kinetic energy on the plateau is quite similar to the K_1 case (not shown), with two cells of high KE with magnitudes that are even greater. This proves the dominant scattering effect near the tip is associated with the curvature of the topography rather than the reflection caused by the flattening of the shelf.

For lower frequencies the friction coefficient has to be increased by a factor of 2 in order to maintain numerical stability in the model. Another solution would be to increase the spatial resolution, but computer limitations prevented this approach.

The model is solved with a 34.9 hour-period forcing. The ratio of friction over acceleration ($r/\omega h$) is 0.5 at the shallowest point of the plateau. Figure 4.5 displays the normalized average kinetic energy. The two strong current cells are present, and their maximum magnitudes (2.5 for the western cell and 5 for the tip cell) are comparable to the one found for a K_1 forcing with the same bottom friction.

Snapshots of the current vector and surface elevation fields every tenth of a period over half a period are displayed in Appendix E. They reveal the paths followed by the wave energy on the plateau. These pictures show that the trapped wave actually propagates completely around the plateau, as expected from the analytic study of the dispersion curve (see Analytic Model). Scattering occurs at the western side and at the tip, creating the high-KE cells with very significant across-shelf currents in the later case.

When the forcing period is increased to 49 hours, the ratio of friction over acceleration ($r/\omega h$) is 0.74 at the shallowest point on the plateau. The same remarks as above apply to the propagation of the trapped wave. However, the currents associated

79
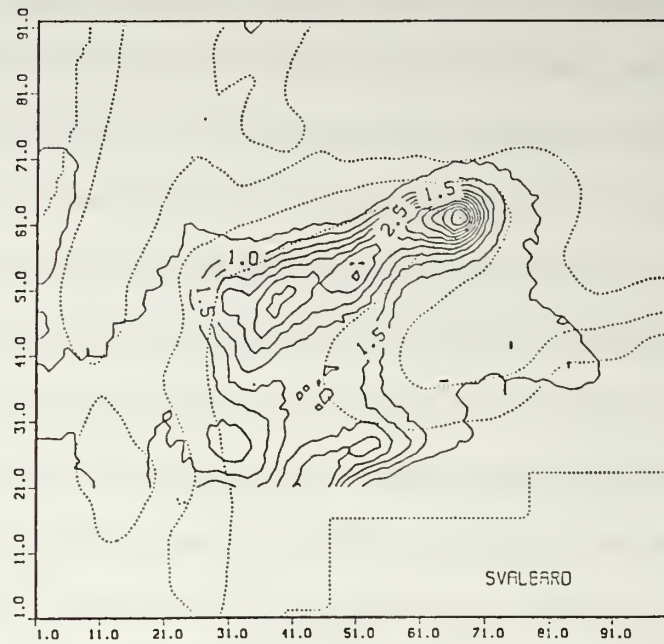
Figure 4.5 Normalized average kinetic energy for 34.9-hour period forcing.
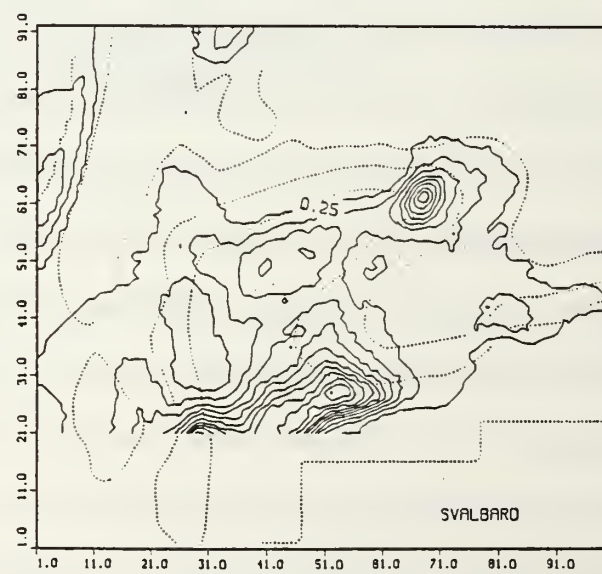
Figure 4.6 Normalized average kinetic energy for a 49-hour period forcing.

80

with the wave are very weak, and the kinetic energy plot (Figure 4.6) shows no current amplification on the plateau.

D. CONCLUSIONS FROM THE NUMERICAL INVESTIGATION

The numerical model shows that the Yermak Plateau response to an incident wave depends on the frequency of the forcing. Currents are significantly enhanced for forcing waves having periods within a window approximately extending from 20 to 35 hours.

The necessary conditions for current enhancement are:

* A CTW must be supported by the Yermak Plateau at the frequency of the forcing. This condition eliminates high frequency forcing.

* The current associated with the CTW must be large. This condition filters out low frequency waves.

When these conditions are satisfied the response of the Yermak Plateau can be described as follows:

* The overall feature is significant currents on the plateau that decrease very rapidly off-shelf.

* On a smaller scale (order of 80 km), the numerical model indicates that the kinetic energy is not distributed homogeneously over the plateau. In agreement with the observations, the model results show that the tip of the plateau is the region of highest kinetic energy. This feature is now explained numerically for the first time.

* However, the numerical model fails to indicate clearly that the strongest currents are to be found on the slope west of the tip.

V CONCLUSIONS AND RECOMMENDATIONS

A. CONCLUSIONS

Based on a few current-meter observations, Hunkins found anomalous diurnal currents on the Yermak Plateau. His radially symmetric analytic model predicted a uniform enhancement of the diurnal currents on the plateau.

In the present study, the analysis of thirty drifter tracks by statistical methods yields a complete and valid description of the diurnal currents on the plateau. This description reveals that the enhancement is not uniform over the plateau and the strongest currents are generated locally and limited to small regions.

First, a simple analytic model was used to show that the variation in the steepness of the slopes of the plateau could be responsible for significant spatial variations in the current field.

Next, a numerical model was used to show that the variation in the curvature of the plateau also plays an important role. Furthermore, the numerical model showed that the Yermak Plateau acts like a filter, enhancing motions with periods ranging from approximately 20 to 35 hours:

* waves with period shorter than 20 hours cannot propagate around the plateau.

* waves with period longer than 35 hours can propagate around the plateau, but the associated currents are small.

* within the period window, currents are enhanced by the plateau. This enhancement is not uniform and depends greatly on the changes in the topography.

The diurnal, but not the semi-diurnal, tide is within this window.

B.   RECOMMENDATIONS

Recommendations concern three aspects: enhancement of the data, improvement of the model and future studies.

1.   Enhancement of the data

ARCTEMIZ 86 and 87 drifting buoys provide a good spatial coverage of the Yermak Plateau, but the temporal coverage is not adequate. FRAM III and IV ice stations (Hunkins, 1986) provide good time series in limited areas. Ideal observations would have both. Simultaneous current-meter observations at different locations are required during a period of time long enough to resolve the two diurnal constituents, K_1 and O_1. A minimum of three locations are necessary: one on the western side of the plateau to observe the incident wave, a second one in the vicinity of the northeastern tip to observe the scattered waves, and a third one off the northern coast of Svalbard to detect the wave trapped by this coast. A fourth location inside Fram Strait off the western coast of Svalbard could give additional information on the tidal forcing.

For the deep water stations, locations close to the 1000 m isobath seem consistent with the structure of the trapped wave revealed by the numerical model. Since the diurnal currents are mainly barotropic, current-meters set in the upper 100 meters of the ocean would be adequate at each location.

Due to ice coverage current meter moorings can be lost easily. Summer time provides a no-ice condition for the southern stations. The northernmost station located near the tip of the plateau is ice covered all year. Two possibilities exist for sensing at this location:

- An ice camp with a current meter suspended below an ice flow, provided that the mean advection of ice on the northern side of the Yermak Plateau is small.

- A moored current meter transmitting its data to an onshore station located 250 km in the south, on the northern coast of Svalbard via a fiber optic link.

2.   Improvement of the model

A predictive model of the current structure on the Yermak Plateau would include:

* High resolution bathymetry, especially near the tip of the plateau. The small scale bottom features in this area probably play an important role in the scattering of CTW. A finite element model may be appropriate to best resolve these features.

* Accurate definition of the forcing using the results provided by a regional tidal model (Schwiderski, 1986; Gjevik and Straum, 1989).

* Atmospheric forcing.

* Increased spatial resolution.

An ice model would be necessary to study the ice response to the tidal forcing and the seasonal variability of the ice.

3.   Future studies

The enhanced rotating diurnal currents on the Yermak Plateau may play an important role in the grinding of the ice floes and act in the breaking/freezing of ice in this region. Several phenomena may be related to this effect:

* Strong turbulent fluxes associated with the diurnal currents have been found during CEAREX 89 (Padman and Dillon, 1990).

* Remotely sensed ice morphology/concentration should show the different morphology due the grinding effect. A study of ice concentration in this region from microwave satellite sensor SSM/I is presently in progress (Wright, personal communication).

* Ambient noise should be enhanced in the region of grinding. Cousins (1991) analyzed ambient noise data east of the Yermak Plateau. He pointed out strong semi-diurnal variations in the level of the ambient noise that were correlated with inertial motion.

APPENDIX A: BUOY TRAJECTORIES FOR ARCTEMIZ 87

Trajectories of all the ARCTEMIZ 87 buoys. The tracks are marked beginning with the deployment date, the last date and at 60 days intervals. Expanded views of the trajectories for buoys which passed over the Yermak Plateau are presented in Appendix B.
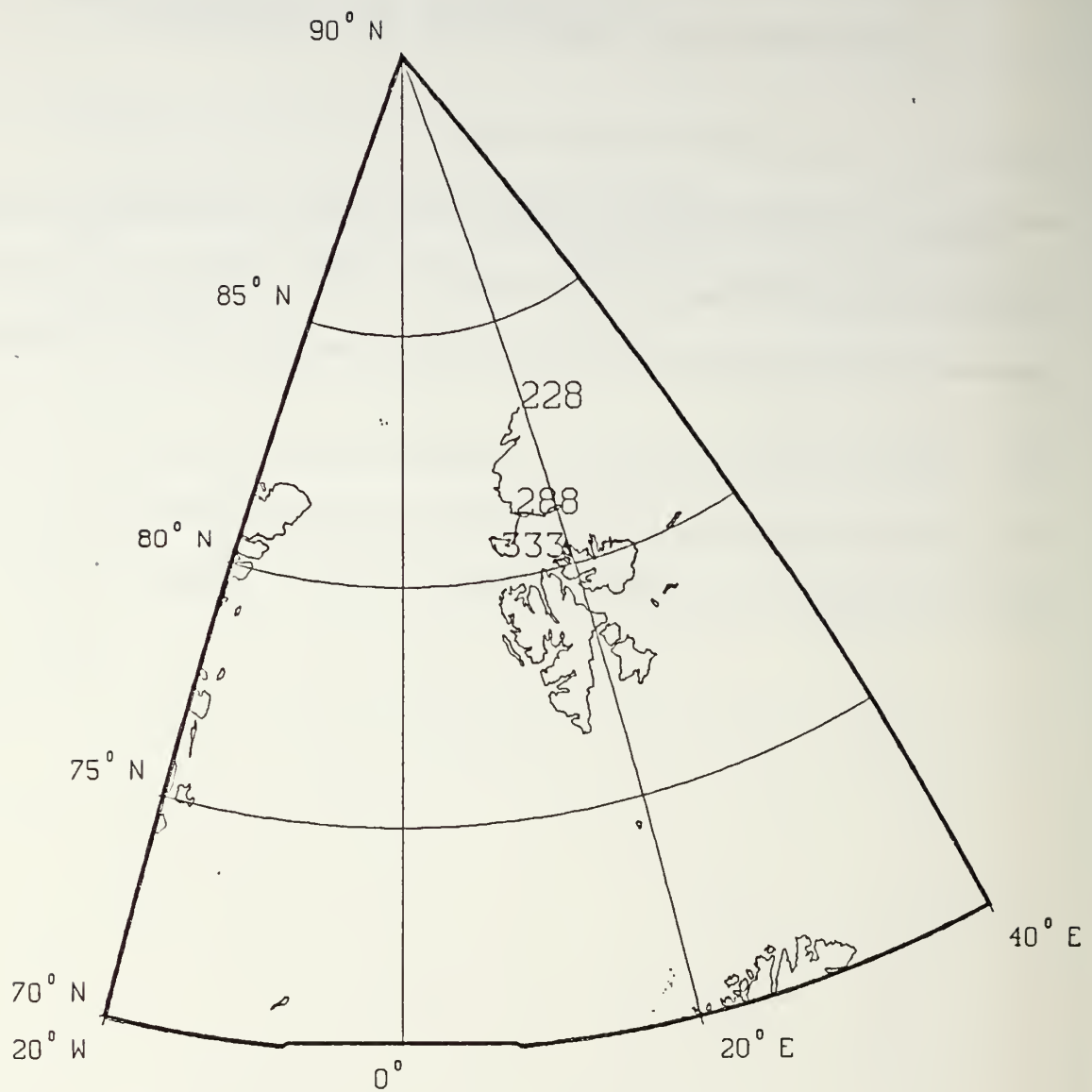
Figure A1. Trajectory of buoy 1479.
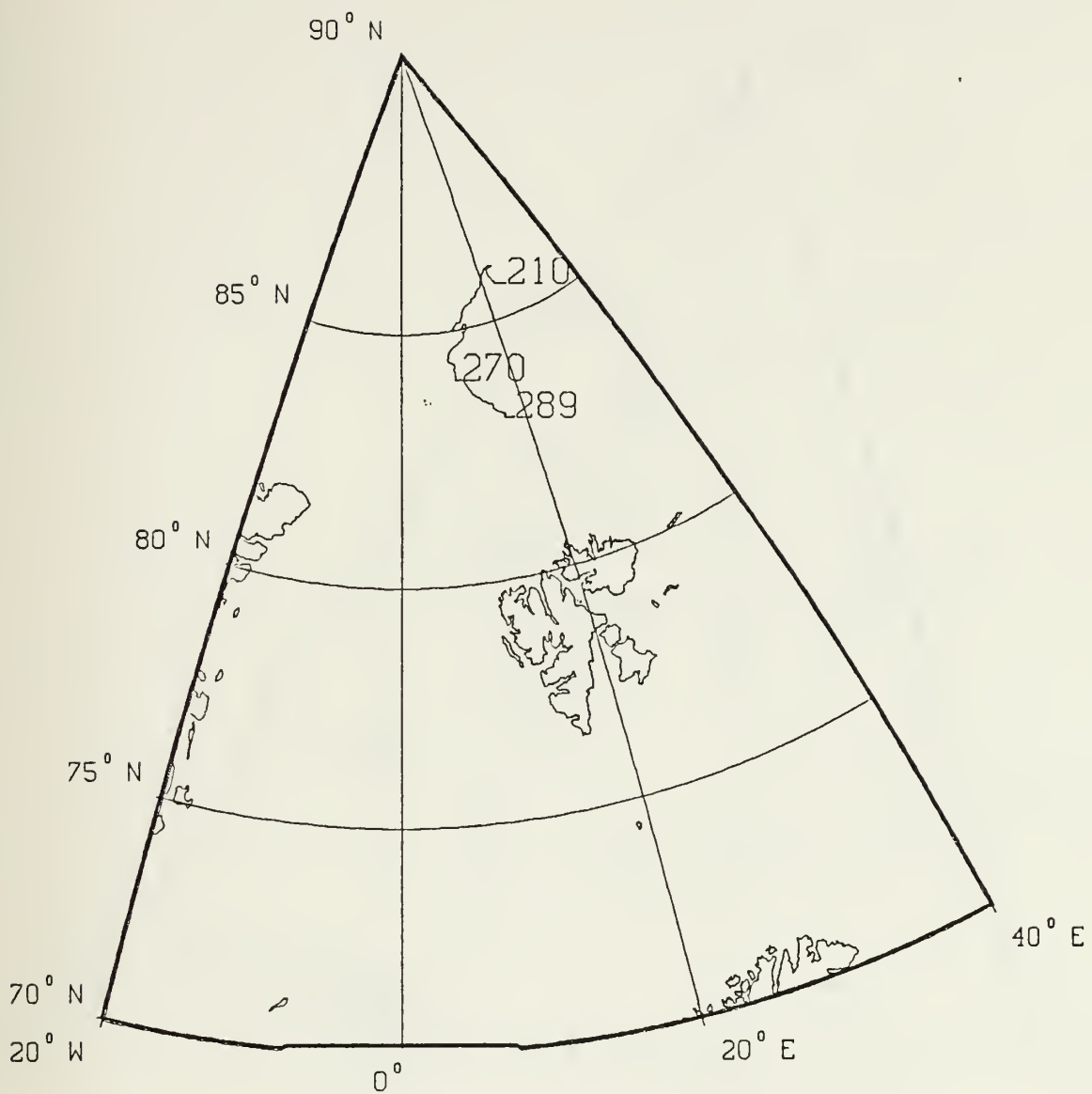
Figure A2. Trajectory of buoy 4992.

89
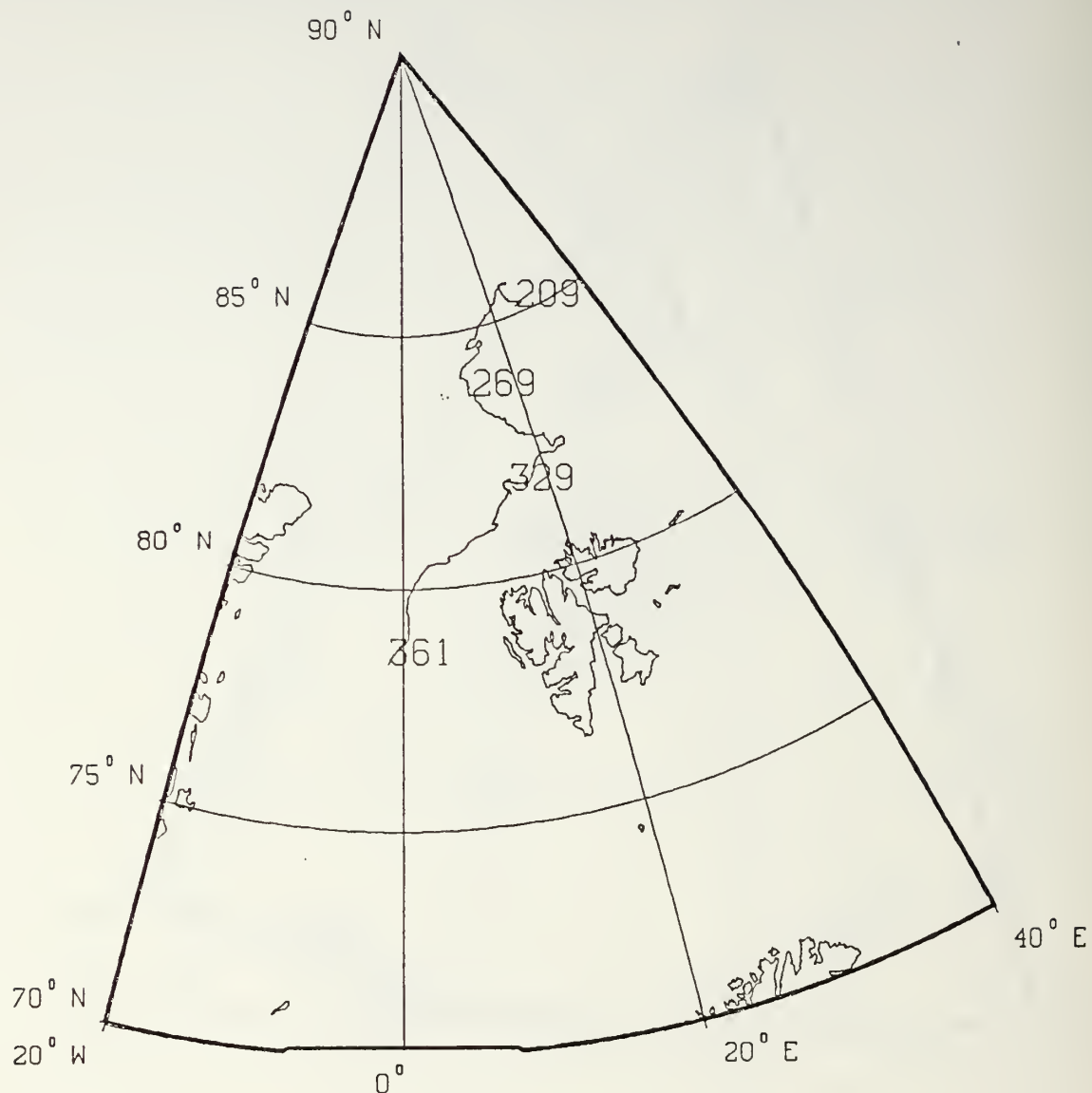
Figure A3. Trajectory of buoy 5077.
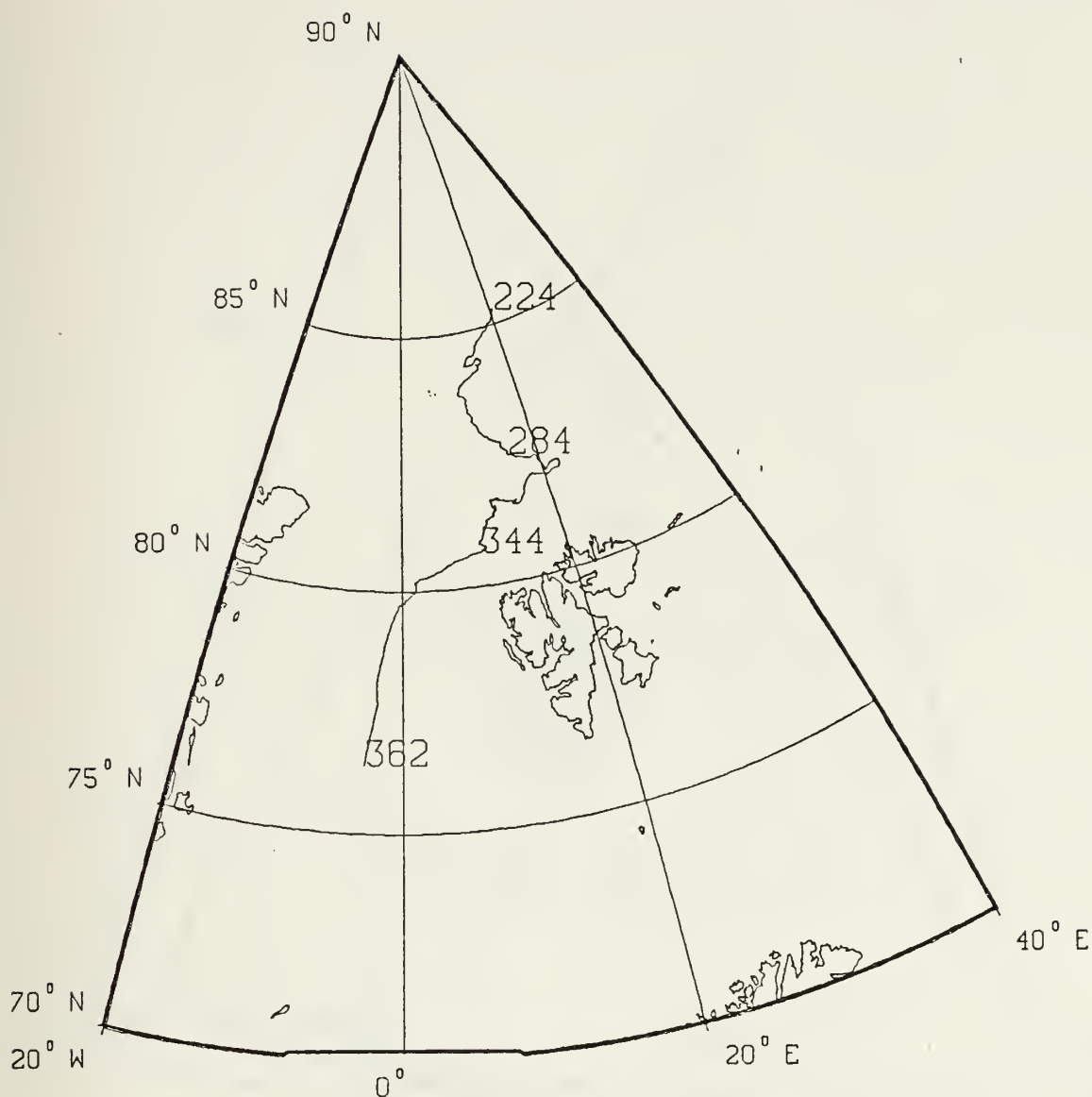
Figure A4. Trajectory of buoy 4994.
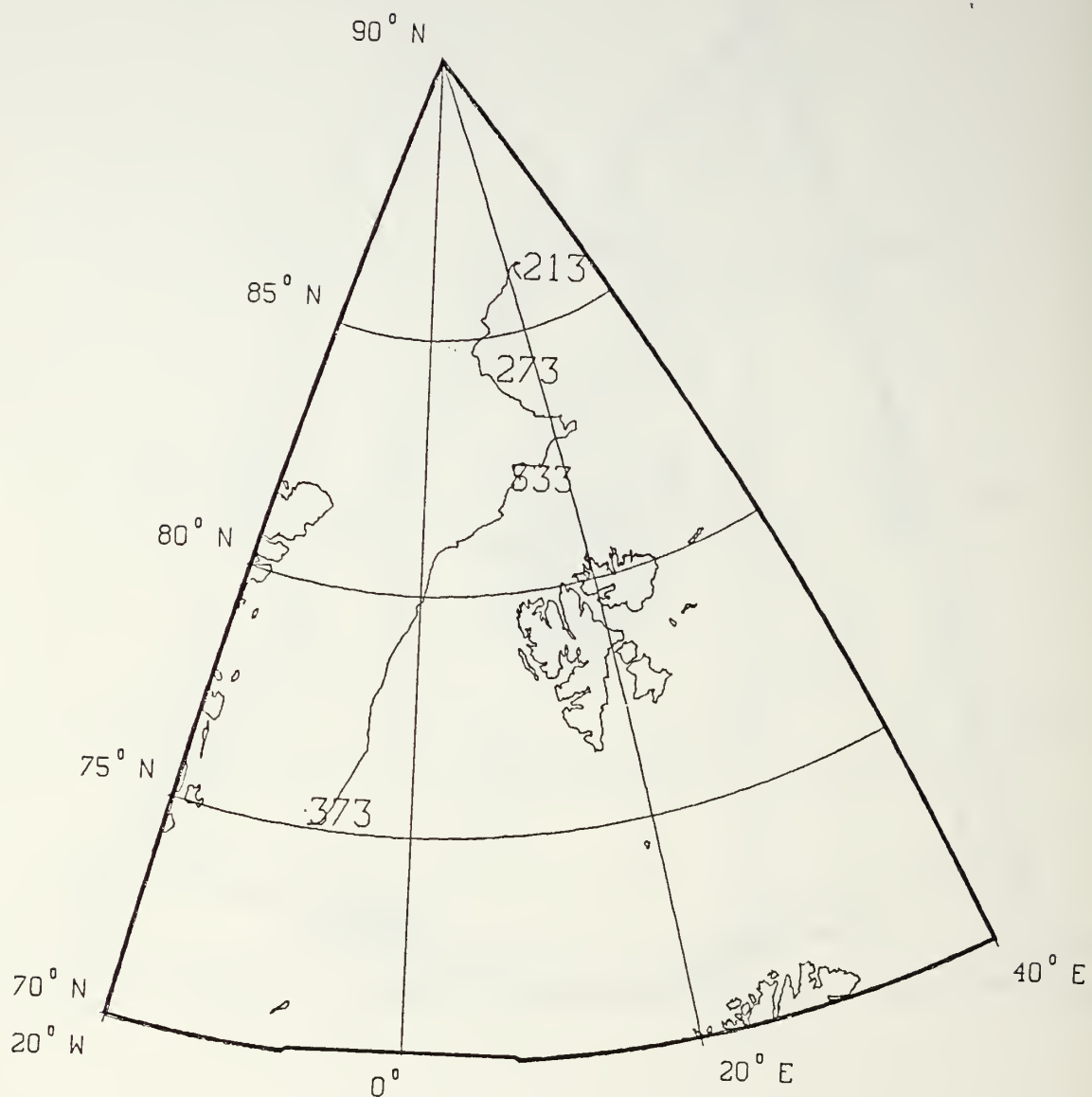
Figure A5. Trajectory of buoy 3491.
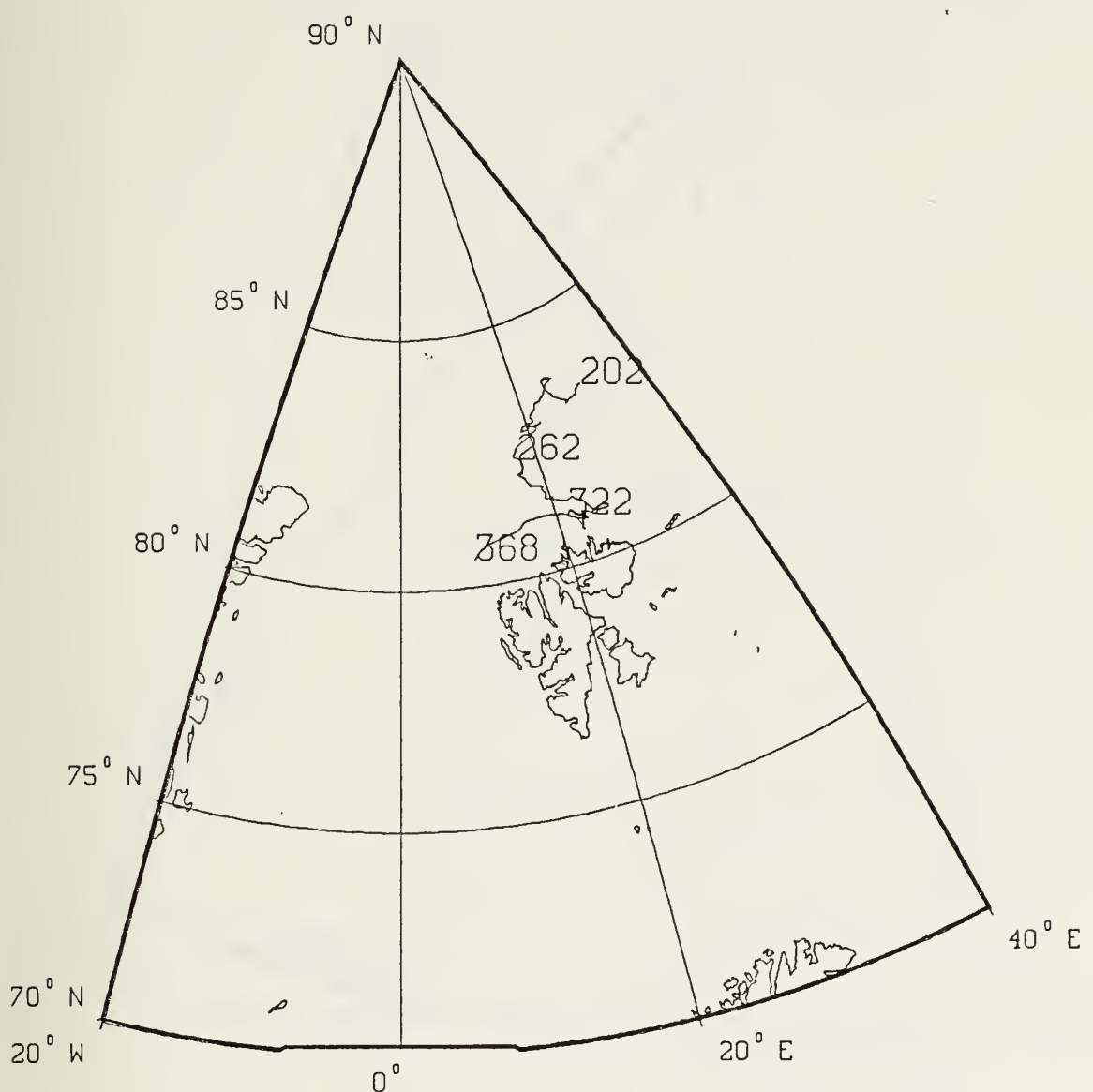
Figure A6. Trajectory of buoy 5094.
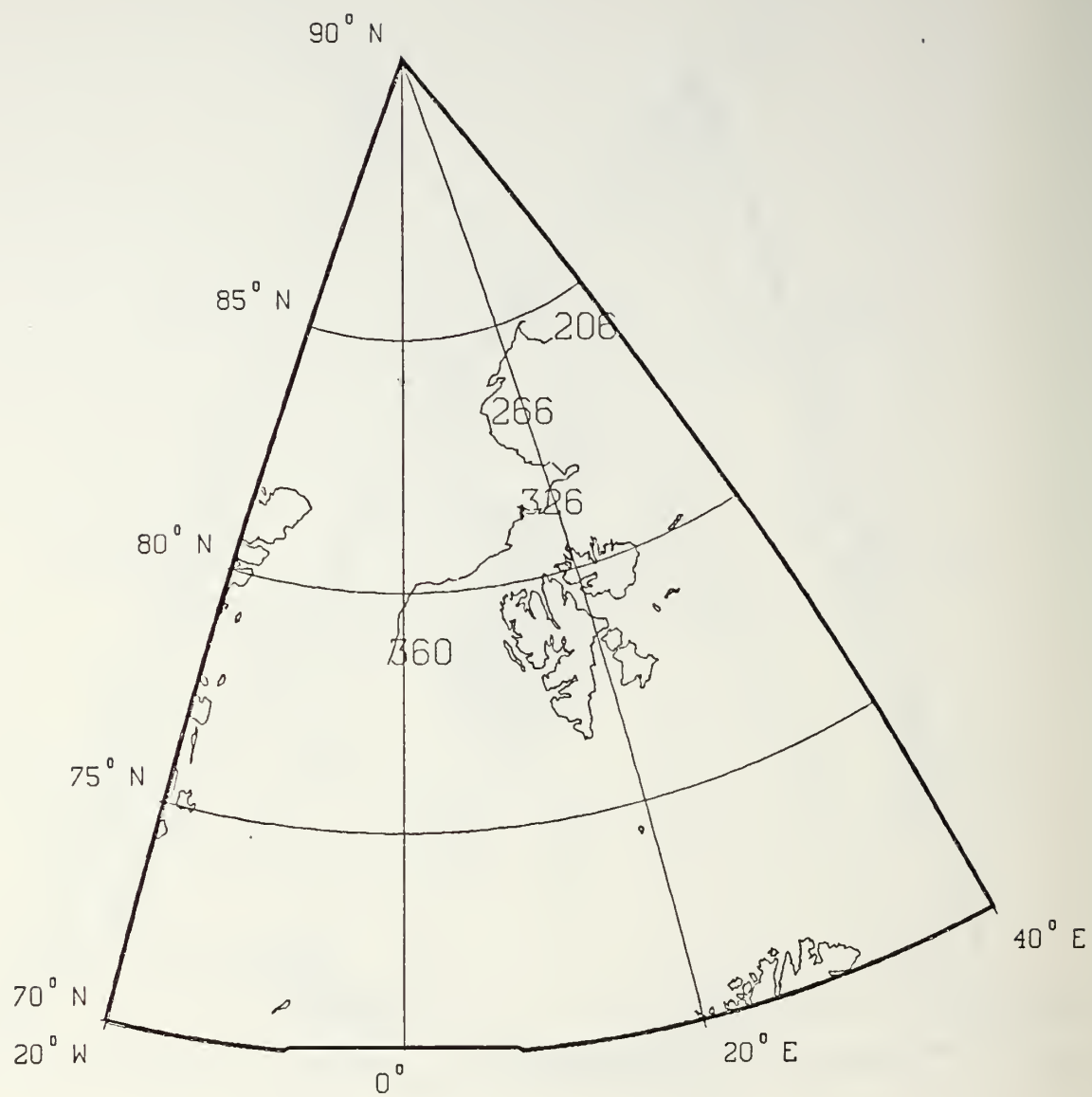
Figure A7. Trajectory of buoy 4996.
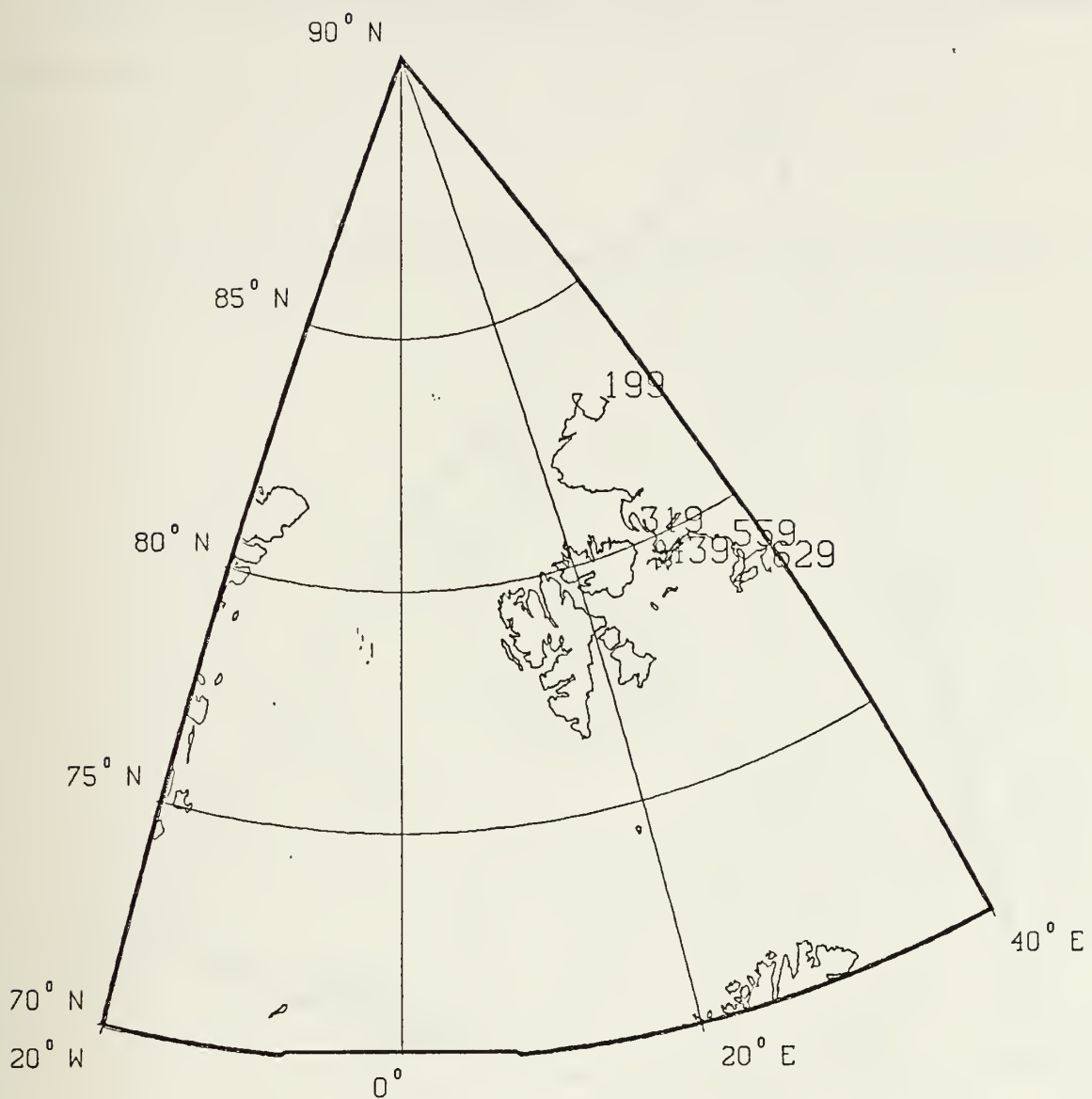
Figure A8. Trajectory of buoy 5079.
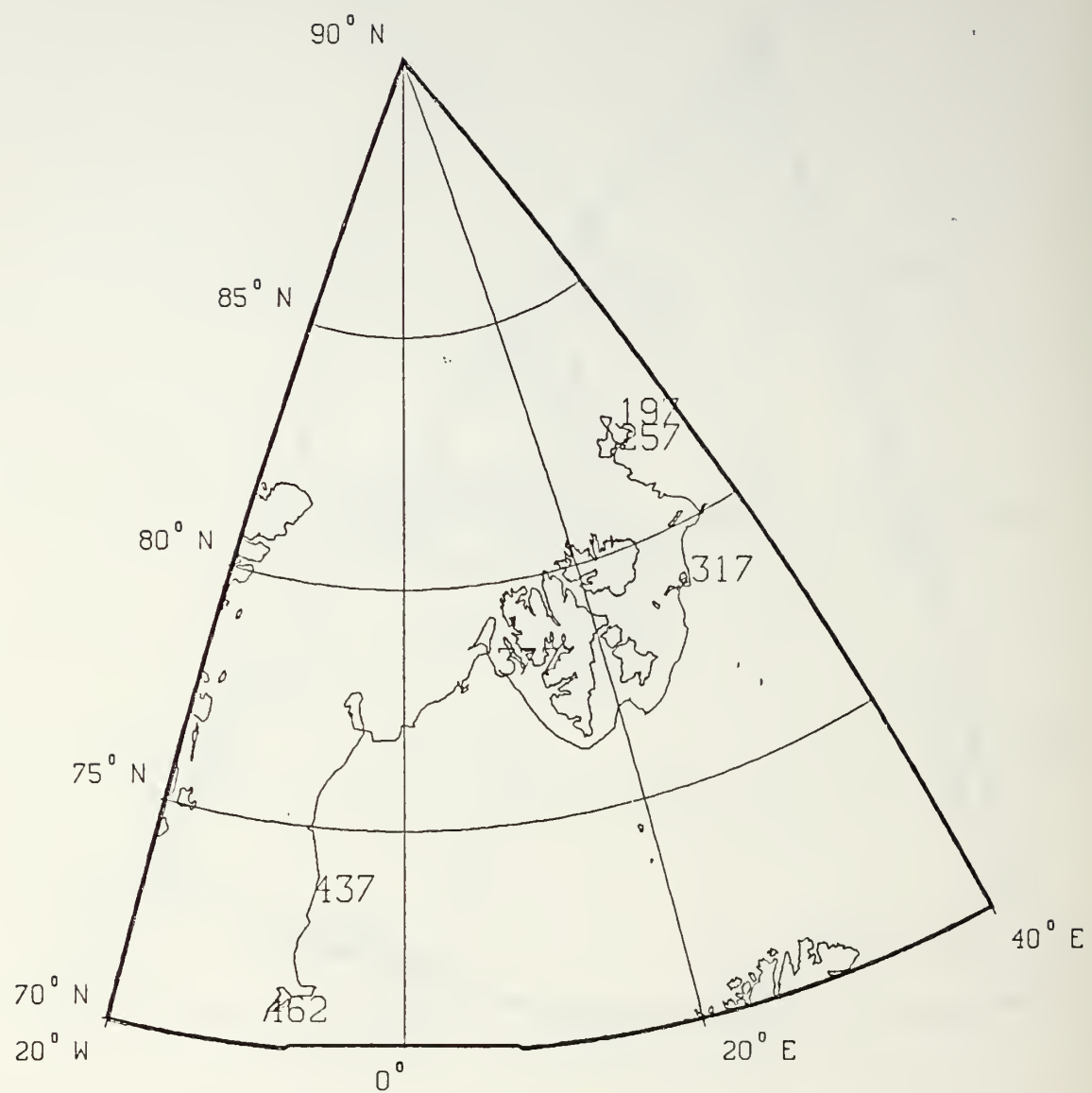
Figure A9. Trajectory of buoy 5095.

APPENDIX B: TRAJECTORIES OF BUOYS IN THE VICINITY OF THE YERMAK PLATEAU

Trajectories of the ARCTEMIZ 87 buoys that drifted over the Yermak Plateau.
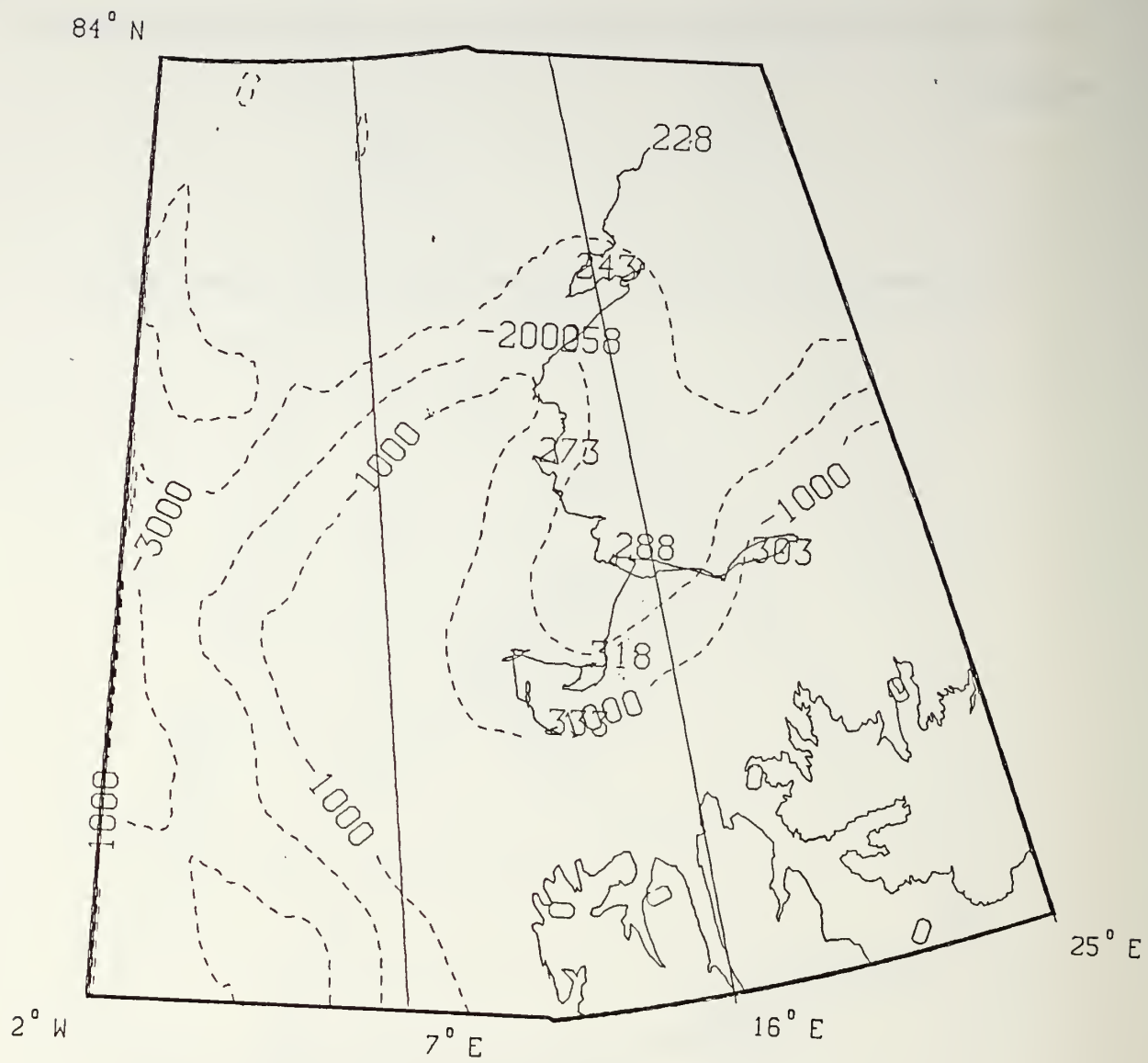
Figure B1. Trajectory of buoy 1479.
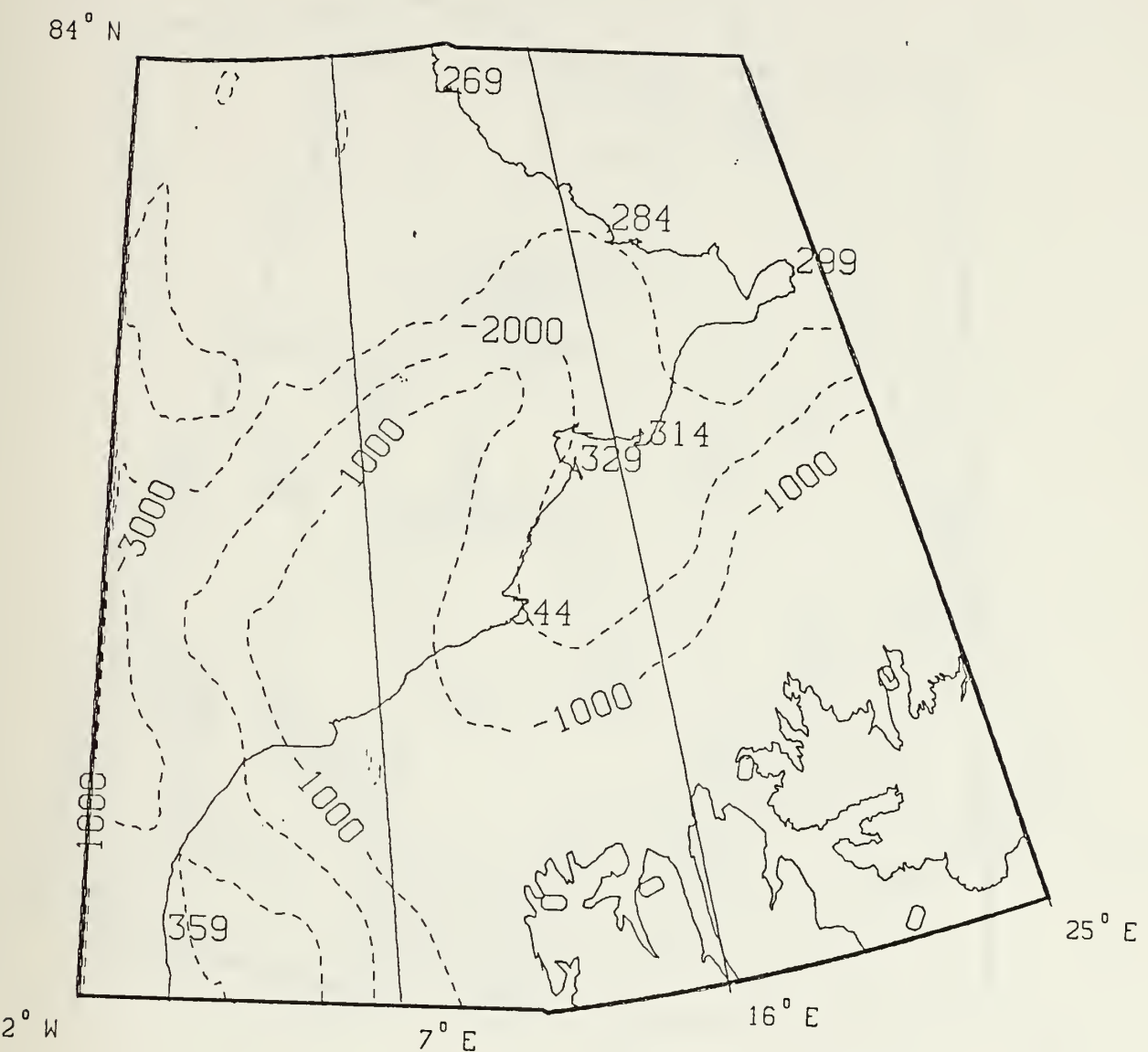
Figure B2. Trajectory of buoy 5077.
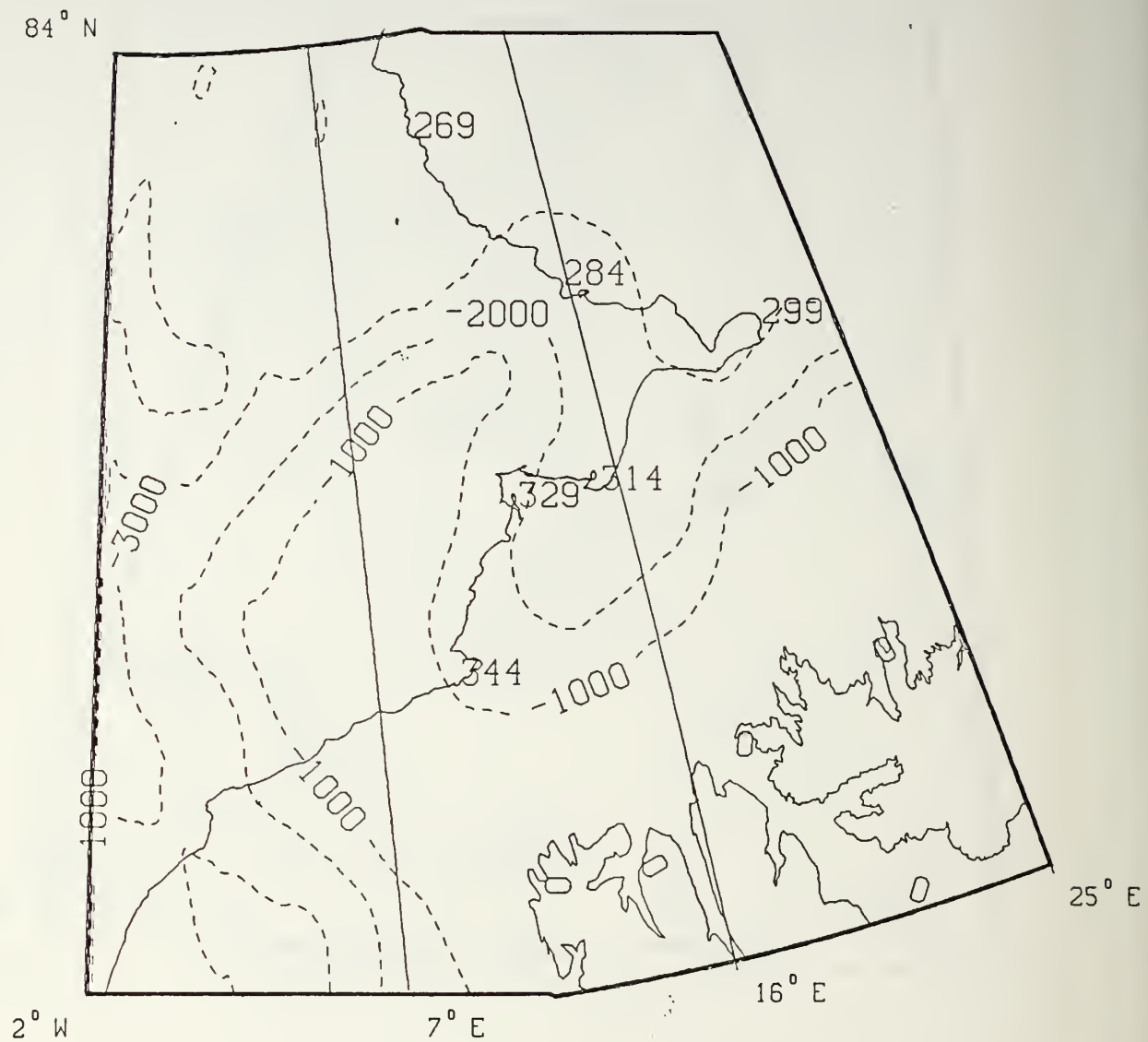
Figure B3. Trajectory of buoy 4994.
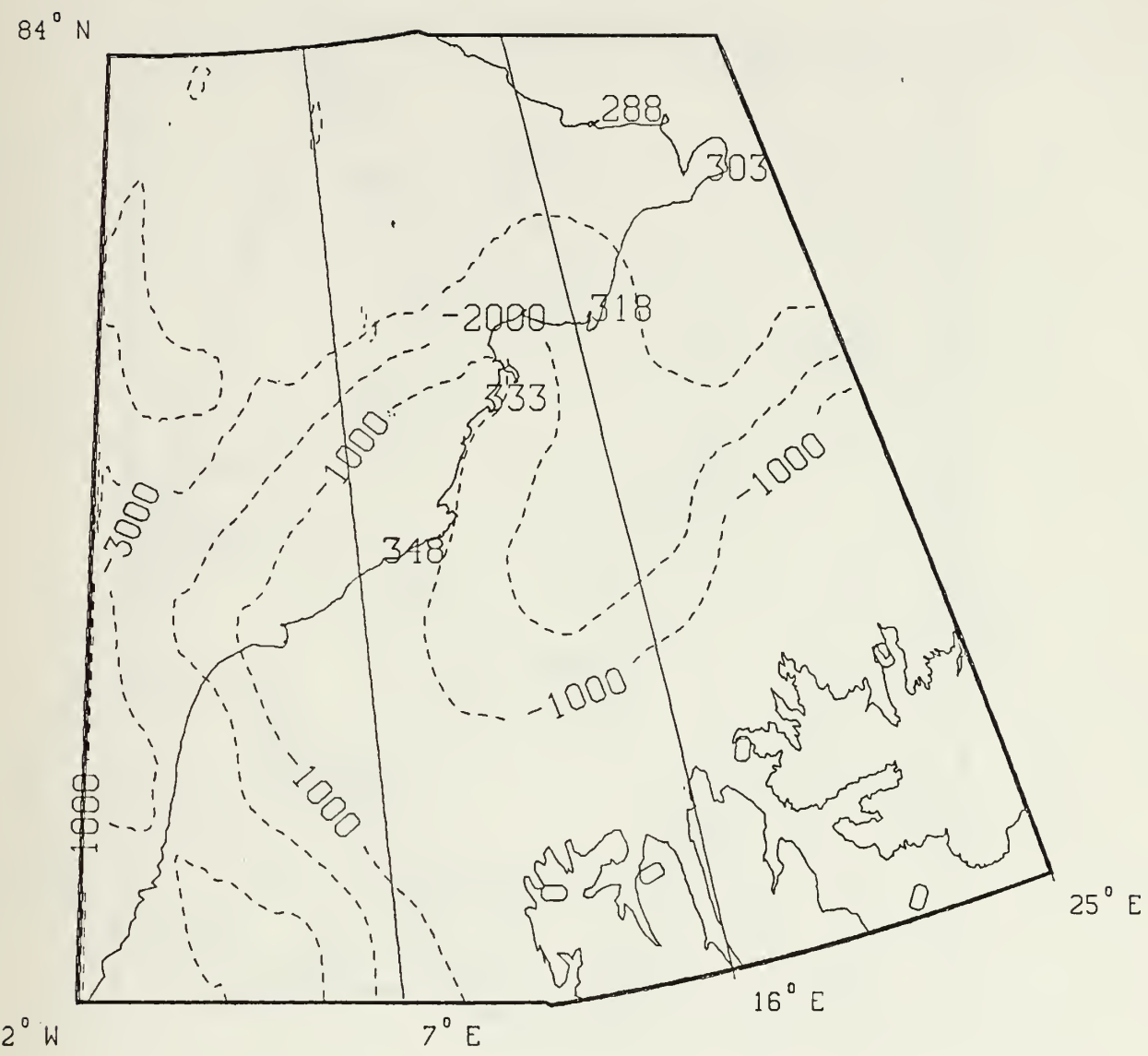
Figure B4. Trajectory of buoy 3491.
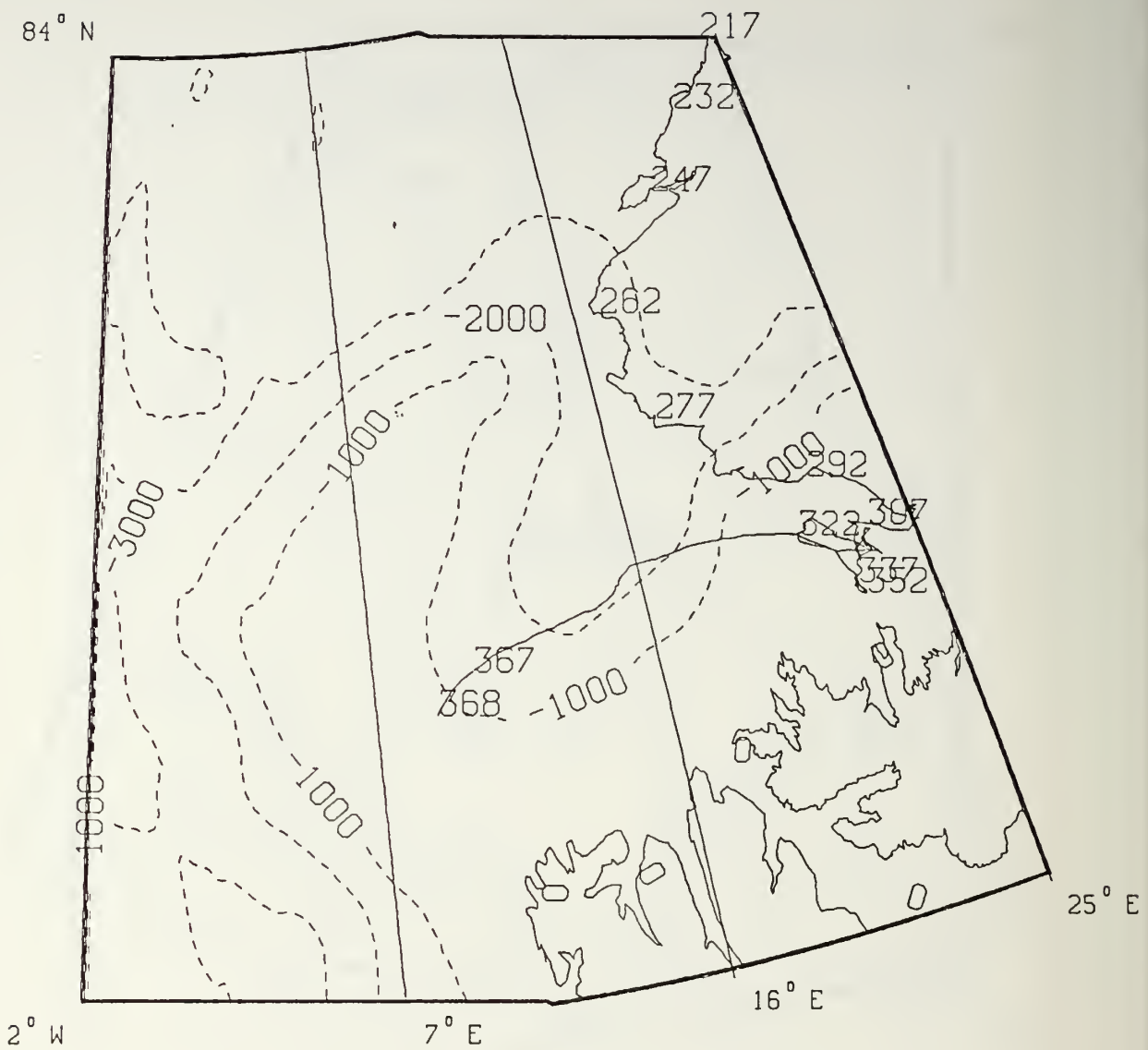
Figure B5. Trajectory of buoy 5094.
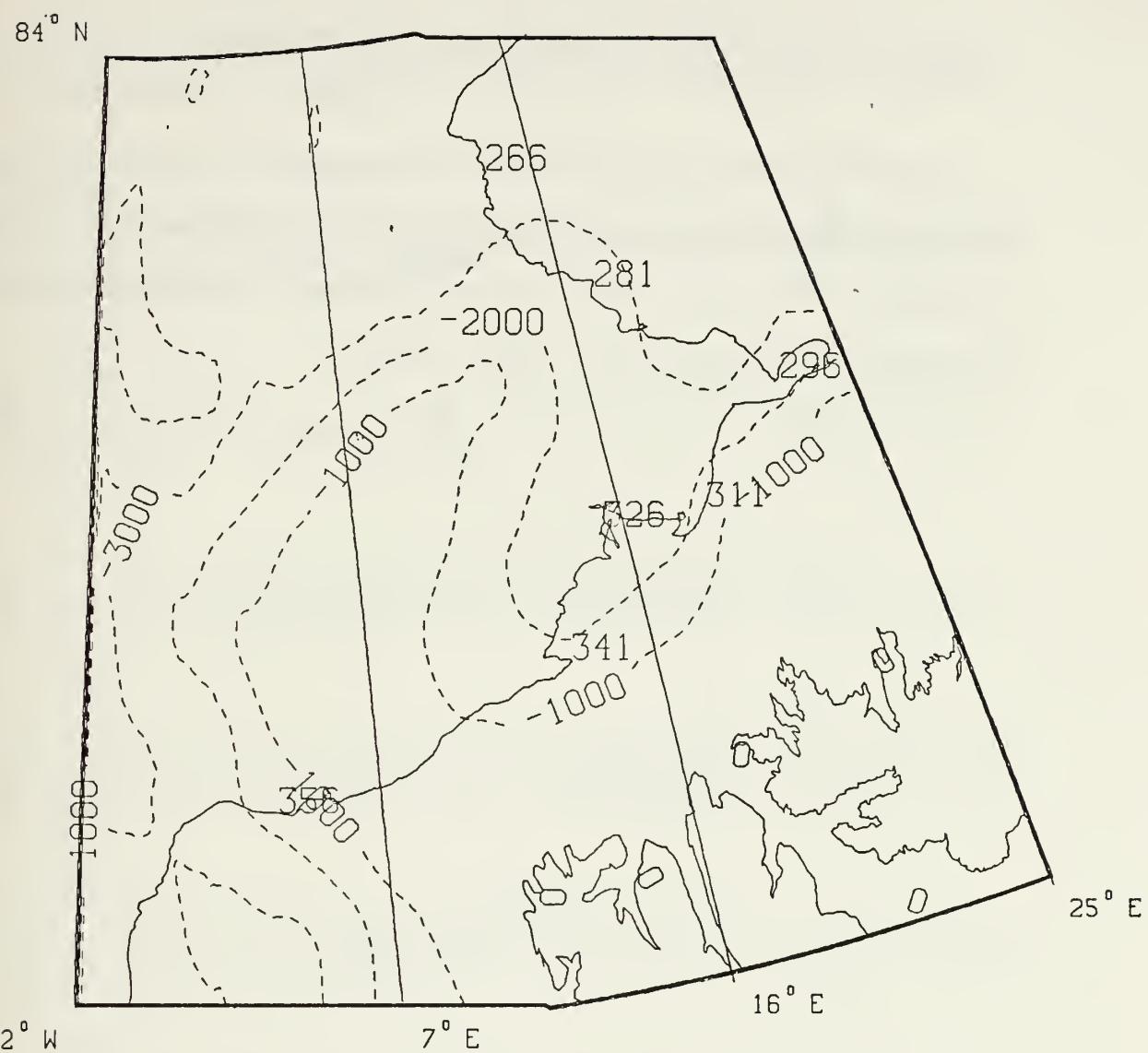
Figure B6. Trajectory of buoy 4996.

APPENDIX C: ARCTEMIZ 87 TIME SERIES

Time series reconstructed from complex demodulation for ARCTEMIZ 87 buoys. Demodulation was performed using the technique developed by McPhee (1986). The u and v components of the velocity are separated into semi-diurnal / diurnal clockwise (SCW / DCW) and counter-clockwise (SCCW / DCCW) signals.
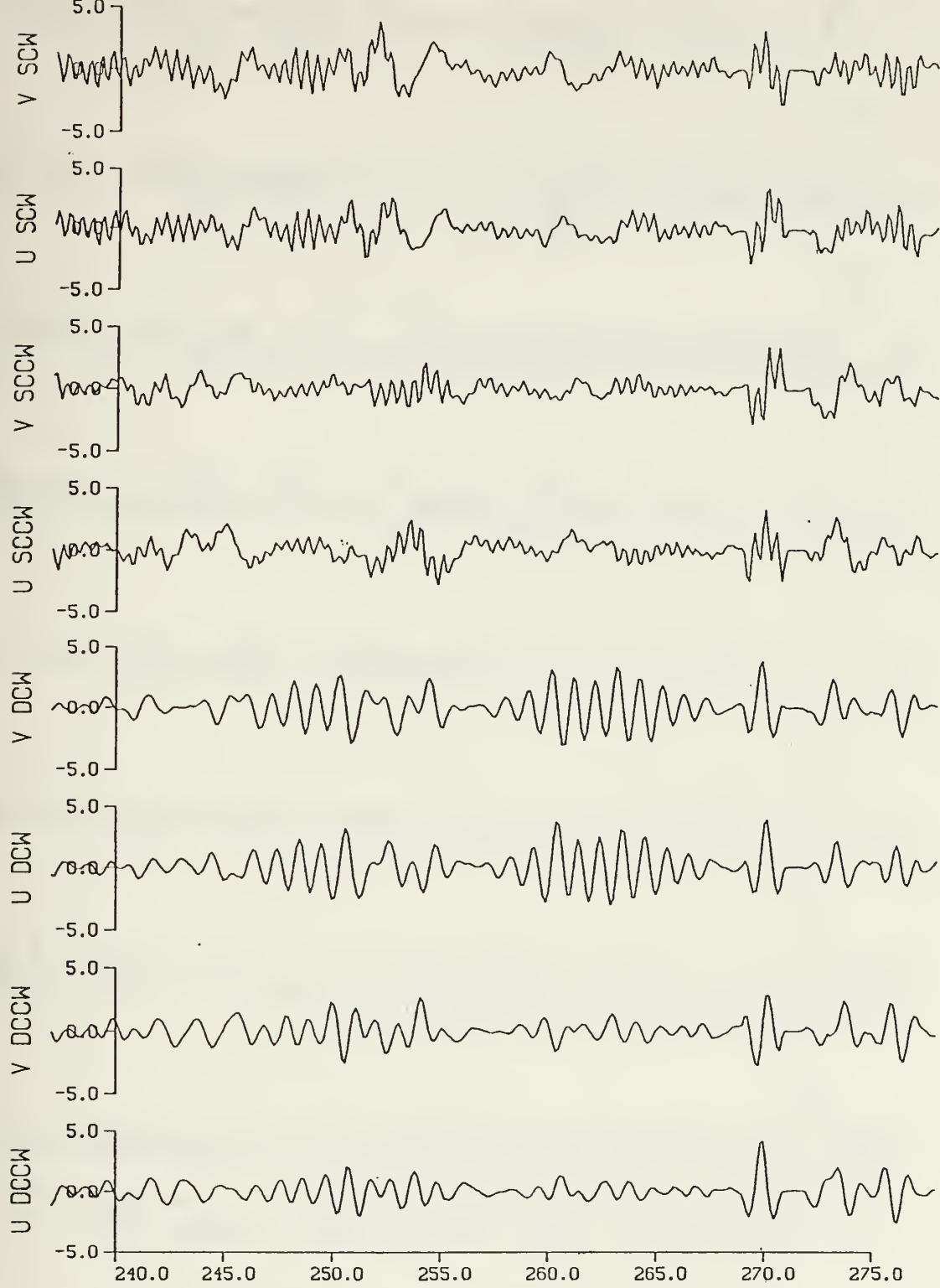
Figure C1. Buoy 1479.

105
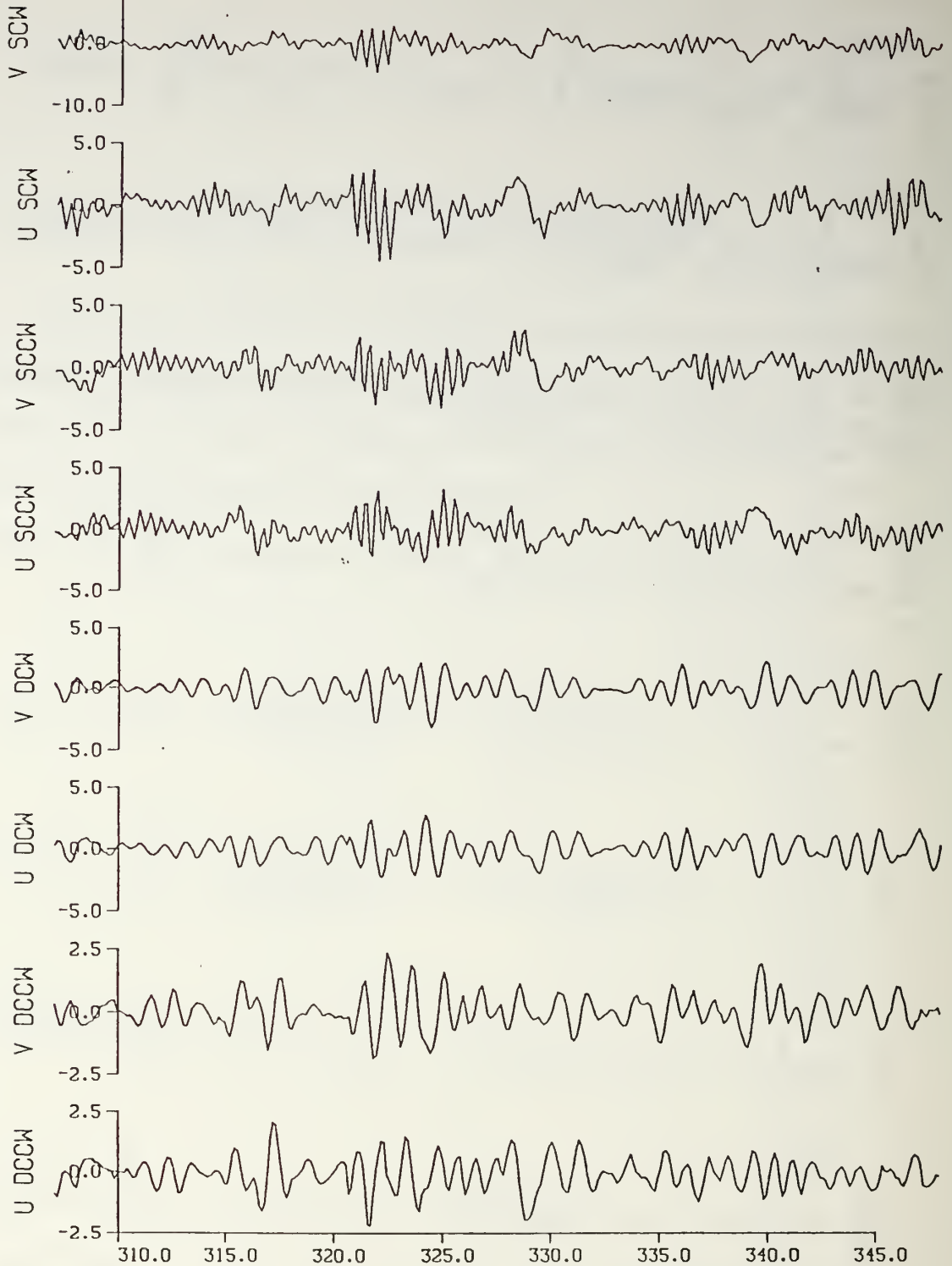
Figure C2. Buoy 5077.

106
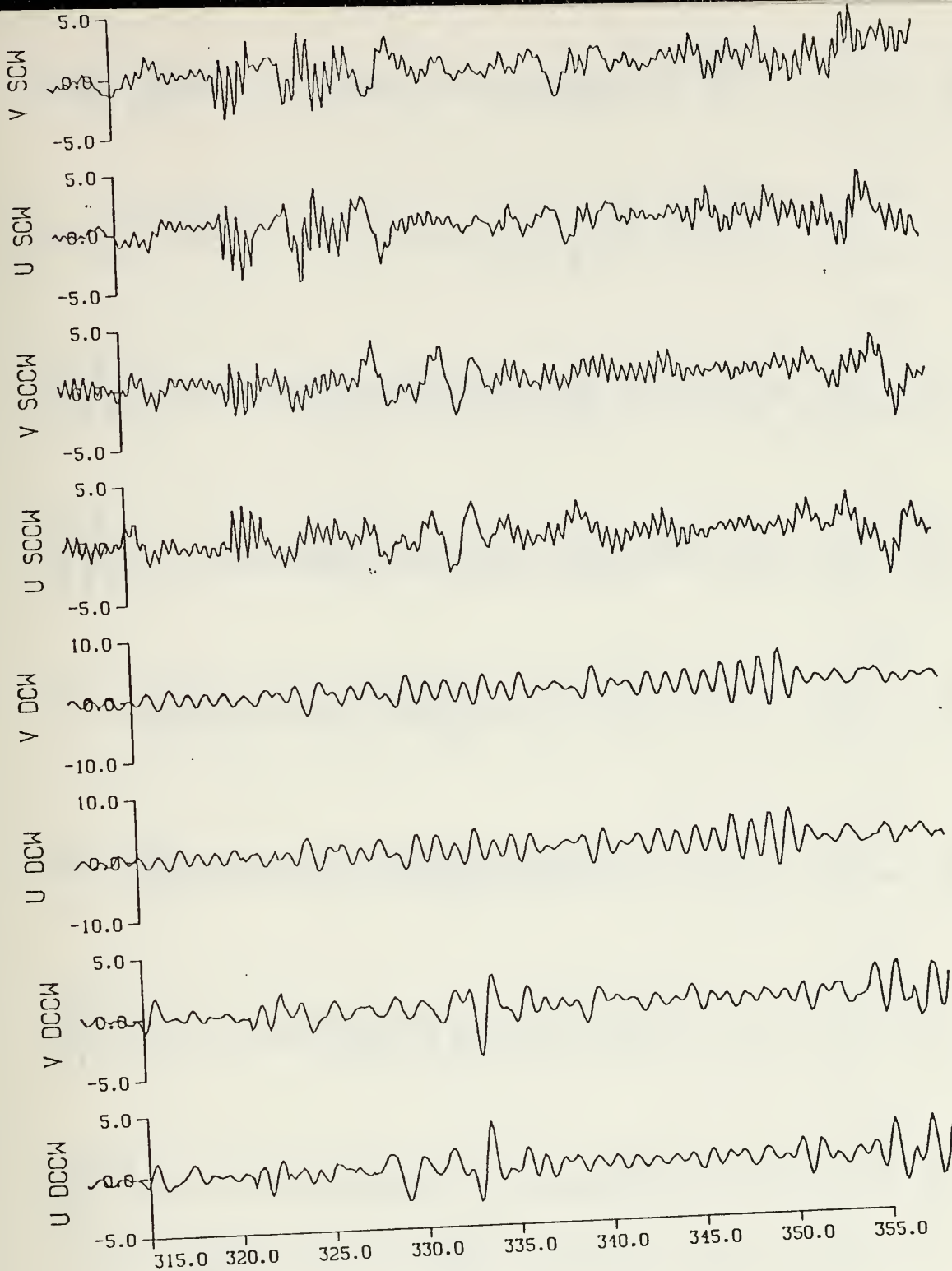
Figure C3. Buoy 4994.

107
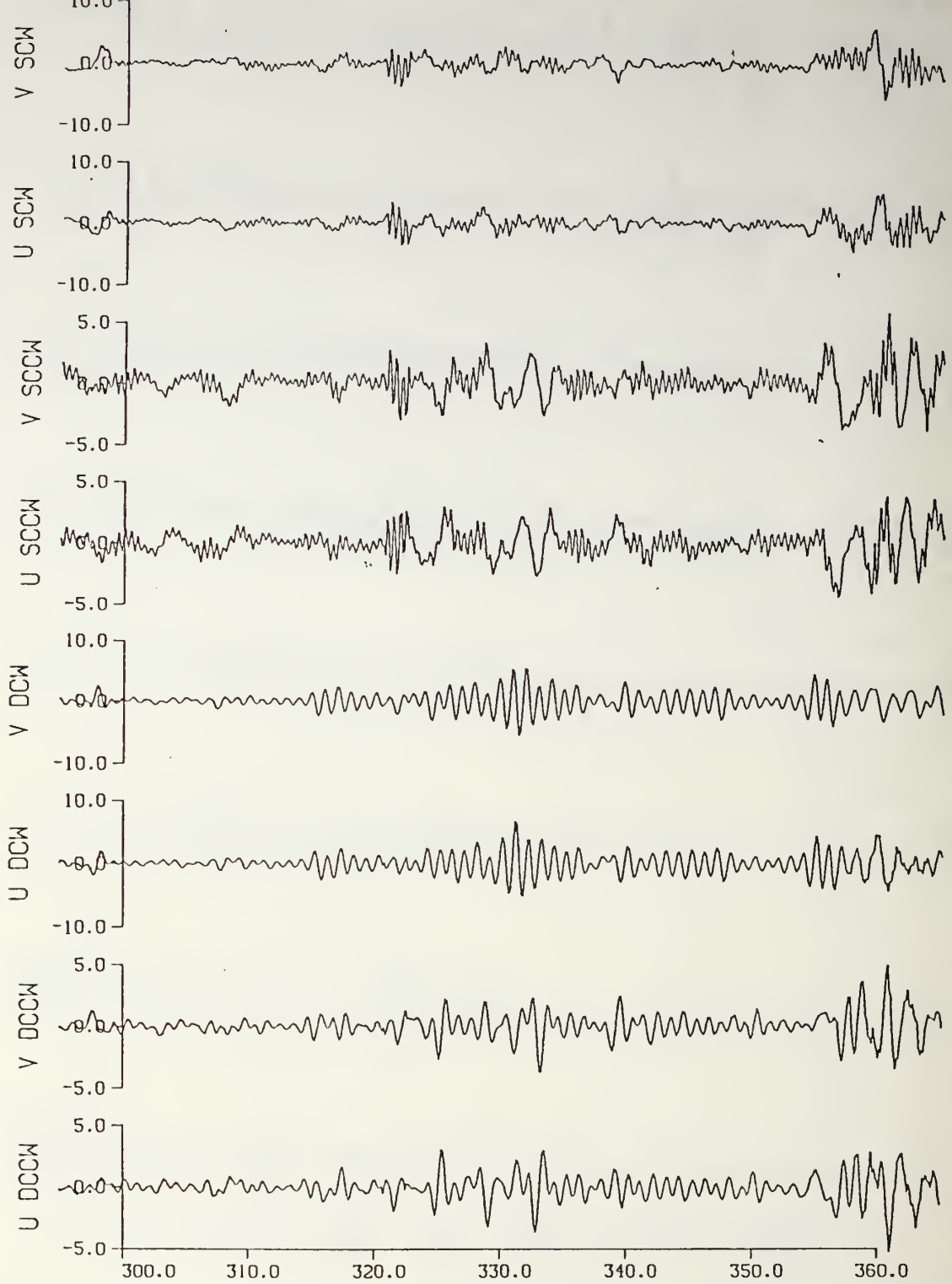
Figure C4. Buoy 3491.

108
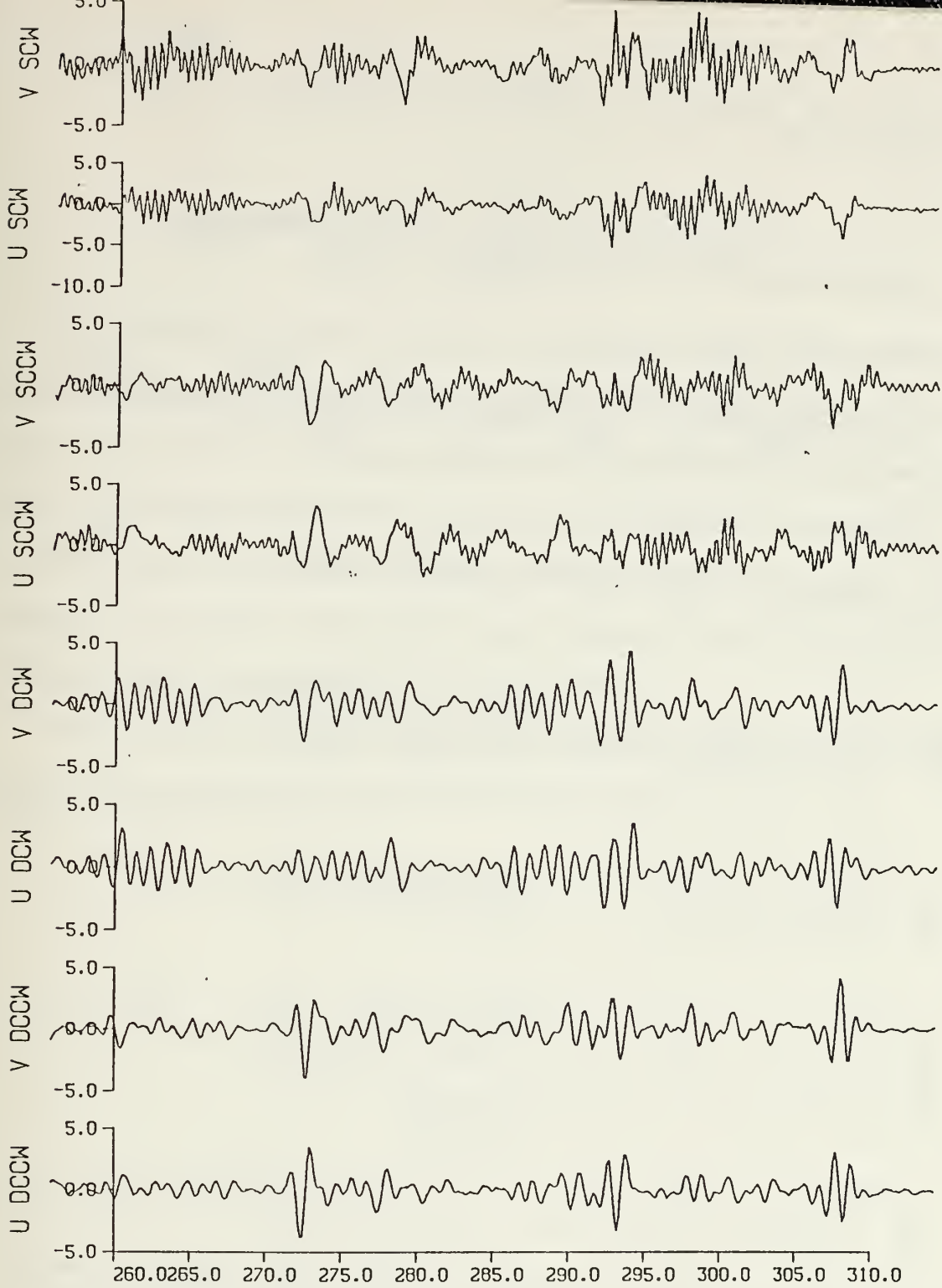
Figure C5. Buoy 5094.

109
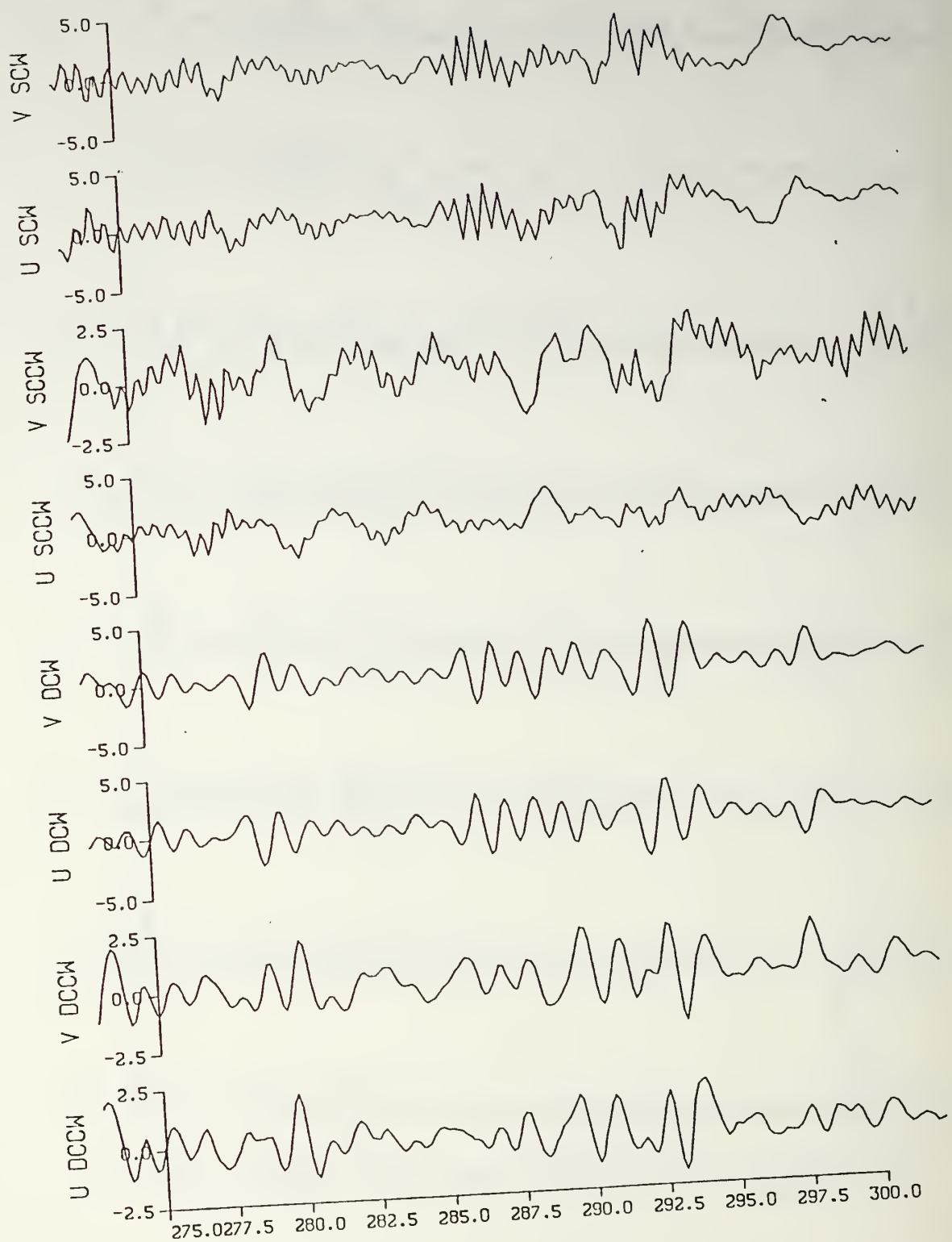
Figure C6. Buoy 4996.

110

APPENDIX D: FORCING BOUNDARY CONDITION

The forcing boundary condition north of Fram Strait is computed analytically. The forcing wave structure is determined by the first mode of a CTW propagating along the western coast of Fram Strait. The actual shelf profile is approximated by an exponential profile. The boundary conditions are no flow normal to the coast and out of the shelf so that the forcing wave is contained in a channel having the width of the shelf. Without modifying the waveguide physics, these boundary conditions allow a simple analytic treatment in a frictional ocean (Wilkin and Chapman, 1989).

Starting with the linearized shallow water equations of motion, the continuity equation, and the assumption of a rigid lid at the ocean surface:

$$\frac{\partial u}{\partial t} - fv = -g\frac{\partial \eta}{\partial x} - \lambda u \tag{1}$$

$$\frac{\partial v}{\partial t} + fu = -g\frac{\partial \eta}{\partial y} - \lambda v \tag{2}$$

$$\frac{\partial uh}{\partial x} + \frac{\partial vh}{\partial y} = 0 \tag{3}$$

where a constant Rayleigh damping coefficient $\lambda = r/h_o$ is used.

The form of the continuity equation allows a stream function ϕ to be defined such that:

Using the definition of the stream function in equations of motion (1) and (2) leads to:

$$\frac{\partial \phi}{\partial x} = vh$$

$$\frac{\partial \phi}{\partial y} = -uh$$

$$e[\frac{\partial}{\partial x}(\frac{1}{h}\frac{\partial \phi}{\partial x}) + \frac{\partial}{\partial y}(\frac{1}{h}\frac{\partial \phi}{\partial y})] = \frac{\partial}{\partial x}(\frac{1}{h}\frac{\partial \phi}{\partial y}) - \frac{\partial}{\partial y}(\frac{1}{h}\frac{\partial \phi}{\partial x}) \qquad (4)$$

where:

$$e = \frac{\omega}{f} - i\frac{\lambda}{f}$$

ω being the frequency.

Solutions of (4) are assumed to be separable of the form:

$$\phi(x,y,t) = \psi(x)e^{i(\omega t - ly)}$$

Topography is of the form:

$$h(x) = h_L e^{2b(x-L)}$$

Equation (4) can then be rewritten:

$$\frac{d^2 \psi}{dx^2} - 2b\frac{d\psi}{dx} - (2ible^{-1} + l^2)\psi = 0 \qquad (5)$$

the boundary conditions $\phi = 0$ at $x = 0$, L yields solutions of the form:

$$\psi(x) = e^{bx}\sin(mx) \qquad (6)$$

where m = nΠ/L. Equations (5) and (6) lead to the dispersion equation:

$$b^2 + l^2 + m^2 + 2i\frac{bl}{\epsilon} = 0 \qquad (7)$$

Equation (7) gives the dispersion relations between the long wave (l_L) and the short wave (l_S) wavenumbers and the complex frequency ϵ:

$$l_L = -\frac{b}{\epsilon}i[1 - \sqrt{1 + \epsilon^2(1 + \frac{m^2}{b^2})}] \qquad (8)$$

$$l_S = -\frac{b}{\epsilon}i[1 + \sqrt{1 + \epsilon^2(1 + \frac{m^2}{b^2})}] \qquad (9)$$

These wavenumbers are complex. Their real part corresponds to the traditional propagating wavenumber, and their imaginary part is the exponential decay of the wave. The inverse of the imaginary part of a wavenumber is the e-folding decay length scale.

APPENDIX E: "MOVIE" AND NUMERICAL RESULTS

Numerical model results for different periods of the forcing. Current vectors and surface elevation are displayed every tenth of a period during half of a period.
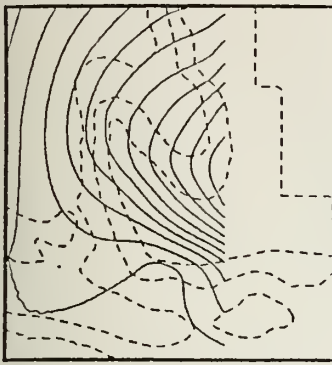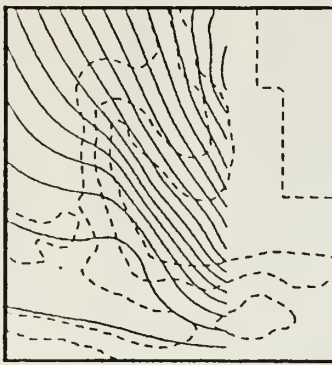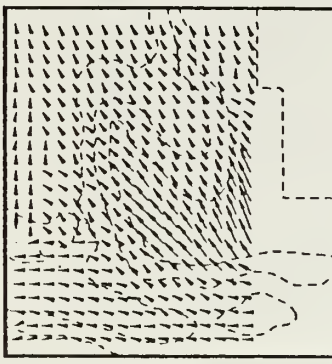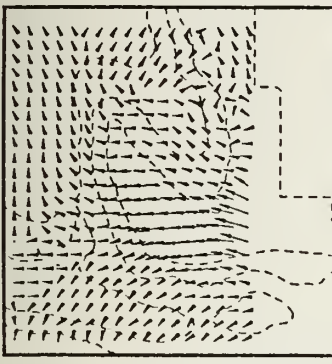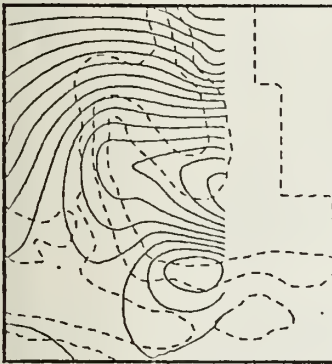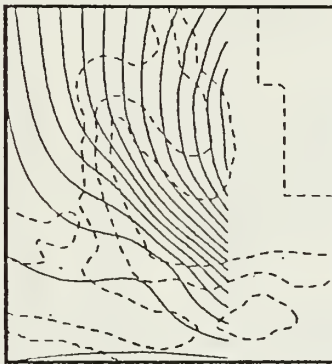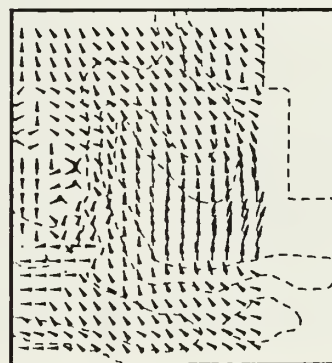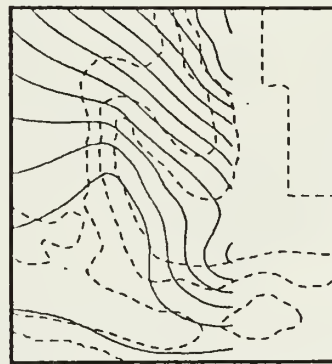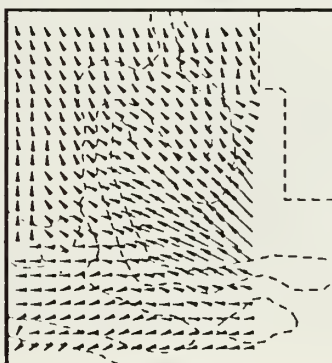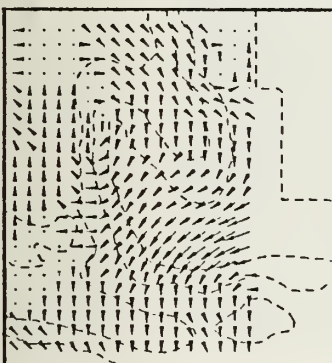
Figure E1. Forcing period of 19.4 hours.

115
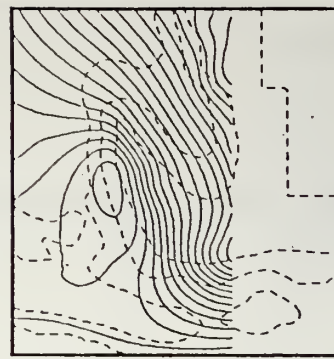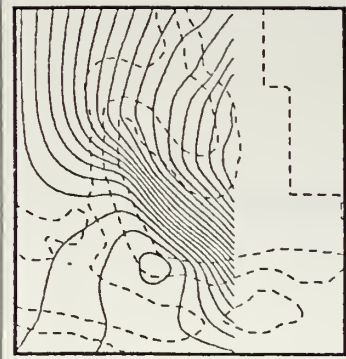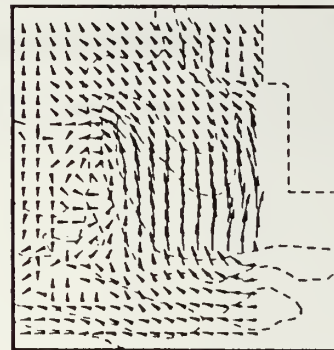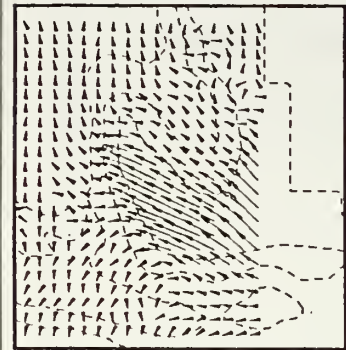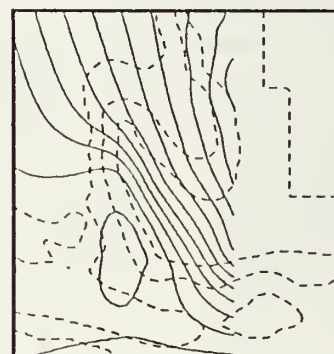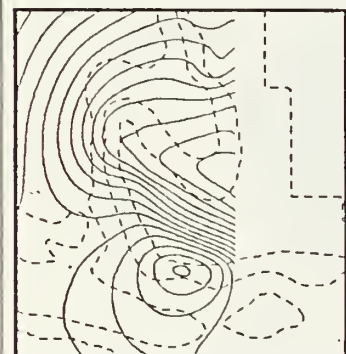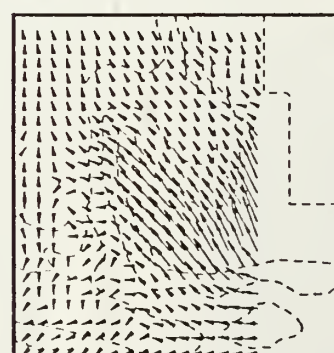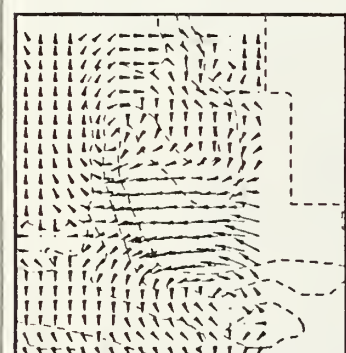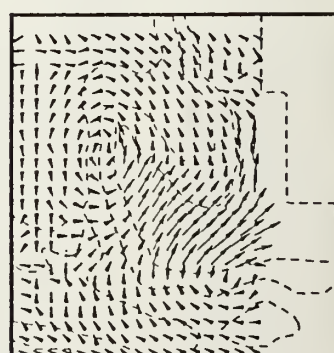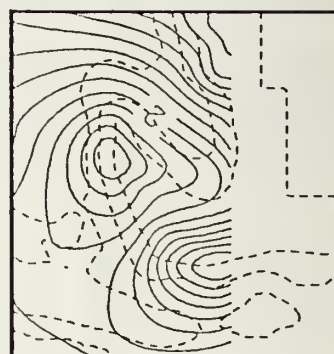
Figure E2. Forcing at the K_1 period.

116

Figure E3. Forcing at the O_1 period.

117
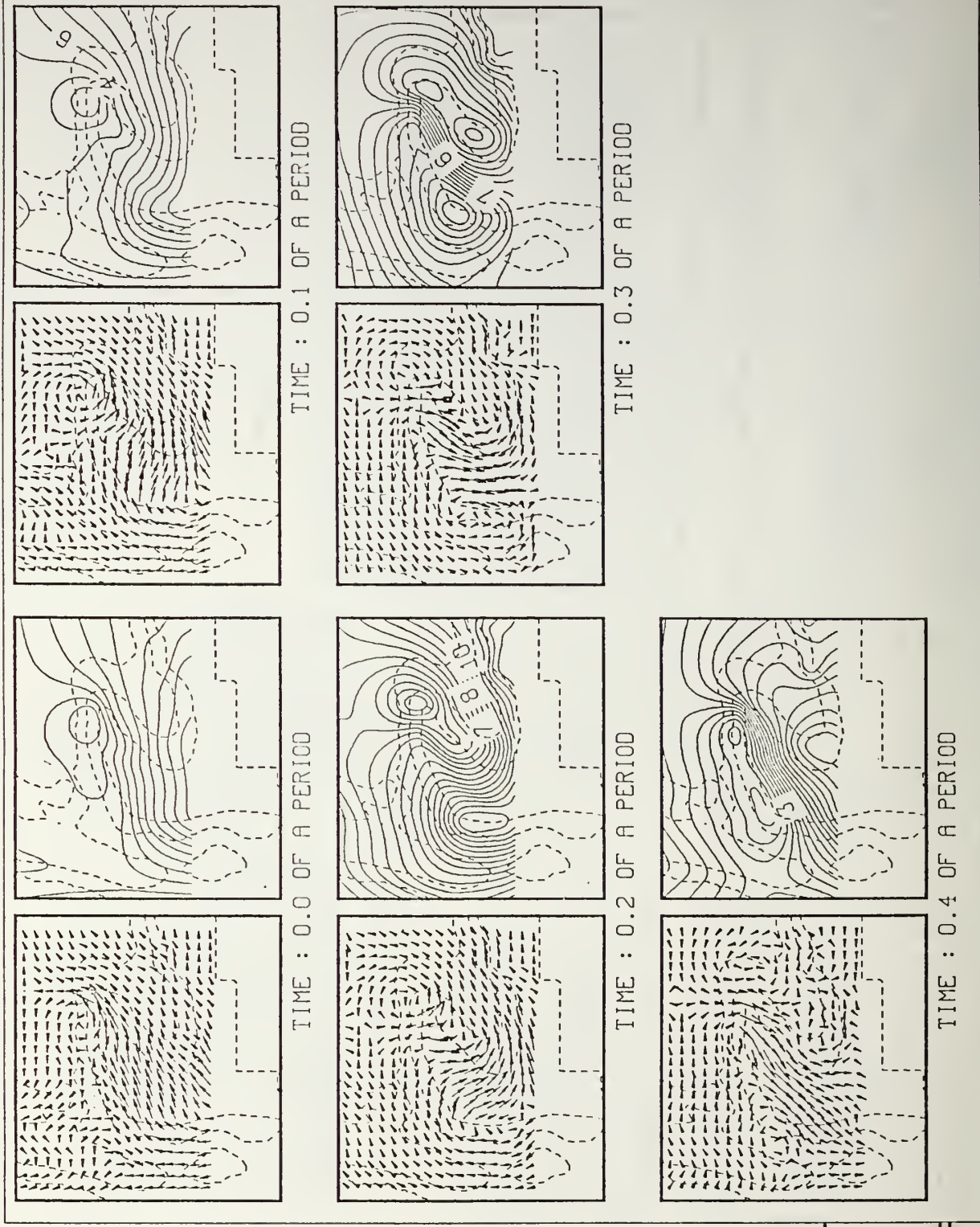
Figure E4. Forcing period of 34.9 hours.
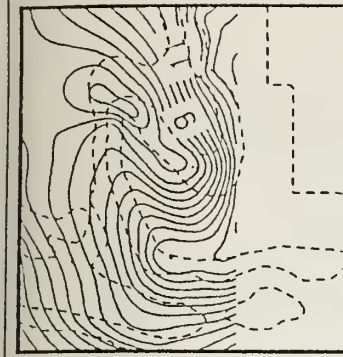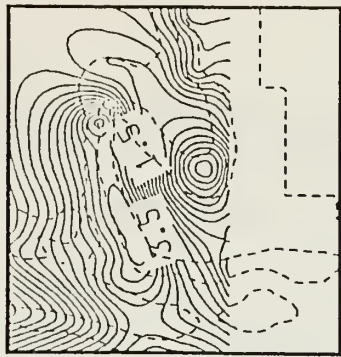
118
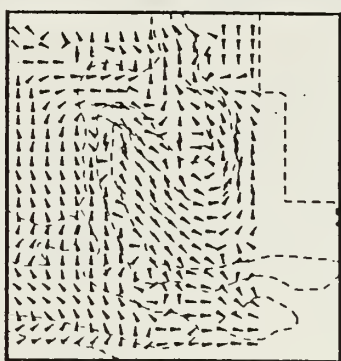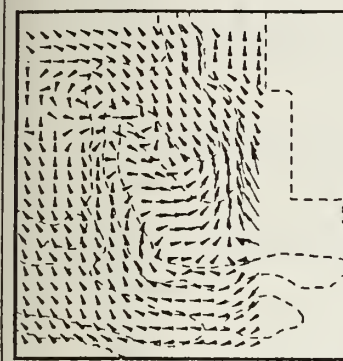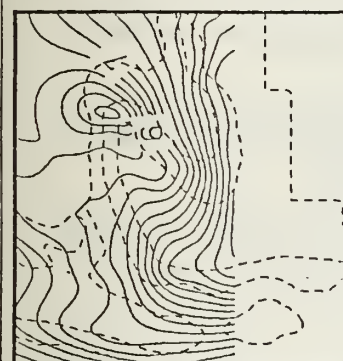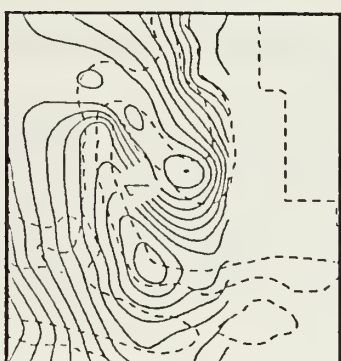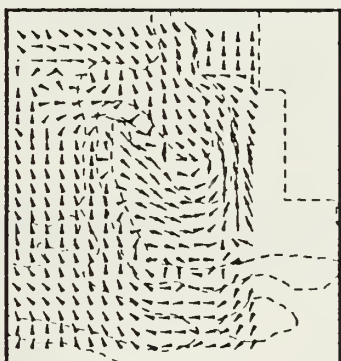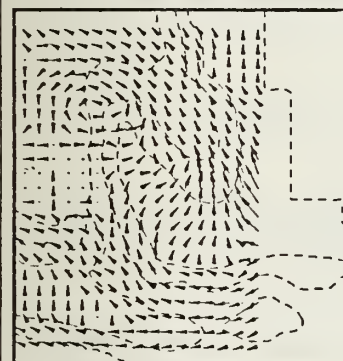
Figure E5. Forcing period of 49 hours.

119

LIST OF REFERENCES

Brink, K.H., Propagation of barotropic continental shelf waves over irregular bottom topography, *J. Phys. Oceanogr., 10*, 765-778, 1980.

Brink, K.H., Scattering of long coastal trapped waves due to bottom irregularities, *Dyn. Atmos. Oceans, 10*, 149-164, 1986.

Brink, K.H., Coastal ocean physical processes, *Review of Geophysics and Space Physics, 25*, 204-216, 1987.

Brink, K.H., The effect of stratification on seamount trapped waves, *Deep-Sea Res., 36*, 825-844, 1989.

Cartwright, D.E., Extraordinary tidal currents near St. Kilda, *Nature, 223*, 928-932, 1969.

Cartwright, D.E., J.M. Huthnance, R. Spencer and J.M. Vassie, On the St. Kilda shelf tidal regime, *Deep-Sea Res., 27A*, 61-79, 1980.

Chao, S.-Y., L.J. Pietrafesa and G.S. Janowitz, The scattering of continental shelf waves by an isolated topographic irregularity, *J. Phys. Oceanogr., 9*, 687-695, 1979.

Chapman, D.C., On the influence of stratification and continental shelf and slope topography on the dispersion of subinertial coastally trapped waves, *J. Phys. Oceanogr., 13*, 1641-1652, 1983.

Chapman, D.C., and K.H. Brink, Shelf and slope circulation induced by fluctuating offshore forcing, *J. Geophys. Res., 92*, 11741-11759, 1987.

Chapman, D.C., Enhanced subinertial diurnal tides over isolated topographic features, *Deep-Sea Res., 36*, 815-824, 1989.

Clarke, A.J., and K.H. Brink, The response of stratified, frictional flow of shelf and slope waters to fluctuating large-scale, low-frequency wind forcing, *J. Phys. Oceanogr., 15*, 439-453, 1985.

Cousins J.D., CEAREX ambient noise data measured northeast of Svalbard. *Masters Thesis, Naval Postgraduate School*, 1991.

Crawford, W.R., and R.E. Thomson, Continental Shelf Waves of diurnal period along Vancouver Island, *J. Phys. Oceanogr., 87(C12)*, 9516-9522, 1982.

Crawford, W.R., and R.E. Thomson, Diurnal-period Continental Shelf Waves along Vancouver Island, a comparison of observations with theoretical models, *J. Phys. Oceanogr.*, *14(10)*, 1629-1646, 1984.

Daifuku, P.R., and R.C. Bearsdley, The K_1 tide on the continental shelf from Novia Scotia to Cape Hatteras, *J. Phys. Oceanogr.*, *13*, 3-17, 1983.

Gill, A.E., and E.H. Schumann, The generation of Long Shelf Waves by the Wind, *J. Phys. Oceanogr.*, *4*, 83-90, 1974.

Gjevik, B., and T. Straume, Model simulations of the M_2 and the K_1 tide in the Nordic Seas and the Arctic Ocean, *Tellus*, *41A*, 73-96, 1989.

Grimshaw, R., The effects of a variable Coriolis parameter, coastline curvature and variable bottom topography on Continental Shelf Waves, *J. Phys. Oceanogr.*, *7*, 547-554, 1977.

Haltiner, G.J., and R.T. Williams, Numerical prediction and dynamic meteorology, 2 nd edition, John Wiley & Sons, 1980, 477 pp.

Heath, R.A., Tidal currents in the southwestern Pacific Basin and Campbell Plateau, southeast of New Zealand. *Deep-Sea Res.*, *30*, 393-409, 1983.

Hoffman, P.J., Transpolar sea ice drift in the vicinity of the Yermak Plateau as observed by ARCTEM1Z 86 buoys. *Masters Thesis, Naval Postgraduate School*, 89 p.

Hopkins, T.S., and D.A. Dieterle, An externally forced barotropic circulation model for the New York Bight, *Cont. Shelf Res.*, *2*, 49-73, 1983.

Hsueh, Y., On the theory of deep flow in the Hudson Shelf Valley, *J. Geophys. Res.*, *85*, 4913-4918, 1980.

Hunkins, K., Anomalous diurnal tidal currents on the Yermak Plateau, *J. Mar. Res.*, *44*, 51-69, 1986.

Huthnance, J.M., On the diurnal tidal currents over Rockall Bank, *Deep-Sea Res.*, *21*, 23-35, 1974.

Huthnance, J.M., On Coastal Trapped Waves: analysis and numerical calculation by inverse iteration. *J. Phys. Oceanogr.*, *8*, 74-92, 1978.

Kowalik, Z., A note on the co-oscillating M_2 tide in the Arctic Ocean, *Dt. Hydrog. Z.*, *32*, 100-112, 1979.

Lewis, J.K., R.E. Englebretson and W.W. Denner, Examples of ice pack rigidity and mobility characteristics determined from ice motion, *Geojournal*,*18.1*, 69-77, 1989.

Longuet-Higgins, M.S., Steady currents induced by oscillations round islands, *J.Fluid Mech.*, *42*,701-720, 1970.

Mauchly, J.W., A significance test for ellipticity in the harmonic dial, *Terrestrial magnetism and atmospheric electricity*, *46*, 145-148, 1940.

McPhee, M.G., Analysis and prediction of short-term ice drift, *Proc. of 5ᵗʰ Int. Conf. on offshore mechanics and Artic Engr.*, Am. Soc. of Mech. Engr., Apr. 1986.

McPhee, M.G., A time dependent model for turbulent transfer in a stratified oceanic boundary layer, *J. Geophys. Res.*, *92*, 6977-6986, 1987.

Middleton, J.H., T.D. Foster and A. Foldvik, Low frequency currents and continental shelf waves in the southern Weddel Sea, *J. Phys. Oceanogr.*, *12(7)*, 618-634, 1982.

Middleton, J.H., T.D. Foster and A. Foldvik, Diurnal shelf waves in the southern Weddel Sea, *J. Phys. Oceanogr.*, *17(6)*, 784-791, 1987.

Morison , J.H., M.G. McPhee and G.A. Maykut, Boundary layer, upper ocean and ice observations in the Greenland Sea marginal ice zone, *J. Geophys. Res.*, *92*, 6987-7011, 1987.

Muench ,R.D., L. Padman, A.J. Plueddemann, and R. Pinkel, Diurnal Currents over the Yermak Plateau, Presented at AGU Fall meeting, San Francisco, Ca., Nov. 1990.

Munk, W., F. Snodgrass and M. Wimbush, Tides off-shore: transition from California coastal to deep-sea waters, *Geophys. Fluid Dyn.*, *1*, 161-235, 1970.

Padman, L., and T.M. Dillon, Turbulent mixing near the Yermak Plateau during CEAREX, *J. Geophys. Res.*, in press, 1991.

Saint-Guily, B., Sur la propagation des ondes de seconde classe le long d'un talus continental, *C.R. Acad. Sci. Paris, t.282, Serie B.*, 141-144, 1976.

Schwiderski, E.W., Tides in *The Nordic Seas,* edited by B. Hurdle, pp. 219, Springer-Verlag, New-York, 1986.

Schwing, F.B., Subinertial circulation on the Scotian shelf, observations and models, Ph.D. dissertation, Dalhousie University, 1989, 207 pp.

Smith, G.D., Numerical solution of partial differential equations: finite difference methods, 3 rd edition, Oxford University press, 1985, 337 pp.

U.S.G.S., Map Projections - A working manual, U.S. Geological survey professional paper 1395, 1987.

Wang, D.P., Diffraction of continental shelf waves by irregular alongshore geometry, *J. Phys. Oceanogr.*, *10*, 1187-1199, 1980.

Webster, I., Scattering of coastally trapped waves by changes in continental shelf width, *J. Phys. Oceanogr.*, *17*, 928-937, 1987.

Wilkin, J.L., and D.C. Chapman, Scattering of continental shelf waves at a discontinuity in shelf width, *J. Phys. Oceanogr.*, *17*, 713-724, 1987.

Wilkin, J.L., and D.C. Chapman, Scattering of coastal-trapped waves by irregularities in coastline and topography, *J. Phys. Oceanogr.*, *20*, 396-421, 1990.

INITIAL DISTRIBUTION LIST

9.   Department of Meteorology   1
      Attn: Chairman
      Naval Postgraduate School
      Monterey, CA 93943-5000

10.   Department of Electrical and Computer Engineering   1
      Attn: Dr. J. Miller
      Naval Postgraduate School
      Monterey, CA 93943-5000